LUND UNIVERSITY

Low-Complexity Multiband and Beam-Reconfigurable Antennas for Beyond 5G Communications

Liang, Qiuyan

2023

Link to publication

Citation for published version (APA):
Liang, Q. (2023). *Low-Complexity Multiband and Beam-Reconfigurable Antennas for Beyond 5G Communications*. Electrical and Information Technology, Lund University.

Total number of authors:
1

General rights
Unless other specific re-use rights are stated the following general rights apply:
Copyright and moral rights for the publications made accessible in the public portal are retained by the authors and/or other copyright owners and it is a condition of accessing publications that users recognise and abide by the legal requirements associated with these rights.
• Users may download and print one copy of any publication from the public portal for the purpose of private study or research.
• You may not further distribute the material or use it for any profit-making activity or commercial gain
• You may freely distribute the URL identifying the publication in the public portal

Read more about Creative commons licenses: https://creativecommons.org/licenses/

Take down policy
If you believe that this document breaches copyright please contact us providing details, and we will remove access to the work immediately and investigate your claim.

LUND UNIVERSITY

PO Box 117
221 00 Lund
+46 46-222 00 00

Low-Complexity Multiband and Beam-Reconfigurable Antennas for Beyond 5G Communications

Qiuyan Liang

Lund 2023

© Qiuyan Liang, 2023
"Low-Complexity Multiband and Beam-Reconfigurable Antennas for Beyond 5G Communications"
Published articles have been reprinted with permission
from the respective copyright holder.

Series of licentiate and doctoral theses
No. 153
ISSN 1654-790X153
ISBN 978-91-8039-564-9 (print)
ISBN 978-91-8039-565-6 (pdf)

This thesis is produced by using the Microsoft Word
Printed in Sweden by *Tryckeriet i E-huset*, Lund.

Department of Electrical and Information Technology
Lund University, Box 118, SE-221 00 Lund, Sweden

To my dear family

Popular Science

Wireless communication networks have been widely developed and utilized for the past several decades. Nowadays the use of wireless internet has permeated many aspects of our lives, including study, work, travel, and entertainment. Correspondingly, the content of wireless communication has been enriched from voice in the early days to text, pictures, videos, and live streaming today, providing many conveniences to our lives. These ever-more-complex contents transmitted in wireless communication networks are essentially in the form of data, and ever-increasing data rates are needed to support the content delivery.

The communication of information requires a transmitter and a receiver. For example, if someone transmits information by speech or body language, then the information can be received by another person's ears or eyes. Similarly, wireless communication also requires a transmitter and a receiver, with an antenna being a critical component in each. At the transmitter, the antenna converts guided signals that contain the information to unguided signals in the form of electromagnetic waves, which propagate towards the antenna at the receiver to be converted back to guided signals. The received signals are then processed to recover the transmitted information. Following the demand for high data rates, the antennas in wireless communications are required to provide more features and higher performance.

Utilizing larger absolute frequency bandwidth for the wireless communication is one common approach to provide higher data rate. Therefore, due to the availability of more unoccupied frequency spectra at higher frequencies, wireless communication is expanding towards the higher frequencies, from sub-6 gigahertz (GHz) bands to millimeter-wave (mm-wave) bands in 5G, and in the future, to terahertz (THz) bands. However, the smaller signal wavelengths at higher frequencies incur higher propagation losses. In fact, this effect is already noticeable within the sub-6GHz bands, where sub-1GHz bands are typically favoured for providing larger coverage areas. Moreover, the electromagnetic waves in mm-wave bands and above experience more noticeable loss due to the atmospheric absorption and obstacles in the environment than in sub-6GHz bands. Therefore, to establish more reliable communication, the signal energy needs to be focused in the desired direction, which requires the antenna to generate a beampattern with higher gain in

this direction. However, the higher gain is achieved at the cost of a smaller beamwidth (i.e., angular range in which the gain is increased). Since the relative direction between transmitter and receiver is often not fixed, the smaller beamwidth implies the need for beam steering, i.e., the beampatterns of the high gain transmitter and receiver antennas need to be steered towards each other.

Due to higher losses in higher frequency bands, smaller cells and hence many more base stations are needed to maintain the same coverage area of the wireless network. Traditionally, beam-steerable high gain antennas are provided by phased array antennas. However, an array antenna requires many antenna elements connected by a feeding network, which is complicated and hence expensive to design and implement. The feeding network is also bulky, and it tends to increase the loss of energy. Therefore, beam-steerable antennas with low-complexity structures and high space utilization are highly desirable to improve system architecture and save installation resources. In this context, antennas based on partially reflective surface (PRS) can provide high gain with simple structure and low cost, which have good potential for application in future base stations. However, PRS antenna needs to be further developed to realize its full potential, despite being proposed more than half a century ago. This is because, until recently, it had not attracted much research interest. The first topic of this thesis is on enhancing two aspects of PRS antenna design, namely beam steering capability and shared-aperture antenna design.

Existing PRS antennas mainly use standard reconfigurable approaches for beam steering, e.g., using reconfigurable loads on the PRSs' unit cells. The beam can be pointed towards different directions in different reconfigurable states. However, current beam-reconfigurable PRS antennas suffer from narrow coverage range, distorted beam shape and considerable gain variations over the beams in different directions, which may lead to degradation of communication quality. On the other hand, shared-aperture antenna design with PRS aims to integrate antennas working at different frequency bands into a shared space to provide high space utilization. However, existing design schemes suffer from inflexible frequency ratio (of the bands) and bulky antenna structures. Therefore, the main part of this thesis deals with the research question on how to solve the challenges encountered by PRS antennas with respect to beam reconfigurability and shared aperture designs, while maintaining low-complexity structures.

Besides base stations with fix installations, wireless communication networks consist of a large number of user devices, including mobile terminals. With the rollout of 5G, terminal antennas are being developed to cover both existing and new 5G frequency bands, spanning both sub-6GHz bands and mm-wave bands. To save antenna implementation space, it is desirable to co-design and even co-locate these antennas. However, existing co-design approaches suffer from complex structure of the mm-wave antenna and low space utilization. Therefore, the other part of this thesis is about solving the research question on how to co-design the sub-6GHz and mm-wave antennas for mobile terminals for compactness and low-complexity.

Abstract

Antennas with large frequency bandwidth, high gain, and beam steering capability are very importance for future wireless communication systems. However, it is very challenging to design antennas with low-complexity structures and high space utilization that can achieve these desired features. Base stations with fixed installations and non-stationary mobile terminals play critical roles in wireless communication networks. The research in this thesis focuses on the low-complexity multiband and beam-reconfigurable antenna design for the two applications.

The first topic of this thesis is about partially reflective surfaces (PRS) antennas, which have significant potential for application in future base stations. In the first part (Part I) of this thesis, existing PRS antennas and challenges to be addressed in PRS antenna design are introduced with respect to beam steering capability and shared-aperture antenna design. To give a clearer insight into the working principle of PRS antenna as well as several observed phenomena involving PRS, the existing theory for PRS antenna is extended. Ray-tracing models as well as the theory of PRS unit cells are utilized to explain the operation of PRS antennas that generate broadside and/or deflected beams. Using these tools, two practical PRS antennas are designed for beam reconfigurability and shared-aperture implementation, respectively. In the first work, we compare the beam deflection capability of different types of PRSs using ray-tracing analysis, with the aim of providing a guideline for selecting a suitable PRS type that would yield a larger beam steering range. In addition, the role of a feeding source in enhancing beam deflection of PRS is explained using ray-tracing analysis, and a beam-reconfigurable feeding source with low-complexity structure is presented. In the second work, we derive the frequency ratio gap for traditional dual-band shared-aperture Fabry-Pérot cavity (DS-FPC) antennas with single-layer PRS and subsequently present a shared-aperture antenna design method with flexible frequency ratio to fill the gap.

The second topic of this thesis is on the co-design of mobile terminal antennas that can cover a wide range of frequency bands. Such antennas are of significant current interest due to the current trend of utilizing higher frequency spectra in wireless communication. A co-designed millimeter-wave (mm-wave) and sub-6GHz antenna system is conceived, where the mm-wave antennas that offer reconfigurable

beams for beam steering are integrated into the capacitive coupling elements (CCEs) of the sub-6GHz antenna. Such an implementation aims to achieve a compact and low-complexity antenna structure. In addition, several techniques have been investigated by simulation to achieve further performance improvements in the proposed antenna system with respect to mm-wave antenna gain and bandwidth as well as sub-6GHz antenna tunability and bandwidth.

Preface

This doctoral thesis consists of two parts. The first part (Part I) gives an overview of the research during the three and half years as a doctoral student at the department of Electrical and Information Technology (EIT), Lund University, Sweden. The second part (Part II) is composed of four papers that constitute my main scientific work, including:

Paper I

Qiuyan Liang and Buon Kiong Lau, "Comparison of capacitive and inductive partially reflective surface antenna using ray-tracing," in *Proc. 16th Europ. Conf. Antennas Propag. (EuCAP'2022)*, Madrid, Spain, Mar. 27- Apr. 1, 2022.

Paper II

Qiuyan Liang, Buon Kiong Lau, and Gaonan Zhou, "Beam-reconfigurable antenna with inductive partially reflective surface and parasitic elements," *IEEE Trans. Antenna Propag.*, 2023, Manuscript finished.

Paper III

Qiuyan Liang, Buon Kiong Lau, and Gaonan Zhou, "Dual-band shared-aperture antenna with single-layer partially reflecting surface," *IEEE Trans. Antenna Propag.*, 2023, Submitted.

Paper IV

Qiuyan Liang, Hanieh Aliakbari, and Buon Kiong Lau, "Co-designed millimeter-wave and sub-6GHz antenna for 5G smartphones," *IEEE Antennas Wireless Propag. Lett.*, vol. 21, no. 10, pp. 1995-1999, Oct. 2022.

During my doctoral studies, I had also contributed to the following publications, which are not included in this thesis:

Conference papers

- Qiuyan Liang and Buon Kiong Lau, "Beam manipulation using characteristic mode analysis for switchable beam patch antenna," in *Proc. 2020 IEEE Int. Symp. Antennas Propag.*, Montreal, Canada, Jul. 5-10, 2020.
- Qiuyan Liang and Buon Kiong Lau, "Beam reconfigurable reflective metasurface for indoor wireless communications," in *Proc. 2021 IEEE Int. Symp. Antennas Propag.*, Singapore, Singapore, Dec. 4-10, 2021.
- Qiuyan Liang and Buon Kiong Lau, "Analysis of partially reflective surface antenna with different reflection magnitudes using ray-tracing," in *Proc. 2022 IEEE Int. Symp. Antennas Propag.*, Denver, CO, Jul. 10-15, 2022.

Journal papers

- Qiuyan Liang, Baohua Sun, and Gaonan Zhou, "Miniaturization of Rotman lens using array port extension," *IEEE Antennas Wireless Propag. Lett.*, Early Access, 2022.
- Qiuyan Liang, Baohua Sun, and Gaonan Zhou, "A dual-band shared-aperture parasitic array radiator antenna for WLAN applications," *Int. J. RF Microw. Comp.-Aided Eng.*, vol. 31, no. 11, 2021.
- Gaonan Zhou, Baohua Sun, Qiuyan Liang, Yuhang Yang, and Jianghong Lan, "Beam-deflection short backfire antenna using phase-modulated metasurface," *IEEE Trans. Antenna Propag.*, vol. 68, no. 1, pp. 546-551, Jan. 2020.

Acknowledgements

The three and a half years of my PhD study at Lund University have been the most enriching time of my life. I have gained so much, and I am so grateful that I have met so many wonderful people during this experience.

First and foremost, I would like to express my sincere gratitude to my supervisor Prof. Buon Kiong Lau. Thank you for offering me the opportunity to start this journey at Lund University, for your time and enthusiasm in the discussions, and for your generosity in providing me with plenty of valuable guidance in my research. Your rigorous work attitude is a valuable quality that I am and will continue to pursue in my career. Your positive attitude and enthusiasm inspire people around you.

I would like to thank Prof. Mats Gustafsson, my co-supervisor and Prof. Daniel Sjöberg. Thank you for organising a variety of electromagnetics-related seminars that have provided me with access to further knowledge and expertise in my field of study. Thank you for your valuable advice on my individual study plan during my PhD study.

I would like to thank my colleague Hanieh Aliakbari for collaborating with me in some of my research work. I am fortunate to have you as a friend and thank you for all your support in my research, courses, teaching, and daily life.

I also want to thank all my former and current colleagues at EIT for the great working environment we have created together. More specifically, I thank all the administrative staff for providing strong and essential support to my PhD study, and all my colleagues in Communications Engineering Division for your company in the division meetings, activities and “fika”.

I would also like to thank these colleagues for their help in the writing of my thesis: Xuhong Li, Leif Wilhelmsson and Siyu Tan.

During the past three and a half years, I have made many friends and have been fortunate to spend time with them: Hanieh Aliakbari, Liying Nie, Shang Xiang, Sevda Özdemir, Kranti Kumar Katare, Irfan Yousaf, Kentaro Murata, Ahmed El Yousfi, Ben Nel, Xuhong Li, Tao Qin, Yuyan Cao, Guoda Tian, Siyu Tan, Xuesong

Cai, Yanan Wu, Haipeng Li, Jie Ding, Siyuan Cang, Xiaotong Tu, Jing Yang, Hui Zhu, and Xiaoya Li. Your company has brought me lots of much needed warmth.

I would like to express my deepest gratefulness to my family: my parents, my sisters and brothers, and my lovely nephews and niece, for your support and remote companionship, and for filling the whole family with love and hope.

Most importantly, I would like to thank my husband Gaonan Zhou. You are always warm, patient, and optimistic. Your firm companionship has been the biggest support for me to get to where I am today. It is my greatest fortune to have you in my life.

Finally, I thank all the strangers in the big world around me; everyone's own world makes up the whole world we live in. May the world be full of peace and love.

Qiuyan Liang

Lund, Feb. 2023

List of Acronyms and Abbreviations

1-D	One-Dimensional
5G	Fifth-Generation
5G NR	5G New Radio
6G	Sixth-Generation
AiP	Antenna-in-Package
AMC	Artificial Magnetic Conductor
CCE	Capacitive Coupling Elements
DC	Direct Current
DS-FPC	Dual-Band Fabry-Pérot Cavity
FEM	Finite Element Method
FPC	Fabry-Pérot Cavity
GNSS	Global Navigation Satellite System
HB	High Band
ISM	Industrial Scientific Medical
LB	Low Band
LTE	Long-Term Evolution
MIMO	Multiple-Input Multiple-Output
NFC	Near-Field Communication
PBC	Periodic Boundary Condition

PCB	Printed Circuit Board
PEC	Perfect Electric Conductor
PIFA	Printed Inverted-F Antennas
PRS	Partially Reflective Surface
Mm-Wave	Millimeter-Wave
SBA	Short Backfire Antenna
SLL	Sidelobe Level
UWB	Ultrawide Band
Wi-Fi	Wireless Fidelity
WLAN	Wireless Local Area Network

Contents

Part I

Introduction

1 Motivation and Outline

Nowadays wireless communication is ubiquitous and has become an indispensable part of our daily lives. We have become accustomed to viewing the latest news, watching videos, participating in online meetings, etc. on our wireless devices. With the widespread adoption of user devices and rich multimedia content, the demand for higher data rates is also increasing rapidly. As a critical component in wireless communication systems, antennas play the roles of transmitting and receiving signals. To facilitate higher data rates, the antenna systems are required to provide more features and higher performance.

In this chapter, we first provide an overview of the development trends of antennas in wireless communication and several prevailing antenna design approaches to support these trends. Then, we introduce the current developments and challenges in antenna design for applications in base stations and mobile terminals, on which the motivation for the research in this thesis is formed. The research questions and thesis goals are then presented, alongside with the thesis structure.

1.1 Overview of Antenna Development Trends

With the rapid growth in both the number of user devices and the data rates, more advanced wireless communication networks are needed. The deployment of fifth-generation (5G) networks and the increasing volume of research in future sixth-generation (6G) networks are aimed at providing enhanced wireless communication capabilities and novel features, which require higher data rate and higher precision in terms of latency, synchronicity, reliability, and localization [1], [2].

As shown in Fig. 1.1, smaller cells and hence many more base stations are indispensable components in the architecture of future wireless communication networks that provide continuous connectivity, particularly at higher frequency bands [3]. Consequently, a substantial number of antennas will be needed for base

Figure 1.1: Many more base stations in future wireless communication networks.

stations in the deployment of future wireless communication networks [4]. Therefore, the antennas need to be designed using more advanced techniques to improve system architecture and save resources. In the following, four representative antenna development trends for future communication systems and the corresponding antenna design techniques to meet these trends are summarized:

1. **Wide/multi-band operation**: The 5G New Radio (5G NR) air interface has been developed to meet the requirements of 5G networks. The air interface covers the wide range of frequency bands from sub-1GHz bands to millimeter-wave (mm-wave) bands [5]. Accordingly, the antennas need to be designed for wideband operation, to minimize the number of antennas needed for frequency coverage.

   Ultrawide band (UWB) antennas can be designed to operate over a wide range of frequency bands. Some UWB antennas, including Vivaldi antenna and bi-cone-shaped antenna, have been designed for an ultrawide range of the 5G frequency bands [6]. However, since the size of UWB antennas tends to be limited by the wavelength at the lowest frequency of operation, they tend to be physically large and unsuitable for applications with limited implementation space. In addition, a continuous wide operating band is not needed or even allowed in many applications. For example, 5G NR should not operate in the unlicensed industrial scientific medical (ISM) bands (e.g., 0.9, 2.4, and 5.8GHz). Therefore, antennas working in multiple non-contiguous frequency bands have also been proposed for

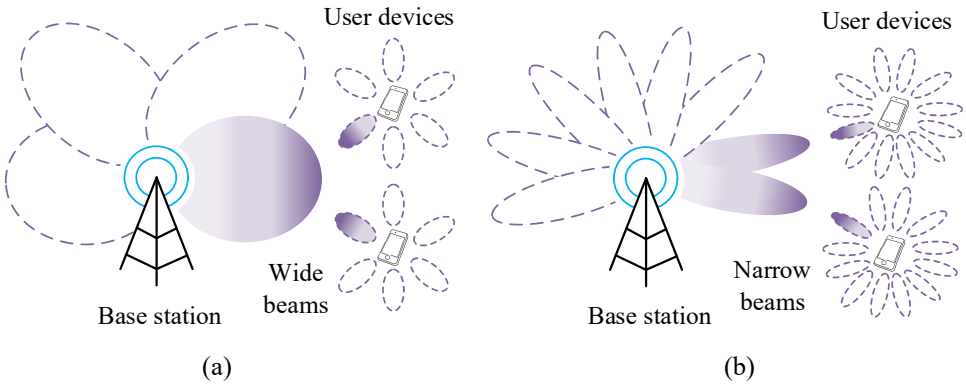

Figure 1.2: Beam distributions of base stations and user devices in (a) low and (b) high frequency bands.

a variety of applications, such as wireless local area network (WLAN) [7], base stations [8], and mobile phones [9].

2. **Beam steering capabilities:** Compared with the lower frequency bands (e.g., sub-1GHz), the electromagnetic waves in the higher frequency bands experience more noticeable attenuation due to higher propagation losses; and in the case of millimeter waves, high atmospheric and material absorptions in the environment as well [10]. To compensate for the high propagation losses, the antennas operating in higher frequency bands need to generate beams with higher gains[1]. However, a higher gain is achieved at the cost of a narrower half-power beamwidth[2] and thus the angular coverage range is reduced. Therefore, base station and user device antennas in high frequency applications need to be capable of beam steering to maintain the same coverage area as in low frequency bands, as depicted in Fig. 1.2.

   The high gain performance of an antenna is attributed to a large effective antenna aperture and the beam steering capability typically relies on changing the phase distributions of the signal across the antenna aperture [11]. A wide variety of antennas have been developed for beam steering, including phased array antennas and antennas based on passive beamforming feeding networks, reflectors, and

[1] According to [77], *gain* (in a given direction) describes the ratio of the radiation intensity in a given direction to the radiation intensity that would be produced if the power accepted by the antenna were isotropically radiated.

[2] According to [77], *half-power beamwidth* describes the angle between the two directions in which the radiation intensity is one-half the maximum value in a radiation-pattern cut containing the direction of the maximum of a lobe.

lenses [12]. These beam steering antennas are introduced in the following, and their characteristics in terms of beamforming flexibility, occupied space, structure complexity, and economic cost are summarized.

Phased array, invented more than a century ago [13] is arguably the most common type of beam steering antenna. By connecting the antenna elements with phase shifters and other RF elements, the amplitude and phase distributions of the phased array can be controlled flexibly for more diverse beampatterns, which is a key technique to provide coverage in satellite communications [14]. However, the large numbers of required phase shifters and RF components render the antenna system highly complex, bulky, and expensive.

Passive beamforming feeding networks can also be used for antenna arrays to achieve multiple fixed beams pre-steered to cover different angular ranges. They can be classified into two categories according to their working principles: lens-based [15] or circuit-based feeding networks [16]. Both feeding networks can achieve multiple phase distributions along their output ports for antenna arrays to generate beams in different directions without the use of active RF components. However, the lens-based and circuit-based networks suffer from the problems of large size and complex circuit architecture, respectively. For antenna arrays with a large number of antenna elements, these problems are even more pronounced, making integration into compact antenna systems difficult.

The reflector-based and lens-based antennas operate with quasi-optical principles, where the beam steering is achieved by changing the position of the external feeding sources relative to the reflectors or lenses [17], [18]. These two types of antennas have rotationally symmetrical structures, which facilitate flexible beam steering in both azimuth and elevation. However, due to the use of external feeding sources and non-planar reflectors or lenses, these two types of antennas tend to occupy a large implementation space, which may increase the installation cost of the antenna systems. Recently, transmitarray/reflectarray antennas that are based on planar metasurfaces have been proposed to replace the traditional bulky reflector or lens [19], [20], thus simplifying the antenna structures.

3. **Low complexity:** Considering the increasing use of higher frequencies and the need for more base stations for seamless connectivity, it can be anticipated that an unprecedentedly large number of base station antennas will be deployed. To keep the fabrication and installation costs down, antenna designs with minimal structural complexity are desired. The requirement for low-complexity antenna design can be addressed from several perspectives: the antenna structure, beam steering techniques, fabrication process, and antenna installation.

   The antenna structure can be simplified by minimizing the usage of feeding networks. As mentioned earlier, the high gain performance and beam steering capability of phased array antennas rely on sophisticated feeding networks to provide the required amplitude and phase distributions, which brings high

structural complexity and high insertion losses. Several types of antennas based on metasurfaces or parasitic elements can generate high gain beams without using feeding networks, such as transmitarray and reflectarray antennas as mentioned above, partially reflective surface (PRS) antenna [21], planar Yagi-Uda antenna [22], and short backfire antenna [23]. By manipulating the propagation of waves from the excited feeding source to some resonant structures (e.g., metasurfaces) with specific transmission/reflection properties or some parasitic elements with specific structural parameters, the phase distribution across the antenna aperture can be rearranged. This allows the waves across the antenna aperture to achieve in-phase superposition in a certain direction, to generate high gain beam in that direction.

For antennas without feeding networks, beam steering capability can be achieved by using reconfigurable approaches without altering the antenna construction. For a metasurface-based antenna, the transmission/reflection properties of unit cells and the amplitude and phase distributions across the antenna aperture can be reconfigured by electrically controlled components, such as switches or diodes [24], [25]. For an antenna array employing parasitic elements, the reconfigurable states of the electrically controlled components also affect the equivalent electrical dimensions of parasitic elements, providing an effect similar to phase shifters [26].

The approaches of electrical reconfiguration and the usage of metasurfaces provide significant flexibility for the design of low-complexity beam steering antennas. To further simplify the antenna design, it is highly desirable for the antennas to be fabricated and installed in simple and cost-effective ways. For example, single-layer dielectric substrate is preferred to multi-layer dielectric substrate in antenna design. Moreover, planar antennas are aesthetically appealing and easy to install since the base stations are often mounted on the walls or ceilings of buildings for indoor communication scenarios. In this context, beam steering antennas based on single-layer metasurfaces have distinct advantages.

4. **High space utilization:** As more antennas will be deployed in future communication networks for higher data rates, it can be foreseen that the installation resources, such as the installation space, will be limited in practical application scenarios. Moreover, antennas for multiple generations of wireless communication systems, working in different frequency bands, need to coexist. Therefore, these antennas need to be designed with high space utilization.

   Improving antenna space utilization mostly involves two approaches. One common approach is to minimize the volume occupied by individual antennas, such as lowering the antenna profile (height). However, a trade-off between compact antenna size and acceptable antenna performance is always needed. The second, often highly regarded, approach is to integrate multiple antennas working in different frequency bands in a shared aperture. The goal of this shared-aperture

technology is to accommodate antennas of multiple frequency bands in a compact manner while maintaining their respective performance.

Metasurface plays a significant role in both approaches for high space utilization. Compared to a traditional perfect electric conductor (PEC) ground, the use of a metasurface with proper reflection phase as the ground plane can enable a lower antenna profile [27]. Moreover, because of its frequency-selective features, a metasurface can be shared by antennas in different frequency bands through providing the required transmission and reflection properties in each band [8].

In summary, according to the four antenna development trends, the antennas in future wireless communication systems need to support more frequency bands and have beam steering capabilities, especially at high frequencies, while maintaining low-complexity structure and high space utilization. These requirements present tough challenges to the design of such antennas. The utilization of metasurfaces as well as the aforesaid antenna design methods, such as beam reconfiguration approaches and shared-aperture antenna technology, provide significant potential in addressing these requirements. This thesis focuses on antennas for base stations and mobile terminals, which are critical parts of today's wireless communication networks.

1.2 PRS Antennas for Base Stations and Design Challenges

As described in the last section, metasurfaces can be used to design planar antenna structures with high gain and shared aperture. Among many types of metasurface-based antennas, those that utilize PRS have attracted a lot of attention recently due to the advantages of high gain, simple structure, and low cost. PRS antenna was first proposed for gain enhancement in the classical paper by G. Trentini [21]. Because the working principle is based on the Fabry-Pérot resonance condition [28], PRS antenna is also known as Fabry-Pérot cavity (FPC) antenna.

Since its discovery, PRS antenna has been adopted for many applications, such as CubeSat [29], WLAN [30], and mobile communications [31]. In particular, the high gain performance of the PRS antenna is suitable for base station deployment at higher frequencies, due to its low-cost and simple structure. The high gain of the PRS antenna is achieved by manipulating the propagation of waves between the feeding source (or ground plane) and the PRS. This operating principle allows the antenna to function without a feeding network.

A PRS antenna consists of a feeding source, a PRS and a fully reflecting ground plane. A conventional PRS antenna employs a uniform PRS placed at a specific distance from the ground to generate a broadside beam, as shown in Fig. 1.3(a). By

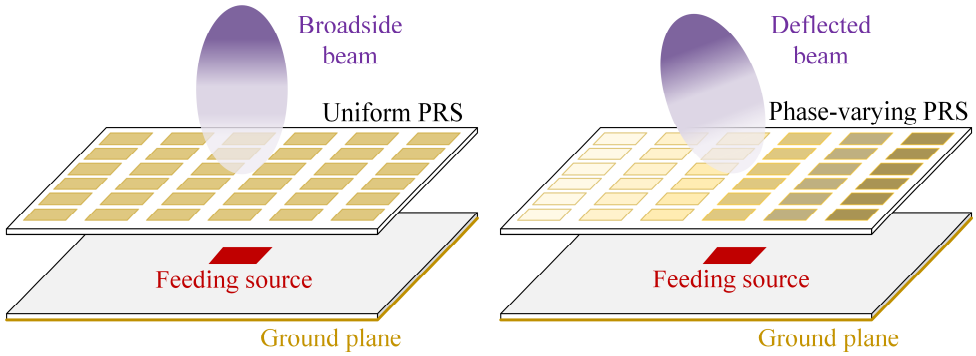

(a) (b)

Figure 1.3: PRS antennas generating (a) broadside beam and (b) deflected beam.

modifying the PRS into a nonuniform phase-varying PRS, the generated beam can be deflected from the broadside direction, as shown in Fig. 1.3(b). Recently, to enable beam steering capability and high space utilization, beam-reconfigurable PRS antennas and shared-aperture antennas with PRSs have been proposed, following the development trends of antennas for wireless communication systems as described in Section 1.1. In the first topic (main part) of this thesis, PRS antennas addressing these two aspects are studied. The aim is to enhance the antennas performance and solve the challenges encountered by the two types of PRS antennas.

1.2.1. Beam-reconfigurable PRS antennas

Typically, a PRS is composed of many unit cells with specific structures designed to provide the required transmission and reflection properties. The waves from the feeding source are reflected multiple times between the PRS and the fully reflecting ground plane, with each incident wave at the PRS also producing a transmitted wave. In this process, the multiple transmitted waves formed across the PRS can be regarded as new sources re-radiating towards the upper half space. The direction and shape of the beam generated by a PRS antenna are dependent on the amplitude and phase distributions of the multiple transmitted waves across the PRS. Therefore, the unit cell design of the PRS (e.g., with uniform vs. nonuniform transmission and reflection properties) affects the phase distribution across the PRS and hence the generated beam by the antenna, as depicted in Fig. 1.3. For a PRS antenna with beam steering capability, different phase distributions are required for beams pointing in different directions. However, since that the structural parameters of a fabricated PRS antenna are fixed, a reconfigurable approach is required for the PRS antenna to generate different phase distributions across the PRS for beam steering.

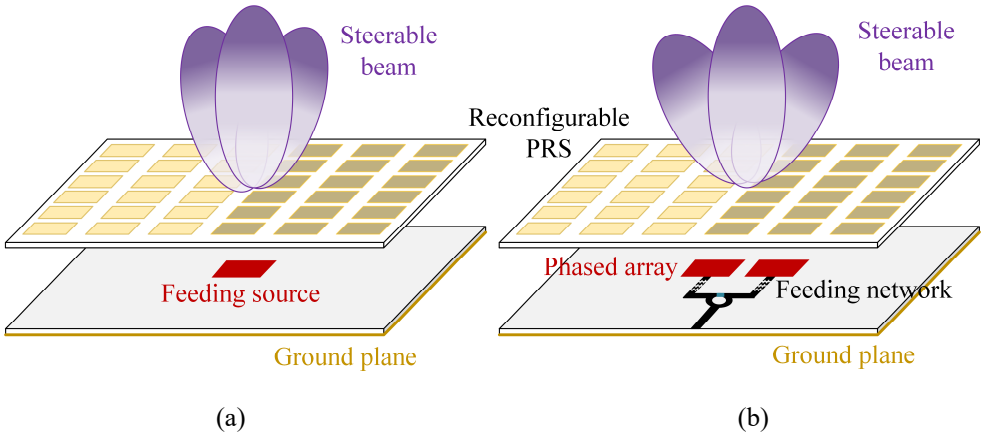

Figure 1.4: Beam-reconfigurable PRS antennas with two PRS parts for 1-D beam steering. (a) A reconfigurable PRS is employed. (b) A reconfigurable PRS and a phased array as feeding source are employed [41].

A reconfigurable PRS is mainly implemented using three approaches: mechanical rotation, movement of liquid materials, and control of electronic elements. In [32] and [33], the reconfiguration of phase distribution across a PRS is achieved by using the mechanical rotation of a pair of metasurfaces above the feeding source or by injecting the liquid metal into specific zones of the PRS. Compared to these two reconfigurable approaches, which require external motors or an additional layer with nested microfluidic channels for liquid materials, the reconfigurable approach with electronic elements is simpler in structure and can offer faster beam steering. Thus, this approach is gaining more and more interest [34]-[41].

By varying the supplied direct current (DC) biasing voltages for the electronic elements, such as varactors or PIN diodes, which are loading the PRS unit cells, the reconfigurable state of the PRS can be controlled. Compared to PIN diodes, varactors allow for independent voltage control (within a continuous range) to each PRS unit cell, which facilitates a wider range of phase distributions and finer beam steering. However, the structural complexity of the DC biasing network is significantly higher. Therefore, many existing reconfigurable PRS employ PIN diodes with low-complexity DC biasing network, consisting of two or four PRS sectors to realize one-dimensional (1-D) [37], [41] or 2-D beam steering [39], [40]. An illustration of beam-reconfigurable PRS antennas with two PRS parts for 1-D beam steering is presented in Fig. 1.4(a). By varying the reconfigurable state of the PRS, two symmetrical deflected beams and a broadside beam can be realized.

In addition to the beam deflection achieved by the reconfigurable PRS, it is found from practical design examples that a beam deflected feeding source can provide additional beam deflection to a PRS antenna [41], [42]. In [41], with a

reconfigurable feeding network consisting of phase shifters and impedance matching networks, the phased array can act as the beam deflected feeding source to provide additional beam deflection, as illustrated by the larger beam deflection angles in Fig. 1.4(b) than in Fig. 1.4(a).

By introducing reconfigurability at both the PRS and the feeding source, the beam steering capability of the PRS antenna can be enhanced. However, current beam-reconfigurable PRS antennas suffer from some common performance limitations, i.e., small beam steering range, high sidelobe levels[1] (SLLs), and considerable gain variations over different reconfigurable states. In the design of PRS antenna using a phased array as the feeding source, the reconfigurable feeding network for the phased array is still complicated and it leads to extra insertion losses. In addition, the mechanism underlying the phenomenon of the beam deflected feeding source further enhancing the beam deflection angle of the PRS antenna remains unexplained. To address the performance issues, it is essential to provide an intuitive theoretical analysis framework for beam-reconfigurable PRS antennas and utilize it to gain insight into these antennas' working principles. The resulting insight can then be exploited to achieve better antenna performance. In addition, further study is needed to lower the structural complexity of the beam-reconfigurable feeding source.

1.2.2. Shared-aperture antennas with PRS

In the design of a PRS antenna, the Fabry-Pérot resonance condition needs to be satisfied, where the reflection phase of PRS needs to be matched with the PRS height such that the multiple transmitted waves through the PRS are in-phase. For a PRS antenna with fixed structural parameters and PRS height, the Fabry-Pérot resonance condition can be satisfied at multiple specific frequencies, which enables the construction of a dual-band shared-aperture Fabry-Pérot cavity (DS-FPC) antenna using a single-layer PRS. Two high gain beams can thus be generated at the low band (LB) and the high band (HB), respectively, as depicted in Fig. 1.5(a). However, it is observed from practical design examples that the frequency ratios of DS-FPC antennas using single-layer PRS tend to be close to the ratio of the orders of the utilized FPC modes in the two frequency bands, implying that this ratio is inflexible [43]-[46].

To achieve a more flexible frequency ratio, two layers of PRS with different PRS heights can be used to form two separate Fabry-Pérot cavities working in LB and HB, respectively [47]-[53]. The PRS layers are designed to exhibit high transmission in the other frequency band to minimize wave blockage, hence

[1] According to [77], *sidelobe level (maximum relative)* describes the maximum relative directivity of the highest sidelobe with respect to the maximum directivity of the antenna.

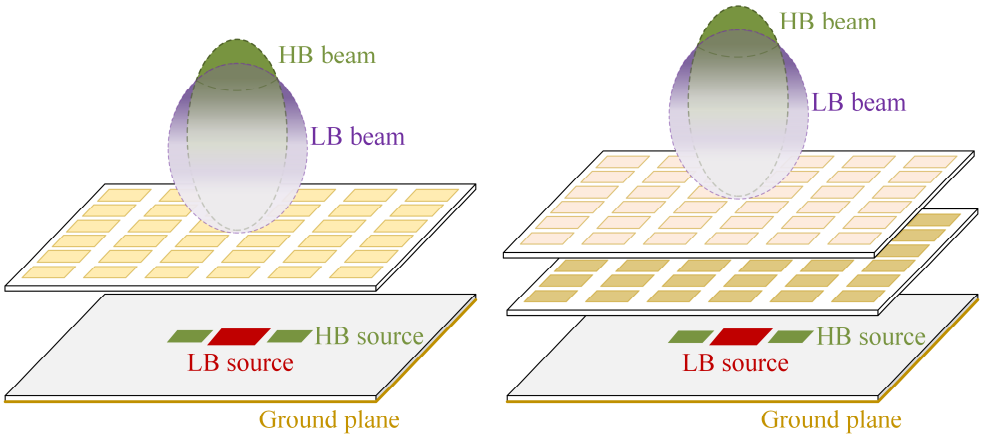

Figure 1.5: Shared-aperture PRS antennas with (a) single-layer PRS and (b) two separate layers of PRS.

generating two high gain beams in both frequency bands, as seen in the Fig. 1.5(b). However, since this design scheme requires two layers of PRS, the structural complexity of the antenna is increased and the antenna profile for HB is also increased. An artificial magnetic conductor (AMC) ground has been used in DS-FPC antennas to lower the antenna profile by compensating the propagation phase in one of the two bands [54]-[55]. The downside of this approach is that the antennas tend to exhibit narrow overlapping bandwidths between the 10dB impedance bandwidths and 3dB realized gain bandwidths.

The above DS-FPC antennas aim to construct the Fabry-Pérot cavities in both frequency bands using single- or dual-layer PRS. However, the shared-aperture antenna design can also be achieved based on different concepts in two frequency bands, where the Fabry-Pérot resonance condition is satisfied in only one frequency band. In [56], a folded transmitarray antenna working in HB and a PRS antenna working in LB are integrated in a shared aperture using four layers of substrate. However, it also suffers from an inflexible frequency ratio and the structural complexity is high. Therefore, to obtain a flexible frequency ratio while maintaining a low-complexity antenna structure, it is important to choose a suitable type of high gain antenna to integrate with a PRS antenna for high space utilization. In addition, no explanation has yet been provided for the observed limitations in the frequency ratio of DS-FPC antennas using single-layer PRS.

1.2.3. Ray-tracing analysis for PRS antenna

Ray-tracing analysis has been found to be useful for the design of PRS antennas. In the classical article that first proposed the PRS antenna [21], its working principle and design parameters are all presented using an intuitive ray-tracing model. In this early work, the emphasis is on the ray with normal incidence at the PRS, to simplify the analysis of directivity in the broadside direction. In some subsequent designs of PRS antennas, ray-tracing models accounting for oblique incidence have also been used to achieve higher gain [57] and arbitrary beam deflection angle [58].

The following are some phenomena of PRS antennas observed from practical design examples:

- Capacitive PRS exhibits higher gain than inductive PRS, given the same reflection magnitude [59], [60].
- A uniform PRS with a larger reflection magnitude than that with a smaller reflection magnitude exhibits a higher gain for an ideal, infinitely large PRS [21].
- A beam deflected feeding source can provide additional beam deflection for a PRS antenna [41], [42].

These observed phenomena show that the PRS type, the reflection magnitude of the PRS, and the beam deflection capability of the feeding source influence the antenna gain or beam direction of the PRS antenna. However, clear and intuitive explanations have not yet been provided for these phenomena. To achieve PRS antennas with more features and higher performance, proper guidelines for choosing the suitable PRS types, PRS properties, and feeding source are highly desirable. Therefore, in this thesis, ray-tracing analysis is used to explain these phenomena, and the obtained insights are utilized to address the design challenges in two research areas covered by this thesis: beam-reconfigurable PRS antenna and shared-aperture antenna design using PRS.

1.3 Co-Designed Antennas for Mobile Terminals and Design Challenges

Since the invention of the mobile phone until today, the content delivered to users has become more and more diverse: from voice to text, pictures, videos, and live streaming. The increasingly rich multimedia content delivery is supported by the increasing data rates in wireless communication networks. One approach to provide high data rates in 5G is to utilize the larger available frequency spectra in the mm-wave bands. Therefore, mobile terminals for 5G communication are starting to be developed for operation in both sub-6GHz and mm-wave bands [9].

As mentioned in Section 1.1, to compensate for the high losses in propagation of electromagnetic waves, mm-wave antennas are required to generate high gain and steerable beams. Currently, the most prevalent antenna type for mm-wave antennas is phased array antenna with feeding networks. Various antenna element types have been employed for the phased arrays, including patch antennas [61], Vivaldi antennas [62], slot antennas [63], and folded dipoles [64]. Typically, multiple mm-wave antenna arrays need to be deployed in different locations of the mobile terminal to enable beam scanning over the full angular range [62]. In a mobile terminal, the mm-wave antennas can be designed on the printed circuit board (PCB) or integrated on the protected metal frame, or added as a compact module using the antenna-in-package (AiP) method [9].

The antennas of a mobile terminal are required to cover many different bands, including the long-term evolution (LTE)/NR bands, the bands used by wireless fidelity (Wi-Fi), the bands for near-field communication (NFC) and global navigation satellite system (GNSS), and mm-wave bands [65]. Therefore, the sub-6GHz band antennas and mm-wave band antennas need to coexist in the limited space of a mobile terminal. Therefore, co-designed sub-6GHz and mm-wave antennas for mobile terminals are attracting more and more research interest.

Many co-design schemes of sub-6GHz and mm-wave antennas for mobile terminals have been proposed. In [61], [63], [66], and [67], the mm-wave band antennas are placed on the PCB in separate locations to the sub-6GHz antennas which employ chip antennas, printed inverted-F antennas (PIFA), monopoles, and patch antennas, respectively. The performance of the antennas in the two bands can then be optimized independently. In [64], [68], and [69], the mm-wave antennas are integrated with the sub-6GHz antenna by sharing their antenna structures, which enhances the space utilization of the PCB. In addition, by modifying the structure of metal bezels used to excite the sub-6GHz antennas, the mm-wave antenna can be embedded in the metal bezels [62], [70], [71].

The current co-designed antennas suffer from poor space utilization, which is caused by two main factors: the large size of sub-6GHz antenna and the considerable area occupied by the feeding networks of mm-wave phased array antennas. To design a small radiator and avoid the usage of phase shifters, reconfigurable parasitic elements are employed in [72] in a mm-wave antenna for beam steering. In this design, the beam steering is realized by shorting the parasitic elements via four transmission lines of different lengths. Even though no real switch is used in the measurement and the transmission lines occupy considerable PCB space, the utilization of parasitic elements facilitates a low-complexity implementation for the beam-steering mm-wave antenna. In summary, to further enhance the space utilization of the mobile terminals, it is crucial to choose a compact excitation technique for the sub-6GHz antennas and propose a more compact mm-wave antenna, while maintaining a low-complexity structure.

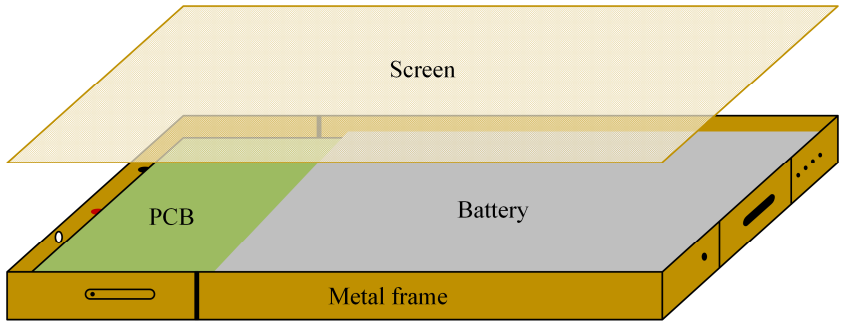

Figure 1.6: Simplified antenna design environment of a mobile terminal.

The complex environment of the mobile terminal also brings challenges to the co-designed antennas. As shown in Fig. 1.6, today's mobile terminal typically requires a metal frame, a PCB, a battery, a screen, and some other components that interact with the user [65]. Nowadays, users have higher and higher demands for the appearance of mobile phones, such as slim profile and large screen-to-body ratio, which lead to a highly integrated architecture with many metallic components. Considering that the metal components may influence the antenna performance, the antenna co-design scheme is required to be practical in the actual implementation environment. For instance, the antennas should be able to function properly in the presence of a metal screen and frame. In addition, the performance of the antennas should be rather tolerant to a slight variation in the thickness. Moreover, while selecting a co-design scheme, the locations of the antennas should be chosen to minimize blockage due to the user's hands.

1.4 Research Questions and Thesis Goals

The research work of this thesis focuses on two aspects: (1) design of low-complexity PRS antennas for base stations; (2) co-design of sub-6GHz and mm-wave antennas for mobile terminals. The research questions and goals considered for each aspect are summarized as follows.

Research questions for PRS antennas:

- Clear and intuitive explanations have not yet been provided for the phenomena observed from several design examples that utilize different PRS types, structural parameters, and feeding sources. Such insights are essential for the design of the PRS antennas to achieve better performance.
- Current beam-reconfigurable PRS antennas suffer from some common performance limitations in terms of small beam steering range, high SLLs, and

considerable gain variations over different reconfigurable states. The beam-reconfigurable feeding sources for further deflection enhancement still use complicated phased array antennas with sizeable insertion losses.

- From practical design examples, the DS-FPC antennas with single-layer PRS cannot provide a flexible dual-band frequency ratio while retaining high antenna gain. No explanation has yet been provided for this observed limitation and a low-complexity dual-band shared-aperture scheme using PRS is needed to fill the frequency ratio gap.

Research goals for PRS antennas:

- To pursue intuitive explanations for the different effects of different PRS types and feeding sources on the antenna performance, in terms of antenna gain, beam deflection capability, and SLLs. Ray-tracing analysis has been identified as a promising tool for this purpose.
- To design a beam-reconfigurable PRS antenna with a low-complexity feeding source to achieve a larger beam deflection angle, a lower SLL and a smaller gain variation than conventional solutions. New insights on the working principles of PRS antennas from ray-tracing analysis are expected to be valuable input to this effort.
- To derive the dual-band frequency ratio gap for traditional DS-FPC antennas with single-layer PRS, given a specific reflection magnitude range for gain enhancement.
- To design a dual-band shared-aperture antenna with a more flexible frequency ratio and a simple structure to fill the frequency ratio gap derived for traditional DS-FPC antennas with single-layer PRS.

Research questions for co-designed antennas:

- Current co-designed antennas for mobile terminals suffer from poor space utilization due to the large size of the sub-6GHz antennas and the considerable area occupied by the feeding networks of mm-wave phased array antennas, which also bring extra insertion losses.
- The complex practical environment with many metal components of the mobile terminals brings challenges to the co-designed antennas, which needs to be considered in the antenna design.

Research goals for co-designed antennas:

- To co-design the sub-6GHz and mm-wave antennas with high space utilization and low-complexity structure, which will support two sub-6GHz bands and offering beam scanning for the 28GHz band.

- To evaluate the effects of several practical design considerations on the performance of the proposed co-designed antenna and suggest solutions to the observed performance issues.

1.5 Thesis Structure

This thesis focuses on the design of two types of low-complexity multiband and beam-reconfigurable antennas for beyond 5G communications, namely: (1) PRS antennas for base stations; (2) co-designed sub-6GHz and mm-wave antennas for mobile terminals. The rest of Part I of this thesis contains three more chapters, to give more details on the work performed on these two topics:

- **Chapter 2** first introduces the working principle of PRS antenna, and then presents a theoretical analysis of PRS properties. The theoretical analysis provides design guidelines for beam-reconfigurable PRS antenna and shared-aperture antenna with PRS, which are then utilized to propose new designs with state-of-the-art performances.
- **Chapter 3** briefly introduces the proposed co-designed antenna systems for mobile terminals. Then, it presents an initial investigation on techniques to achieve further performance improvements. Lastly, it summarizes the effects of practical design considerations.
- **Chapter 4** provides a summary of the main research contributions of each of the included papers and my personal contributions, as well as a few promising future research extensions of the presented work.

Part II of the thesis contains the four original research papers that cover the research areas described in Part I.

2 PRS Antenna Design for Base Stations

As mentioned in the previous chapter, PRS antennas have the advantages of high gain, simple structure, and low cost, providing great potential for application in future base stations. However, PRS antennas encounter challenges with respect to beam-reconfigurable and shared-aperture designs.

In the first section of this chapter, the working principle of conventional PRS antenna is introduced based on ray-tracing analysis. In the second section, the theory of the PRS unit cell and the effects of several PRS properties on the antenna performance are presented. These theoretical analyses clarify the working principle of the PRS and explain several of the observed phenomena in the design of PRS antennas. In the third section, an intuitive ray-tracing model for the working principle of beam deflected PRS antennas, as well as design guidelines for beam-reconfigurable PRS antennas, are provided. The final section of this chapter explains the frequency ratio limitations for traditional DS-FPC antennas that utilize single-layer PRS and presents a shared-aperture antenna design scheme to fill the frequency ratio gap.

2.1 Working Principle of Conventional PRS Antenna

2.1.1. Ray-tracing analysis considering normal incidence

As described in Section 1.2, a PRS antenna typically employs a patch antenna as the feeding source, which is printed at the center on one side of a substrate, where the other side of the substrate is used as the fully reflecting ground plane. The PRS antenna utilizes the multiple reflections of the waves between the PRS and the fully reflecting ground plane to achieve high gain performance. In the classical article

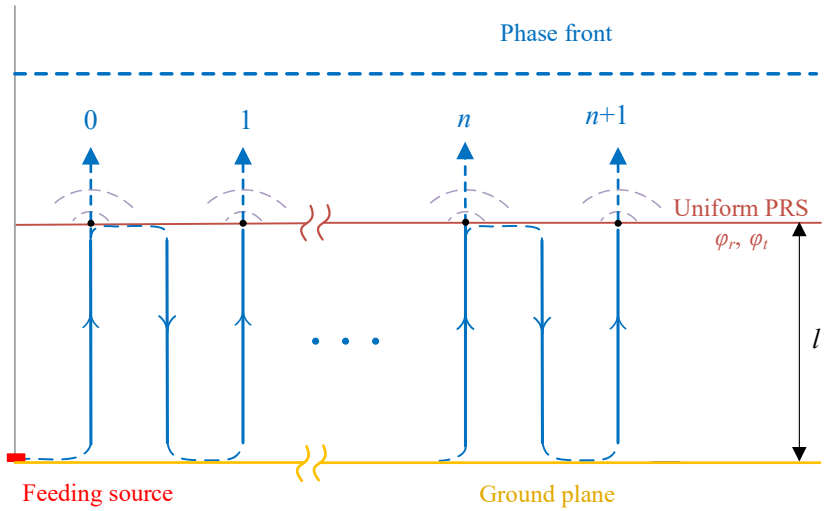

Figure 2.1: Path of ray with normal incidence and predicted phase front (only half of the PRS antenna is illustrated due to mirror symmetry).

[21], the working principle of PRS antenna is explained with a ray-tracing model where the propagating waves are represented by rays. Oblique incident angle α of the ray from the source (α is the angle between the ray and broadside direction, i.e., $\alpha \in [0°, 90°]$) is considered in the classical article. However, to simplify the theoretical analysis of directivity in the broadside direction, only the normal incident angle $\alpha = 0°$ is considered for the PRS height derivation. As shown in Fig. 2.1, the vertical ray paths are illustrated with solid lines, while the horizontal ray paths are illustrated with dash lines for the continuity of the ray paths, even though they are neither physical nor considered in the derivation.

The PRS exhibits specific reflection and transmission properties in terms of magnitudes and phases which are dependent on the unit cell shape and structural parameters. Since the reflection magnitude of the PRS is less than 1, each incident wave at the PRS is partially reflected and partially transmitted. In the process of the waves being reflected by the PRS and the ground plane, multiple transmitted waves (rays) are formed across the PRS, which can be regarded as new wave sources radiating towards the upper half space. Each ray experiences a total propagation path, consisting of multiple times of reflection on the PRS and ground plane and one time of transmission through the PRS, which causes a relative phase shift between the rays. To achieve the in-phase condition for the multiple transmitted waves, the PRS height l (the distance between PRS and ground plane) needs to be matched with the reflection phase φ_r of the PRS in a specific manner, which has been derived as [21]

$$l = \left(\frac{\varphi_r}{2\pi} - 0.5 \right) \frac{\lambda}{2} + N \frac{\lambda}{2} , \tag{2.1}$$

where λ is the wavelength in free space and $N = 0, 1, 2, \ldots$. Since the PRS antenna is also known as FPC antenna, the N in the FPC antenna's resonance condition is called the order of the FPC mode [43].

From (2.1), the PRS height l is related to the reflection phase φ_r, the order of FPC mode N, and the wavelength λ. Given the same N and a fixed wavelength λ, different reflection phases φ_r's correspond to different PRS heights l's, so the antenna height (or profile) is adjustable, providing a degree of flexibility in PRS antenna design. On the other hand, with a fixed reflection phase φ_r and wavelength λ, the FPC antenna's resonance condition can be satisfied theoretically with multiple sets of values for N and PRS height l. Since a larger N corresponds to a higher antenna profile, $N = 1$ is normally chosen to minimize l (while being a physical solution).

From the ray-tracing model depicted in Fig. 2.1, the total phase shifts of the rays and the phase difference between adjacent rays can be expressed to predict the phase distribution across the PRS, given a specific PRS height and the reflection and transmission properties of PRS. The total phase shift of ray n is the sum of the phase shifts due to the ray path, the reflections on the PRS φ_r and the ground plane π, as well as the transmission through the PRS φ_t, expressed as

$$\varphi_{rayn} = -\frac{2\pi}{\lambda}(2n+1)l + n\varphi_r + n\pi + \varphi_t , \tag{2.2}$$

where the index n ($n = 0, 1, 2, \ldots$) represents that the wave has been reflected n times before it is transmitted through the PRS. The phase difference between ray ($n + 1$) and ray n is deduced as

$$\Delta\varphi = \varphi_{ray(n+1)} - \varphi_{rayn} = -\frac{4\pi}{\lambda} l + \varphi_r + \pi . \tag{2.3}$$

It can be verified that with the PRS height l and reflection phase φ_r satisfying the FPC antenna's resonance condition in (2.1), the phase difference $\Delta\varphi$ in (2.3) becomes $-2\pi N$, where $N = 1, 2, \ldots$. The phase difference $\Delta\varphi$ takes a negative value, representing an excess phase delay of the ray ($n + 1$) relative to the ray n. Therefore, it can be concluded that the multiple transmitted rays across the PRS satisfy the in-phase condition, as depicted in Fig. 2.1.

From (2.3), given a PRS height, when the reflection phase φ_r of the utilized PRS is less than the calculated one from (2.1), more phase delay will be brought to the ray ($n + 1$) by the PRS than required, thus the absolute value of phase difference $|\Delta\varphi|$ will be greater than $2\pi N$ and no longer a multiple of 2π. In other words, the given vertical ray path length is too long to satisfy the FPC antenna's resonance condition in this case, causing more phase lag to the ray ($n + 1$) relative to the ray n. With a

similar derivation process, it can be concluded that when the reflection phase φ_r of the utilized PRS is greater than the calculated one from (2.1), the FPC antenna's resonance condition cannot be satisfied due to the insufficient phase lag to the ray (n + 1). Therefore, both smaller and larger reflection phases will cause phase front tilting as the waves are transmitted through the PRS from its center to the edges. The tilting phase distributions based on this mechanism can be utilized for the design of beam deflected PRS antennas as presented in Paper II, which will be further discussed in Section 2.3.

2.1.2. Ray-tracing analysis considering oblique incidence

In practice, the waves transmitted through the off-center positions of the PRS are from multiple oblique incident angles. As mentioned in Section 1.2, ray-tracing models accounting for oblique incidence have been used for PRS antenna designs to achieve higher gain [57] and arbitrary beam deflection angle [58]. To construct a more accurate ray-tracing model, the effect of oblique incidence is analyzed in this thesis, based on which the observed phenomena mentioned in Section 1.2.3 can be explained and a beam deflected PRS antenna with better performance can be designed.

As shown in Fig. 2.2, assuming that a ray with arbitrary incident angle α is propagating between the PRS and the ground plane, the path length for each reflection is l / cos α. From (2.3), the phase difference between ray (n + 1)′ and ray n′ becomes

$$\Delta\varphi' = \varphi_{ray(n+1)'} - \varphi_{rayn'} = -\frac{4\pi}{\lambda}\frac{l}{\cos\alpha} + \varphi_r + \pi \,. \tag{2.4}$$

The l / cos α term is larger than the vertical distance l between the PRS and the ground plane, so the ray (n + 1)′ has more excess phase delay relative to the ray n′ in the case considering the oblique incidence than the case considering only the normal incidence. Therefore, the phase front in the ray-tracing model considering the oblique incidence gradually lags the ideal uniform phase front in the simplified model considering only normal incidence, as the rays propagate from the center of PRS to the edges, as illustrated in Fig. 2.2. The phase delay at the edge of the PRS can weaken the constructive interference of waves in broadside direction, thus affecting the radiation pattern performance, e.g., decreasing the antenna gain [73].

At a particular location of the PRS, the transmitted wave is composed of rays originating from different incident angles. From (2.4), the phase difference $\Delta\varphi'$ is related to the incident angle α, so different incident angles have different effects on the phase front. The corresponding derivation details are included in Paper I, where it is concluded that the ray with a larger incident angle and a smaller number of

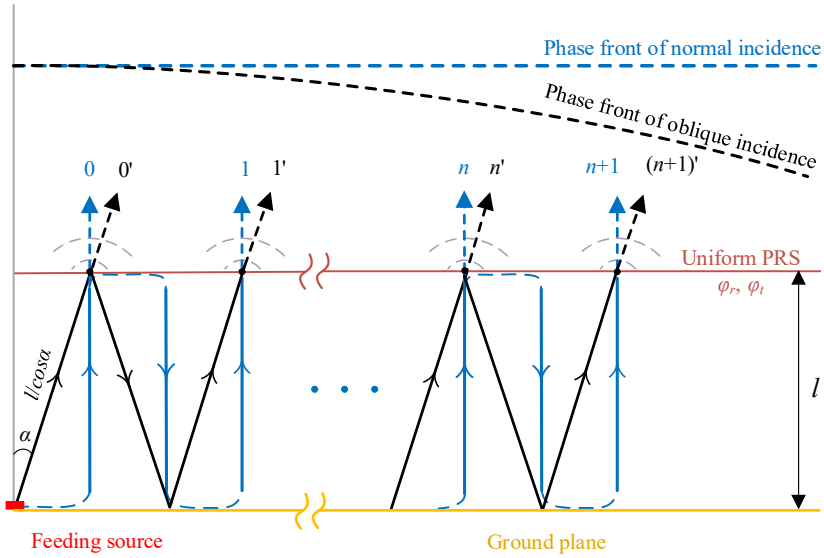

Figure 2.2: Path of ray with oblique incident angle and predicted phase front (in black), relative to that of normal incidence (in blue).

reflections causes a larger phase delay than the normal incidence at the same location of the PRS.

Since the larger incident angles correspond to larger phase delays than the normal incidence, the extent of total phase delay at a particular location of PRS, which is the sum of (complex) phasor representations of rays with multiple incident angles, depends on the proportion of the ray with larger incident angles. This proportion is derived in Paper I and is used to explain why different types of PRS influences the antenna gain performance, see further details in Section 2.2.

2.1.3. Proper reflection magnitude

From the working principle of conventional PRS antenna described above, multiple transmitted waves are formed in the process of multiple reflections between the PRS and reflecting ground plane. In addition to the requirement for the reflection phase in (2.1), the reflection magnitude of the PRS needs to take a proper value, considering that the size of the PRS is finite in practical design.

If the PRS reflection magnitude is too small, most of the waves radiated from the feeding source will be transmitted through the center part of the PRS due to insufficient reflections between the PRS and reflecting ground plane. In this case, the aperture of PRS antenna cannot be fully utilized to achieve high gain. In contrast, if the reflection magnitude of PRS is too large, the proportion of wave transmitted

through the PRS (at each wave incidence at the PRS) will be very small. The amplitude of the transmitted waves across the PRS will thus be small, and a substantial proportion of the waves will leak from the sides of the cavity formed by the PRS and the ground plane, resulting in low gain and high SLLs. According to the classical article [21], a reasonable reflection magnitude is between 0.7 to 0.9 for a uniform PRS that facilitates a broadside beam.

Therefore, the two reflection properties of a PRS, i.e., the reflection magnitude and the reflection phase, are critical parameters for the performance of PRS antennas. These PRS properties will be analyzed in detail in the next section.

2.2 PRS Properties

PRS is a type of metasurface, which is typically composed of unit cells with various metallic patterns periodically distributed on a dielectric substrate, exhibiting varying reflection and transmission properties with frequency. In this section, the PRS types and the reflection and transmission coefficients of the unit cell of a single-layer PRS are introduced, based on which the effects of PRS type on the PRS antenna performance are analyzed.

2.2.1. PRS unit cell types

The unit cell of a single-layer PRS can be considered as a two-port system regardless of its shape [47], as illustrated in Fig. 2.3. The incident and reflected plane waves on both sides are complex quantities and are related to each other as

$$\begin{bmatrix} E_1^- \\ E_2^- \end{bmatrix} = \begin{bmatrix} S_{11} & S_{12} \\ S_{21} & S_{22} \end{bmatrix} \begin{bmatrix} E_1^+ \\ E_2^+ \end{bmatrix}, \tag{2.5}$$

where the elements in the scattering matrix [S] are four scattering parameters (S-parameters) of the two-port system, corresponding to the two reflection coefficients (S_{11} and S_{22}) and two transmission coefficients (S_{21} and S_{12}) [74]. Each complex S-parameter contains magnitude (i.e., $|S_{11}|$ is reflection magnitude) and phase (i.e., $\angle S_{11}$ is reflection phase) information.

Given the specific metallic pattern of the unit cell with certain equivalent inductance and capacitance, the PRS unit cell resonates at specific frequencies with maximum reflection or transmission [75]. At the resonant frequency with maximum reflection, the unit cell is equivalent to a series LC circuit (acting essentially as a short circuit), whereas at the resonant frequency with maximum transmission, the unit cell is equivalent to a parallel LC circuit (acting essentially as an open circuit), as shown in Fig. 2.4.

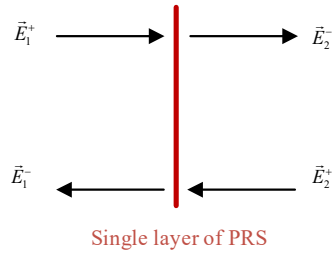

Figure 2.3: Illustration of waves on both sides of a single-layer PRS [47].

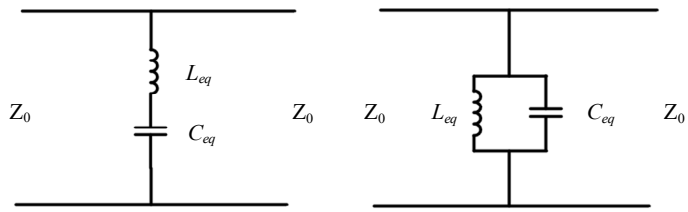

(a) (b)

Figure 2.4: Equivalent circuits of PRS unit cell at resonant frequencies with maximum (a) reflection and (b) transmission.

PRS has been classified into two types, according to the equivalent reactance of the periodic structure: capacitive PRS with reactance less than 0, and inductive PRS with reactance larger than 0 [76]. Since the metallic pattern of the unit cell has varying equivalent inductance L_{eq} and capacitance C_{eq} with frequency, the equivalent reactance and the PRS type of the unit cell also vary with frequency.

From Fig. 2.4(a), the equivalent reactance X of the unit cell near the resonant frequency with maximum reflection is

$$X = j\omega L_{eq} + \frac{1}{j\omega C_{eq}} = j\frac{\omega^2 L_{eq} C_{eq} - 1}{\omega C_{eq}} \tag{2.6}$$

The resonant frequency is $f_r = \omega_r / 2\pi = 1/2\pi\sqrt{L_{eq}C_{eq}}$, where the equivalent reactance X is 0. It can be derived from (2.6) that X takes a negative value and increases monotonically to 0^- as the frequency increases from $f_r - \Delta f$ to f_r^-, while it takes a positive value and increases monotonically from 0^+ as the frequency increases from f_r^+ to $f_r + \Delta f$, where Δf is positive and small. According to the frequency-varying trend in the equivalent reactance, it can be deduced that the PRS

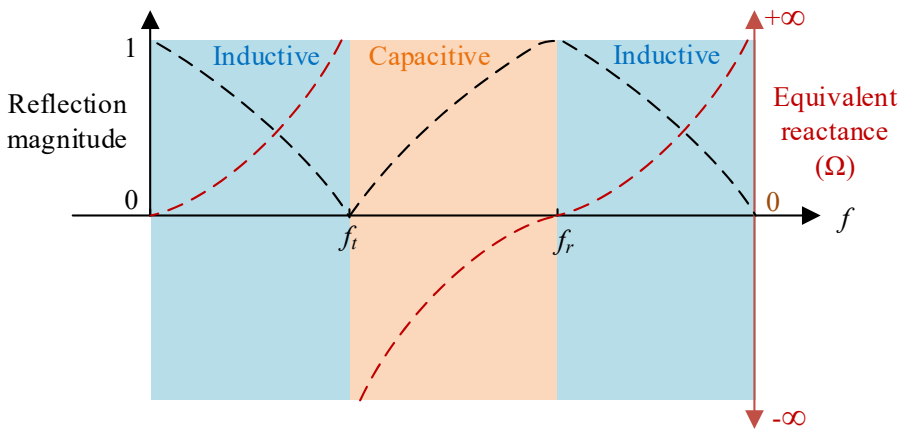

Figure 2.5: Illustration of trends in frequency-varying reflection magnitude and PRS type.

type changes from being a capacitive one to an inductive one as the frequency varies from $f_r - \Delta f$ to $f_r + \Delta f$ near the resonant frequency with maximum reflection, as illustrated in Fig. 2.5.

From Fig. 2.4(b), the equivalent reactance X of the unit cell near the resonant frequency with maximum transmission is

$$\mathrm{X} = j\omega L_{eq} \,//\, \frac{1}{j\omega C_{eq}} = j\frac{\omega L_{eq}}{1-\omega^2 L_{eq} C_{eq}} \tag{2.7}$$

The resonant frequency is $f_t = \omega_t / 2\pi = 1/2\pi\sqrt{L_{eq}C_{eq}}$, where the equivalent reactance X is infinite. It can be derived from (2.7) that the equivalent reactance X takes a positive value and increases monotonically to +∞ as the frequency increases from $f_t - \Delta f$ to f_t^-, whereas it takes a negative value and increases monotonically from -∞ as the frequency increases from f_t^+ to $f_t + \Delta f$. Therefore, near the resonant frequency with maximum transmission, the PRS type changes from being an inductive one to a capacitive one as the frequency varies from $f_t - \Delta f$ to $f_t + \Delta f$, as illustrated in Fig. 2.5.

In this section, the unit cell of single-layer PRS is analyzed based on a two-port system with equivalent circuits. The summary is as follows:

- The metallic pattern of a PRS unit cell corresponds to specific equivalent inductance and capacitance, which vary with frequency.

- The equivalent reactance of the unit cell consists of the equivalent inductance and capacitance that vary with frequency, leading to a specific PRS type at a given frequency.

2.2.2. Reflection and transmission coefficients of PRS

Based on the two-port system in Fig. 2.3, assuming that the single-layer PRS is lossless, symmetrical, and reciprocal, and neglecting the higher order harmonics of the PRS layer, the relationships between the reflection and transmission coefficients are [47]

$$S_{11} = S_{22} \text{ and } S_{12} = S_{21} \ , \tag{2.8}$$

$$S_{21} = 1 + S_{11} \ , \tag{2.9}$$

$$\angle S_{11} - \angle S_{21} = \pm \frac{\pi}{2} \ . \tag{2.10}$$

From the relationships of the S-parameters and the conversions between two-port system parameters [74], the impedance parameters (Z-parameters) Z_{11} and Z_{21} can be derived as

$$Z_{11} = Z_{21} = -\frac{S_{21}}{2S_{11}} \ . \tag{2.11}$$

Equation (2.10) gives the relationship between the reflection phase and transmission phase regardless of the reflection magnitude. With the positive sign in (2.10), (2.11) can be expressed as

$$Z_{11} = Z_{21} = j\frac{|S_{21}|}{2|S_{11}|} \ , \tag{2.12}$$

corresponding to the inductive PRS unit cell with reactance larger than 0. With the negative sign in (2.10), (2.11) can be expressed as

$$Z_{11} = Z_{21} = -j\frac{|S_{21}|}{2|S_{11}|} \ , \tag{2.13}$$

corresponding to the capacitive PRS unit cell with reactance less than 0. It is observed from (2.12) and (2.13) that $Z_{11} = Z_{21} = X_{11} = X_{21}$, which are represented with reactance X in the following.

From the above derived conclusions and the conversions between two-port system parameters [74], the S-parameter S_{11} can be expressed as

$$S_{11} = -\frac{Z_0}{Z_0 + j2X} \ , \tag{2.14}$$

and S_{21} can be expressed as

$$S_{21} = \frac{2X}{Z_0 + j2X} \ . \tag{2.15}$$

The magnitudes and phases of the S-parameters vary with the reactance X, given the fixed characteristic impedance of the surrounding media Z_0.

Given the trends in the reactance and PRS type variation with frequency as shown in Fig. 2.5, the trend in the reflection phase $\angle S_{11}$ variation can be deduced from (2.14), as shown in Fig. 2.6. It can be derived that the reflection phase ranges of capacitive and inductive PRSs are $[\pi, 3\pi/2)$ and $(\pi/2, \pi]$, respectively, with the assumptions for the PRS from [47] as mentioned earlier in this section.

Based on the phase difference between the reflection phase and transmission phase in (2.10) and the trend in the reflection phase variation shown in Fig. 2.6, the trend in transmission phase variation can be deduced, as shown in Fig. 2.7. It can be observed that the transmission phase is discontinuous between the two regions separated by a maximum reflection resonance point, while the reflection phase is discontinuous between the two regions separated by a maximum transmission resonance point.

The relationship between the reflection magnitude and transmission phase has been derived as [47]

$$|S_{11}| = \pm \sin(\angle S_{21}) \ . \tag{2.16}$$

Inserting (2.10) into (2.16), the relationship between the reflection magnitude and reflection phase can be expressed as

$$|S_{11}| = -\cos(\angle S_{11}) \ . \tag{2.17}$$

Since the reflection phase ranges of capacitive and inductive PRSs are $[\pi, 3\pi/2)$ and $(\pi/2, \pi]$, the two types of PRS have opposite trends in the reflection magnitude variation as the reflection phase decreases. For the capacitive PRS unit cell, when the reflection phase $\angle S_{11}$ decreases from $3\pi/2$ to π, the reflection magnitude $|S_{11}|$ increases from 0 to 1. For the inductive PRS unit cell, when the reflection phase $\angle S_{11}$ decreases from π to $\pi/2$, the reflection magnitude $|S_{11}|$ decreases from 1 to 0. These trends derived from (2.17) agree with the trends observed from Fig. 2.5 and Fig. 2.6. This difference between the two types of PRS leads to the different beam

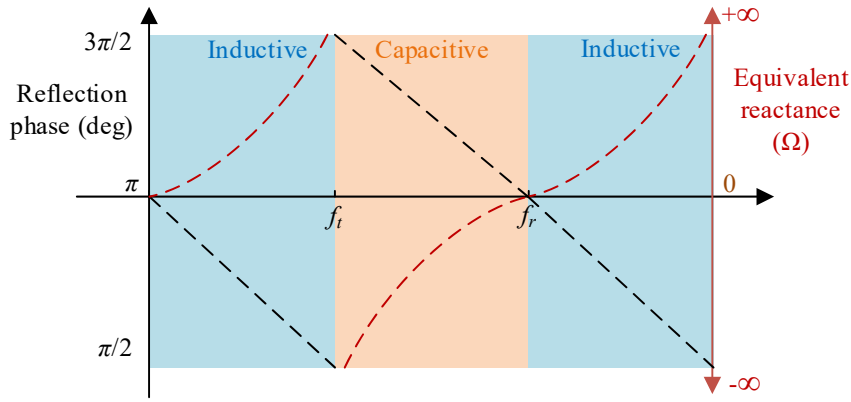

Figure 2.6: Illustration of variation trends in reflection phase and PRS type with frequency.

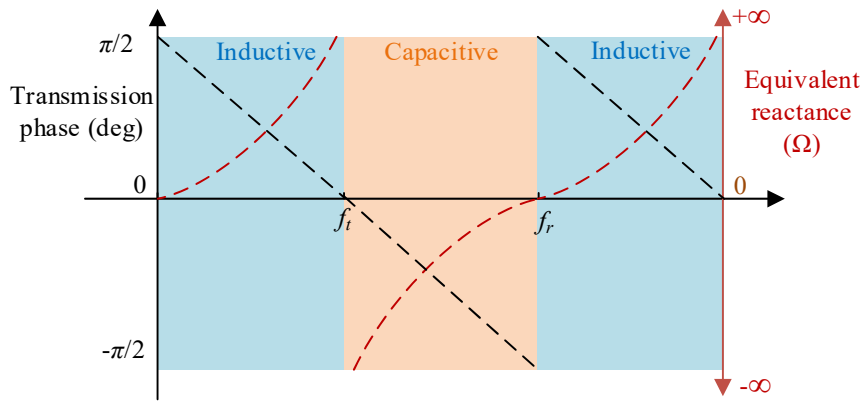

Figure 2.7: Illustration of variation trends in transmission phase and PRS type with frequency.

deflection capability for beam deflected PRS antenna, which will be discussed further in Section 2.3.

In this section, the reflection and transmission coefficients of single-layer PRS are analyzed assuming that the PRS is lossless, symmetrical, and reciprocal, and neglecting the higher order harmonics of the PRS layer. The summary is as follows:

- The reflection phase and the transmission phase have a phase difference of $\pi/2$ for an inductive PRS unit cell with reactance larger than 0 and $-\pi/2$ for a capacitive PRS with reactance less than 0.

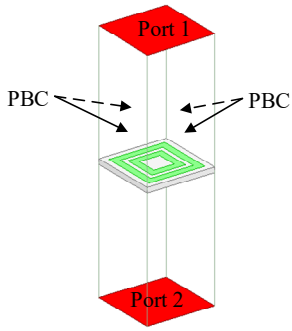

Figure 2.8: Illustration of a simulated unit cell model.

- The magnitudes and phases of the S-parameters vary with equivalent reactance, which explains why the unit cells with different metallic patterns or structural parameters exhibit different frequency responses.
- The reflection phase ranges of capacitive and inductive PRS unit cells are different, due to the different ranges of the equivalent reactance.
- The reflection magnitude of a PRS unit cell is related to the reflection phase. The capacitive and inductive PRSs have opposite trends in reflection magnitude for the same trend in the reflection phase variation.

In practical PRS antenna design, the reflection coefficients of a PRS can be evaluated using its unit cell with two Floquet ports and periodic boundary conditions (PBCs), as illustrated in Fig. 2.8. The PBCs on the four side surfaces are set to model an infinitely large PRS composed of the unit cells. In this thesis, the unit cell model is simulated using the frequency domain finite element method (FEM) solver in ANSYS HFSS.

2.2.3. Effect of PRS properties on broadside beam

From the analysis in the previous section, the capacitive and inductive PRSs exhibit different properties in terms of the reflection phase range, transmission phase range, and trends in the reflection magnitude and phase variations. Since the PRS plays an important role in the working principle of the PRS antenna, the performance of the PRS antenna is affected significantly by the PRS type. As mentioned in Section 1.2.3, it has been observed from practical design examples that the capacitive PRS exhibits higher gain than the inductive PRS for broadside beams, given the same reflection magnitude. This phenomenon can be explained based on the theoretical analysis of PRS properties in the previous section.

From (2.17), the capacitive and inductive PRSs exhibit different reflection phases for the same reflection magnitude. As can be seen from (2.1), the PRS height is determined by the reflection phase at a specific frequency, given the same order of the FPC mode *N*. Therefore, given the same reflection magnitude, the capacitive and inductive PRSs correspond to different PRS heights, which affect the magnitude and phase distribution across the PRS, as described in detail in Paper I.

First, based on a ray-tracing model accounting for oblique incident angles, it is concluded that a larger oblique incident angle causes more phase delay than a smaller one at the same location on the PRS. Then, it is proven that a larger PRS height leads to a larger proportion of power in the ray with the larger oblique incident angle, based on which the phase and magnitude distribution trends along the two types of PRSs are predicted. The derivations in Paper I show that the capacitive PRS can achieve less phase delay and more uniform magnitude distribution over the PRS, which results in higher antenna gain.

In addition to the PRS type, the reflection magnitude of the PRS also has an effect on the antenna gain for an ideal, infinitely large PRS, as mentioned in Section 1.2.3. This phenomenon can also be explained by the ray-tracing model proposed in Paper I. It is derived in Paper I that the proportion of power in the ray with the larger incident angle is inversely related to the reflection magnitude. Therefore, a larger reflection magnitude will result in a smaller proportion of power in the ray with the larger incident angle and hence a smaller phase delay at the same location on the PRS, leading to a flatter phase front. For the PRS with a larger reflection magnitude, a more uniform magnitude distribution is formed across the PRS. Therefore, the flatter phase front and the more uniform magnitude distribution lead to a superior gain.

2.3 Beam-Reconfigurable PRS Antenna Design

As mentioned in Section 1.2.1, PRS antennas can achieve beam steering by introducing reconfigurability into both the PRS and the feeding source. A reconfigurable PRS does not require a sophisticated feeding network as a conventional phased array, and a beam deflected feeding source can further enhance the beam deflection angle of the PRS antenna. A reconfigurable PRS consisting of several PRS sectors formed by different PIN diode states provides the advantage of low-complexity DC biasing network, when compared to other reconfigurable approaches. However, the existing reconfigurable PRS antennas suffer from some common performance limitations, i.e., small deflection angles, high SLLs, and considerable gain variations over different reconfigurable states. In addition, the role of a phased array in enhancing the beam deflection of a PRS antenna has not been explained analytically. Furthermore, the existing reconfigurable feeding

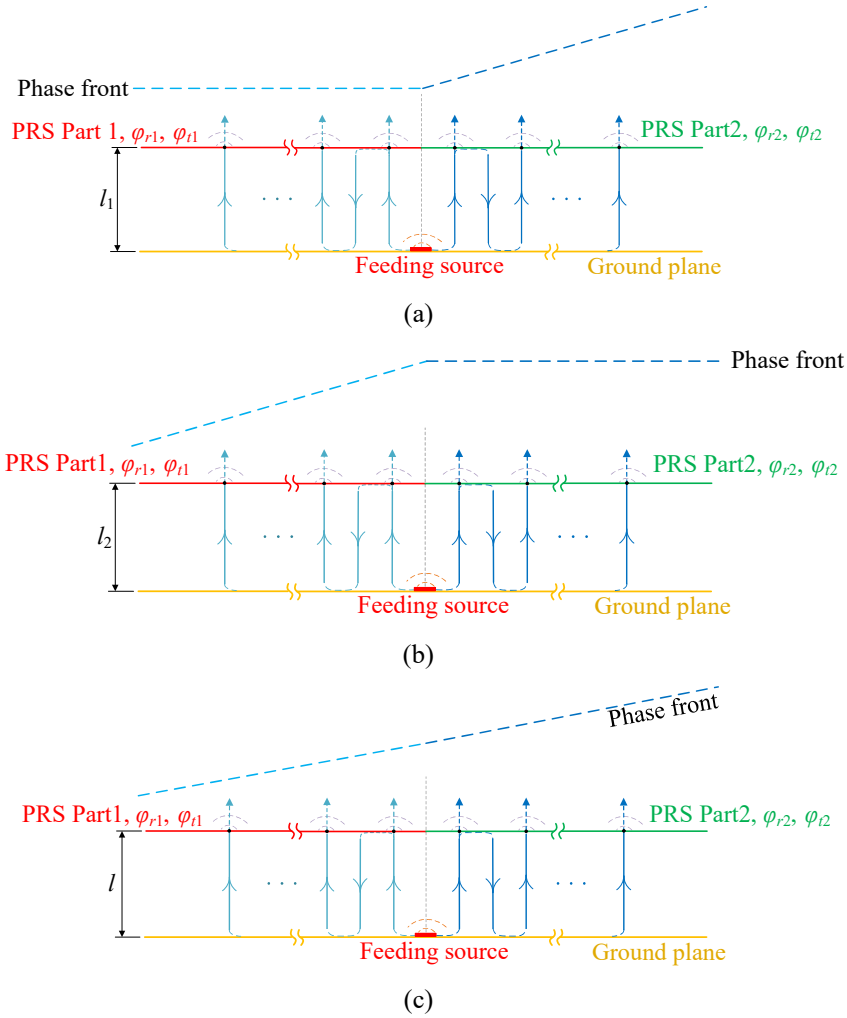

Figure 2.9: Ray-tracing models for three PRS antennas with the same two-part PRS but different PRS heights of (a) l_1, (b) l_2 and (c) l.

sources are still complicated, and they lead to extra insertion losses.

In this section, we first introduce the working principle of beam deflected PRS antenna. Next, we compare the effect of the PRS type on the beam deflection, based on the theory of PRS analyzed in Sections 2.1 and 2.2. Then, we provide a summary of the metrics used to evaluate the performance of a reconfigurable PRS antenna, as well as the trade-off between the metrics. As a supplement, we briefly explain the beam deflection enhancement effect of the feeding source and present a beam-reconfigurable feeding source with a simple structure.

2.3.1. Working principle of beam deflected PRS

The working principle of uniform PRS for the gain enhancement of broadside beam has been described in Section 2.1.1. To satisfy the FPC antenna's resonance condition, the PRS height needs to be matched to the reflection phase of the PRS as determined by (2.1). It has also been derived that a smaller or larger reflection phase of the PRS than the one calculated from (2.1) will cause phase front tilting along the PRS. Based on this mechanism, the PRS composed of two PRS parts exhibiting two different reflection phases can be used to generate tilting phase front for 1-D beam steering. The details of this beam steering effect are presented in Paper II.

Given the same PRS composed of two PRS parts, different PRS heights lead to different phase distributions and beam performances. Three cases of PRS antennas with the same PRS but different PRS heights are illustrated with three simplified ray-tracing models in Fig. 2.9, where only the normal incidence is considered. It is assumed that PRS Part 1 exhibits less reflection phase than PRS Part 2 ($\varphi_{t1} < \varphi_{r2}$), so the required PRS height l_1 for PRS Part 1 is less than the required PRS height l_2 for PRS Part 2, as calculated from (2.1).

In Case 1, where the PRS height is set to l_1, the transmitted rays are in-phase across PRS Part 1. However, since the PRS height is less than the required l_2 for PRS Part 2 to satisfy the in-phase condition, the vertical path is shorter than needed, resulting in the phase on the outer edge of PRS Part 2 leading the phase at the center, as illustrated in Fig. 2.9(a). On the contrary, in Case 2 where the PRS height is set to l_2, the transmitted rays are in-phase across PRS Part 2, whereas the vertical path is longer than needed, resulting in the phase on the outer edge of PRS Part 1 lagging the phase at the center, as shown in Fig. 2.9(b). In both cases, the PRS height is determined by one of the two PRS parts from (2.1), resulting in half of the phase front being parallel to the PRS and another half being tilted, in theory. Consequently, the phase front does not vary smoothly across the entire PRS, which can degrade the beam performance. In Case 3, the PRS height l is set using the average value of the reflection phases of the two PRS parts, which is less than the required value for PRS Part 1 and greater than the one for PRS Part 2. The phase on the outer edges of the PRS lags and leads by the same extent compared to that at the center, which facilitates a smoothly tilting phase front across the entire PRS, as illustrated in Fig. 2.9(c). Therefore, the PRS height for the two-part PRS should be set according to the average value of the two reflection phases. In addition, it can be predicted that the larger the phase difference between PRS Part 1 and Part 2, the more the phase front will be tilted, resulting in a larger beam deflection angle.

2.3.2. Effect of PRS type on beam deflection capability

From the ray-tracing analysis that only considers normal incidence in Section 2.3.1, the achieved beam deflection angle should be the same theoretically given the same

phase difference between the two PRS parts. However, when oblique incidence is considered, the beam deflection capability of the PRS antenna is also influenced by the reflection magnitudes of the two PRS parts, as will be demonstrated below.

As mentioned in Section 2.2.2, the reflection magnitude of a PRS unit cell is related to the reflection phase as expressed in (2.17). Therefore, the two PRS parts with different reflection phases also exhibit different reflection magnitudes. From the analysis of the effects of PRS properties on broadside beam in Section 2.2.3, the PRS with a smaller reflection magnitude leads to more phase delay. Therefore, for the two-part PRS, if the PRS part with a smaller reflection phase that causes phase lagging (i.e., PRS Part 1 in Fig. 2.9(c)) exhibits a smaller reflection magnitude, the phase delay at the outer edge of this PRS part resulting from an oblique incidence will increase. On the other hand, if the PRS part with a larger reflection phase that causes phase leading (i.e., PRS Part 2 in Fig. 2.9(c)) exhibits a larger reflection magnitude, the phase delay at the outer edge of this PRS part resulting from an oblique incidence will decrease. Thus, to further enhance the beam deflection effect of a nonuniform two-part PRS, it is preferred that the trend of reflection magnitude aligns with the trend of reflection phase. The details of this derivation are included in Paper II.

As concluded in Section 2.2.2, the inductive and capacitive PRSs have opposite trends in reflection magnitude for the same trend in the reflection phase. The inductive PRS has the same trend in the reflection magnitude and phase, so it can inherently leverage a larger beam deflection than the capacitive PRS due to effect of oblique incidence, given the same reflection phase difference between the two PRS parts. The above analysis provides a guideline for choosing a suitable type of PRS for better beam deflection performance.

2.3.3. Performance metrics for beam-reconfigurable PRS antenna

Beam steering capability for a PRS antenna requires multiple phase distributions realized with reconfigurable approaches. The phase distribution over the PRS and the direction of the generated beam are dependent on the reflection phase distribution of the unit cells. The analysis in Section 2.2 indicates that the reflection coefficient (i.e., magnitude and phase) of a PRS unit cell is related to its equivalent reactance.

Given different DC excitations, a PIN diode has different equivalent models in the forward (ON) state and the zero or reverse (OFF) state, as shown in Fig. 2.10. In the forward state, the PIN diode is modelled as a series LC circuit with a forward series resistance R_S and a parasitic inductance L_P. In the zero or reverse state, the PIN diode is modelled as a series circuit consisting of a parasitic inductance L_P connected in series with a parallel circuit formed by a parallel resistance R_P and a total capacitance C_T. The difference in the equivalent models enables the PIN diode to be

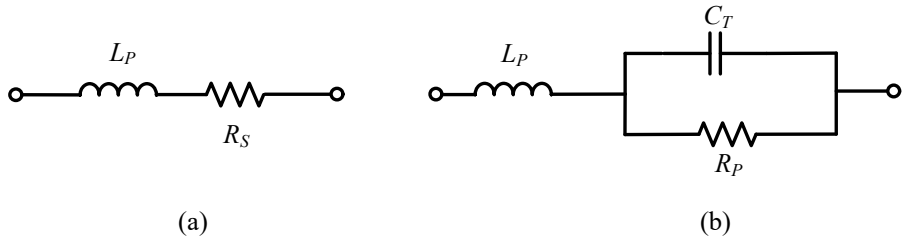

Figure 2.10: Equivalent circuits of PIN diode in (a) forward (ON) state and (b) zero or reverse (OFF) states.

used as a reconfigurable reactance element in the PRS unit cells. For a PRS unit cell loaded with PIN diodes, its equivalent reactance can be controlled to achieve reconfigurability in its reflection coefficient.

A beam-reconfigurable PRS antenna typically has one port for the feeding source and it can generate one of multiple beams in both broadside and deflected directions to cover a wide angular range. The metrics to evaluate the antenna performance mainly address two aspects: the radiation patterns and the reflection coefficients of the port over different reconfigurable states [77]. Concerning the radiation patterns, the key metrics include the maximum deflection angle, the beamwidths, the maximum directivities for different reconfigurable states, and the SLLs. These metrics can be used to evaluate whether the PRS antenna can focus the wave energy in the desired directions and provide high gain beam steering uniformly over a wide angular range. The reflection coefficients indicate the impedance matching performance of the antenna port in different reconfigurable states, which determine if the required input power can be accepted by the PRS antenna. Since the PRS properties vary for different beam directions, the corresponding reflection coefficient of the port also vary over different reconfigurable states, except between the symmetric ones. Therefore, the overlapping impedance bandwidth over the impedance bandwidths of different reconfigurable states is also an important metric, indicating if the beam steering can be realized in a specific frequency bandwidth.

From the analysis in Section 2.3.1, the PRS height for a two-part reconfigurable PRS for 1-D beam steering is determined by the average value of the reflection phases of the PRS unit cell in the ON and OFF states. However, this PRS height does not match with the reflection phase required in the FPC antenna's resonance condition when either state is selected for a uniform PRS (i.e., ON-ON or OFF-OFF), thus affecting the antenna gain and radiation pattern performance of the broadside beam. The performance degradation of the broadside beam state is evaluated in Paper II, which shows that a trade-off is needed between the broadside beam performance and the maximum deflection angle.

2.3.4. Beam deflected feeding source

Given the aforesaid design trade-off in obtaining desired properties for both broadside and deflected beams, a beam deflected feeding source can be used to deflect the beam further while retaining good broadside beam. The role of a phased array in enhancing the beam deflection in a PRS antenna is explained analytically based on a ray-tracing model in Paper II. Since each array element contributes more to the incident rays in the PRS part just above it, the phase deflected feeding source can further increase the total phase difference across the PRS, thus adding constructively to the beam deflection effect of the PRS.

As mentioned in Section 1.2.1, the existing beam deflected feeding sources that employ phased arrays have the drawbacks of complicated feeding networks and extra insertion losses. To overcome these drawbacks, the beam deflected capability of the feeding source can also be realized with parasitic elements (i.e., planar parasitic patch elements), as presented in Paper II, based on the concept of Yagi-Uda antenna [78]. The parasitic elements are loaded with PIN diodes to control its equivalent electric size. By reconfiguring the states of the parasitic elements, the capacitive coupling to the active element can be controlled, thus providing the desired phase distributions and beam reconfigurability. This beam-reconfigurable feeding source does not require a feeding network with phase shifters, leading to lower complexity. In addition, the parasitic element can introduce a second resonance, facilitating better impedance matching and/or impedance bandwidth in the PRS antenna. The details of the parasitic-element based reconfigurable feeding source are provided in Paper II.

2.4 Shared-Aperture Antenna Design Using PRS

As mentioned in Section 1.2.2, a shared single-layer PRS can be used to construct a DS-FPC antenna for high space utilization. However, it is observed from practical design examples that DS-FPC antennas with single-layer PRS suffer from limitations in the dual-band's frequency ratio. Therefore, in this section, we first analyze the feasible range of frequency ratio for traditional DS-FPC antennas with single-layer PRS. Then, we present a new dual-band shared-aperture antenna to fill the frequency ratio gap. Lastly, a summary of the metrics used to evaluate the performance of a shared-aperture antenna that utilizes PRS is provided.

2.4.1. Frequency ratio range analysis for DS-FPC antennas

For a DS-FPC antenna with a single-layer PRS, the shared PRS height l and the reflection phases φ_{rL} and φ_{rH} need to satisfy the FPC antenna's resonance condition in (2.1) in both LB and HB, which can be expressed as

$$l = \left(\frac{\varphi_{rL}}{2\pi} - 0.5 \right) \frac{\lambda_L}{2} + N_L \frac{\lambda_L}{2} \ , \tag{2.18}$$

$$l = \left(\frac{\varphi_{rH}}{2\pi} - 0.5 \right) \frac{\lambda_H}{2} + N_H \frac{\lambda_H}{2} \ , \tag{2.19}$$

where λ_L and λ_H represent the wavelengths in free space in LB and HB, respectively. Combining (2.18) and (2.19), the frequency ratio between the HB frequency f_H and the LB frequency f_L can be expressed as

$$\frac{f_H}{f_L} = \frac{\frac{\varphi_{rH}}{2\pi} - 0.5 + N_H}{\frac{\varphi_{rL}}{2\pi} - 0.5 + N_L} \ . \tag{2.20}$$

From the working principle of FPC antenna, sufficiently reflected waves are required between the PRS and the fully reflecting ground plane to achieve the high gain performance. This implies that the PRS should exhibit a sufficiently high reflection magnitude within a specific range. From the theoretical analysis of the PRS properties in Section 2.2, the reflection magnitude is related to the reflection phase as expressed in (2.17), which results in the reflection phase of the PRS being also constrained within a specific range. For a traditional DS-FPC antenna using a shared single-layer PRS, the PRS should exhibit high reflection magnitudes in both bands, where the reflection phases in both bands are all constrained to specific ranges.

From (2.20), assuming that the PRS exhibits the reflection phases of φ_{rL} and φ_{rH} in specific ranges with upper and lower boundaries, the frequency ratio is thus related to N_L and N_H, the orders of the FPC modes in the two frequency bands. This explains the observed phenomenon in the practical design examples that the achieved frequency ratio tends to be close to the ratio of the FPC mode orders in the two frequency bands, as mentioned in Section 1.2.2. Since the PRS height corresponds to a smaller wavelength in LB than in HB, the order of the FPC mode in LB is normally chosen as $N_L = 1$ to minimize the cavity height.

In this thesis, the frequency ratio range of interest is (1, 2), to cater for dual-band application combining some commonly used frequency bands, such as S-band (2-4GHz), C-band (4-8GHz), and X-band (8-12GHz). The range of feasible frequency ratio for a traditional DS-FPC antenna with single-layer PRS with $N_H = 1$ and $N_H = 2$ are calculated in Paper III. The frequency ratio gap for the two cases of N_H within the range of interest is [1.29, 1.67], given the range of reflection magnitude $\rho \in (0.707, 1)$, where there is more power in the reflected waves than the transmitted ones to facilitate gain enhancement (i.e., 0.707 corresponds to −3dB). Within the frequency ratio gap, a DS-FPC antenna with single-layer PRS is predicted to exhibit low gains due to the lack of reflection. It is also concluded that the upper boundary

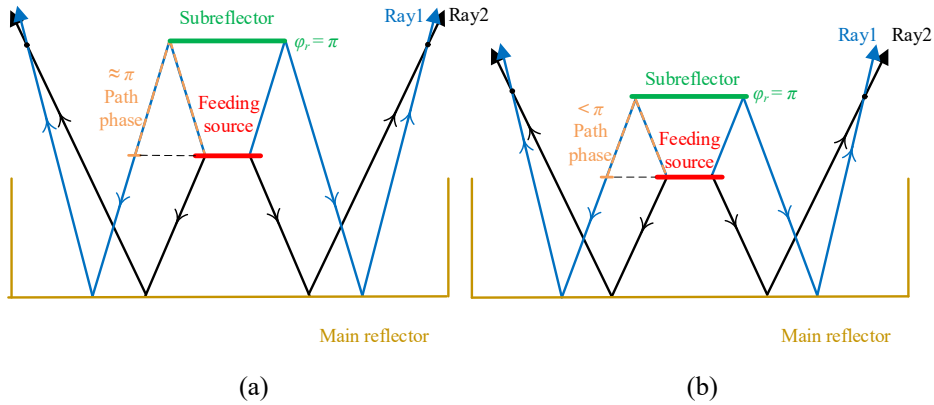

Figure 2.11: Propagation of waves in traditional SBA with (a) typical profile height and (b) reduced profile height.

of this frequency ratio gap is more challenging to achieve for a DS-FPC antenna with N_H = 1, which leads to a smaller antenna profile (i.e., a more compact implementation).

2.4.2. Dual-band shared-aperture antenna design using PRS

A dual-band shared-aperture design is proposed in Paper III, which merges a FPC antenna with a short backfire antenna (SBA) with different working principles to fill the frequency ratio gap while offering a simple structure. A PRS is designed with different reflection coefficient distributions in two frequency bands to enable different functions. The chosen frequency ratio of 1.64 is significantly larger than the upper boundary of the frequency ratio limit for N_H = 1 (1.27). The shared PRS is designed to be capacitive for the HB FPC antenna to achieve high gain [76], and the SBA is designed to work in LB by utilizing a parasitic element and the shared PRS. The HB FPC antenna works with the first-order FPC mode, facilitating a lower overall antenna height.

The PRS height as determined by the HB FPC condition is smaller than the typical 0.5 wavelength used in the traditional SBA [79], which could result in gain degradation for the LB antenna. As illustrated in Fig. 2.11, a traditional SBA consists of a main reflector, a small subreflector, and a feeding source between two reflectors. In the SBA, the waves from the feeding source are reflected by one or both reflectors and the wave components along the different paths satisfy an in-phase condition. The different path lengths of the two rays are mainly attributed to the initial upward path of Ray1 from the feeding source to the subreflector, the reflection at the metallic surface of the subreflector (giving an equivalent path phase

of π), part of the continuing downward path of Ray1 from the subreflector until it reaches the height of the feeding source. However, as the vertical distance between the subreflector and the feeding source is reduced, the in-phase condition between waves in the different paths is no longer satisfied. The nonuniform PRS proposed in Paper III can improve the gain degradation of the LB SBA by utilizing the outer PRS unit cells that are designed to offer positive and increasing transmission phase as the incident angle to the PRS increases. The details of the design methodology are included in Paper III.

2.4.3. Performance metrics for shared-aperture antenna using PRS

In this thesis, the shared-aperture antenna design with single-layer PRS focuses on generating beams in the broadside direction in two frequency bands with their respective feeding sources. The S-parameters evaluation metrics include the impedance matching bandwidths of the two feeding ports and the isolations between the LB and HB ports. The evaluation metrics of radiation pattern performance include gains and 3dB gain bandwidths of the antennas in both bands. Typically, higher gain is more desirable in HB than in LB to compensate for the higher propagation loss in HB, as mentioned in Section 1.1. The overlapping bandwidth between the 10dB impedance bandwidth and 3dB realized gain bandwidth is also an essential metric to evaluate if the dual-band antenna can meet the application requirements in terms of both the S-parameters and radiation patterns in both bands.

The flexibility of the achievable frequency ratio enables a shared-aperture design scheme to be used for more dual-band applications. In Paper III, the frequency ratio flexibility of the proposed antenna is investigated. It is concluded that by choosing proper structure parameters, the proposed antenna can realize a flexible frequency ratio to fill the frequency ratio gap of traditional DS-FPC antennas with single-layer PRS, while maintaining a low-complexity structure. A comparison of recent dual-band shared-aperture designs in terms of these metrics is given in Paper III, which indicates the advantages of the proposed antenna in terms of flexible frequency ratio, simple structure, relatively low antenna profile and high space utilization.

3 Co-Designed Antenna for Mobile Terminals

As described in Chapter 1, the existing terminal antenna co-design schemes still suffer from poor space utilization due to the large size of the sub-6GHz antennas and the considerable area occupied by the feeding networks of mm-wave phased array antennas, which also incur extra insertion losses. In this chapter, we present a co-designed sub-6GHz and mm-wave antenna system for mobile terminals with high space utilization. First, the working principles of the sub-6GHz and mm-wave antennas are introduced, respectively, after which the co-design scheme is briefly described. Then, an initial investigation is provided on techniques to achieve further performance improvements in both bands. Finally, the feasibility of the proposed co-design scheme is further evaluated by taking into account several practical design considerations.

3.1 Working Principle of Co-Designed Antennas

In the sub-6GHz bands, the terminal chassis is utilized as the main radiator and hence it plays a dominant role in the radiation properties of the antennas. Instead of using self-resonant elements, non-resonant capacitive coupling elements (CCEs) with proper matching networks have been proposed to excite the terminal chassis [81]. Non-resonant coupling elements are becoming popular to realize low band antennas due to their compactness and simple structure (see [82] and references therein). Due to their ability to couple power into the electric near-field, CCEs should be located at the region(s) where the electric field strength is maximum for the mode(s) of interest. In Paper IV of this thesis, two CCEs are utilized to excite the same wideband fundamental dipole mode of the chassis. However, different impedance matching networks are used to match the CCE ports to 50Ω to cover two non-overlapping sub-6GHz bands: 1) 0.75-1.13GHz, covering the LTE800/850/900

bands; 2) 1.70-5.30GHz, covering the LTE1700-2600 and 5G NR n77-79 bands. Since the electric field strength is maximum at the two shorter ends of the chassis for this mode, the CCEs are placed at the diagonally opposite corners of the chassis [83]. The detailed structure is presented in Paper IV.

Both the CCE size and the chassis dimensions influence the sub-6GHz antennas performance. A larger CCE size facilitates a wider bandwidth for the sub-6GHz band, so the CCE parameters are chosen considering the trade-off between the bandwidth and size [84]. The resonant frequencies of the chassis modes (especially the wideband fundamental dipole mode) of the terminal antennas in the sub-6GHz bands are affected by the chassis dimensions. If the chassis dimensions are increased, the resonant frequencies of the affected modes will decrease, which will likely reduce the resonant frequencies of the two sub-6GHz ports. However, suitable changes in the impedance matching circuits (which can be performed with the matching software BetaMatch [85], for example) can be used to restore the required bands.

A reconfigurable mm-wave antenna is proposed in Paper IV, which employs a similar structure as the feeding source of the beam-reconfigurable PRS antenna mentioned in Section 2.3, based on the concept of a Yagi-Uda antenna. The mm-wave antenna utilizes two parasitic elements loaded with PIN diodes for beam switching in two symmetrical deflected directions. Compared with the conventional phased array, the proposed beam-reconfigurable array features a low-complexity structure and occupies less space. Each mm-wave array can realize a 90-degree beam scanning range with two states of the PIN diodes. In Paper IV, the insertion losses of the PIN diode in the ON and OFF states are modelled by a 5.2Ω and a 10kΩ resistor, respectively. Instead of using the equivalent circuits, one may use the measured scattering parameters (s2p files) to model the diode properties more accurately, including its losses. The simulation radiation pattern results obtained by using the s2p file show no appreciable change to the pattern shape, but the realized gain is marginally reduced by 0.6dB due to the more accurate representation of the diode losses.

In Paper IV, the compact beam-reconfigurable mm-wave arrays are integrated onto the two corner CCEs of the sub-6GHz antennas for co-design purposes. The metal ground planes of the mm-wave arrays are shared by the corner CCEs. Choosing the diagonally displaced corners as excitation locations of the CCEs enables the four mm-wave antennas on the two CCEs to cover the complete (360-degree) field of view in a convenient manner. Furthermore, the corner placements are also intended to mitigate blockage from the user's hand(s).

In the co-designed system, due to the need of measuring the mm-wave antennas in the prototype to validate simulation results, the loading effect of the mm-wave connectors needs to be considered. Compared to the case of using an ideal port for mm-wave antenna, the real connector causes the sub-6GHz bands of the prototype

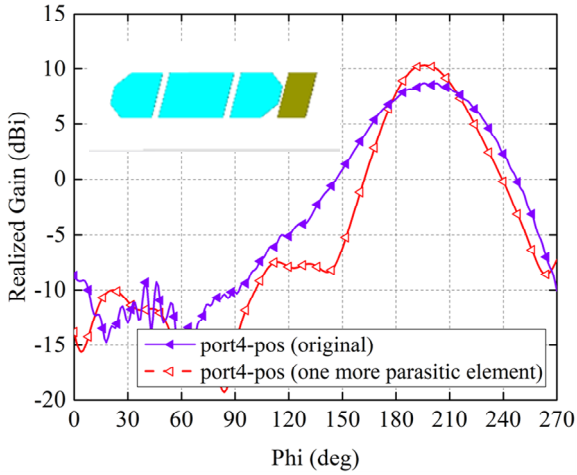

Figure 3.1: Radiation pattern of the mm-wave array with one more parasitic element, relative to the original one ("pos" indicates positive bias voltage for switching the four PIN diodes at port 4).

to shift towards lower frequencies. However, the loading of the real connector does not fundamentally change the radiation properties of the chassis, and the required bands can be restored with suitable changes in impedance matching circuits, as accomplished in Paper IV.

3.2 Investigation of Further Performance Improvements

Paper IV provides a proof-of-concept to the proposed co-design scheme with high space utilization and low-complexity structure. To explore the application potential of the proposed antenna for future mobile terminals, an initial investigation of further performance improvements is provided in this section, in terms of the impedance bandwidth and radiation pattern performance of the mm-wave array, as well as the impedance bandwidths of the two sub-6GHz antennas.

3.2.1. Investigation of mm-wave array

From the existing papers on mm-wave antennas for mobile terminal, the achieved mm-wave antenna gain is found to vary from 7 to 12.5dBi, depending on the number of antenna elements used. Typically, 8 elements would enable a 12.5dBi gain and 3 or 4 elements would offer a 7-10dBi gain. In Paper IV, the proposed mm-wave

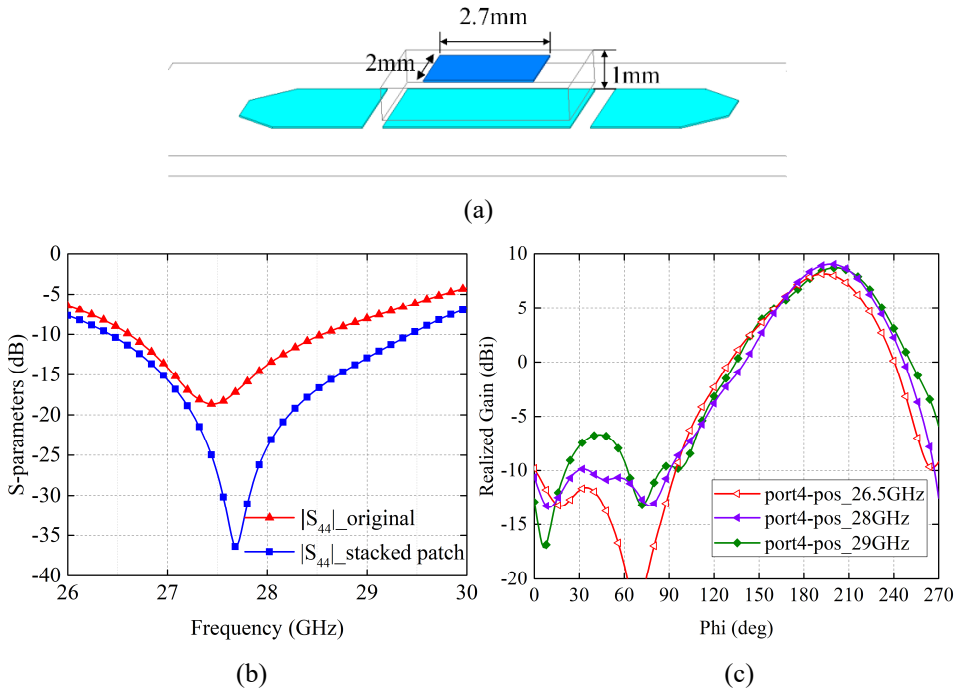

Figure 3.2: (a) Mm-wave antenna with a stacked patch antenna as the active element. (b) Re-simulated return loss in mm-wave band, relative to the original one. (c) Re-simulated radiation patterns of mm-wave array in different frequencies.

array is less capable in achieving high gain relative to a normal phased array with many (active) array elements and a feeding network. This is because only three antenna elements are utilized in the proposed mm-wave array and two of them are parasitic elements with the energy being coupled from the active element. The simulated realized gain of the mm-wave antenna at 28GHz is 9.1dBi. The measured gain is 7.9dBi, due to the losses in the PIN diodes and the slight discrepancy in the pattern shape, which are common issues in mm-wave bands. With one more parasitic element added in the proposed mm-wave antenna as shown in Fig. 3.1, the realized gain can be increased to 10.2dBi. However, the beamwidth will also decrease with higher gain, which will then require more reconfigurable states to cover the original angular range. To design such a mm-wave antenna with higher gain and more reconfigurable states is a promising direction for future work.

The mm-wave antenna proposed in Paper IV uses patch antenna elements, and the function of the parasitic elements depends on its equivalent electrical size, which makes the antenna exhibit narrowband characteristics. The simulated 10dB

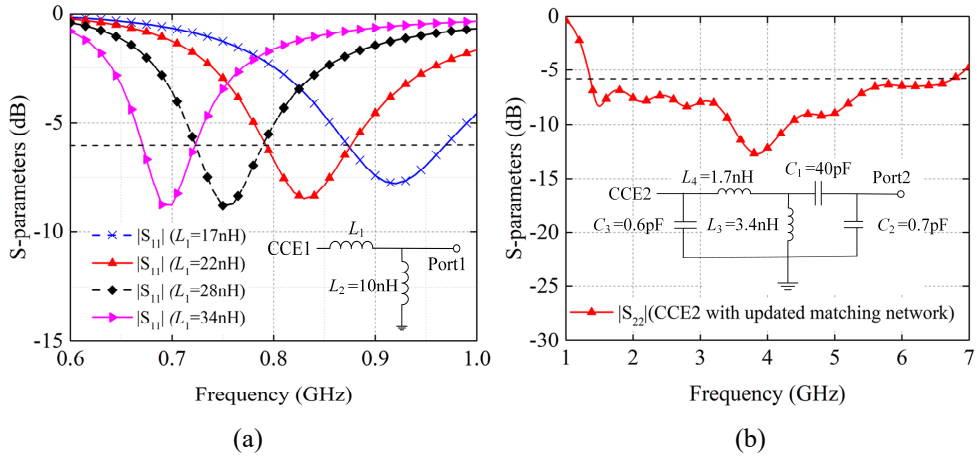

Figure 3.3: Simulated results of return losses of (a) LB antenna with a tuner and (b) HB antenna with updated matching network.

impedance bandwidth of the mm-wave antenna is around 2GHz (26.56-28.54GHz). The measured impedance bandwidth is narrower than 2GHz, due to the tolerance in the soldering of the mm-wave cables. As an attempt to show the feasibility of enhancing the bandwidth of the proposed mm-wave antenna, the regular patch antenna is replaced with a stacked patch antenna as the active element (see Fig. 3.2(a)). From the re-simulated results, the obtained impedance band is then 26.42-29.42GHz, giving around 3GHz of 10dB impedance bandwidth (see Fig. 3.2(b)). The radiation pattern is also found to be stable over the operating band (see Fig. 3.2(c)). These results shows that there is a good potential for enhancing the bandwidth of the mm-wave antenna in future work.

3.2.2. Investigation of sub-6GHz antennas

In Paper IV, the two sub-6GHz antennas cover the low band (LB: 0.79-0.96GHz) and the high band (HB: 1.7-5GHz) with two ports, respectively. More effort can be made to achieve wider bandwidths in the two sub-6GHz bands by using more matching elements or a tuner. For example, the LB from 0.69 to 0.96 GHz can be covered by using a tuneable inductor for L_1 with four different inductance values as shown in Fig. 3.3(a). The HB from 1.37 to 6.71GHz can be covered by updating the matching network with a five-element matching network in Fig. 3.3(b). These results are obtained by using the matching software BetaMatch [85].

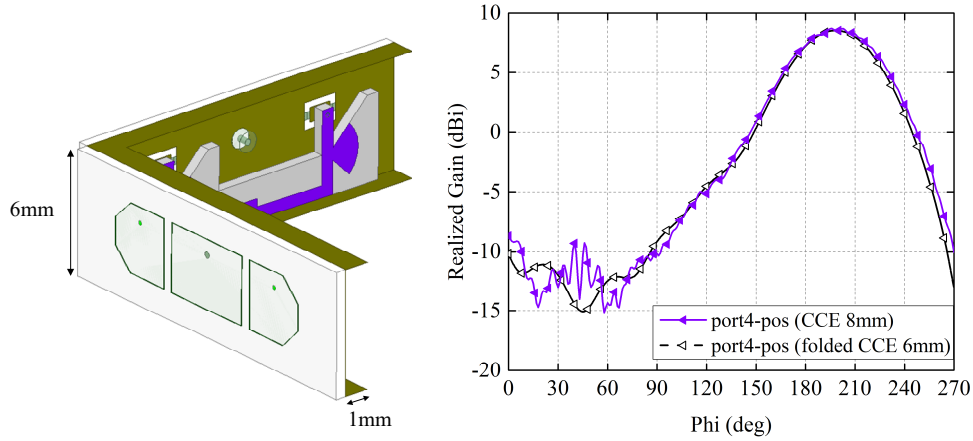

(a) (b)

Figure 3.4: (a) CCE structure with folded edges. (b) Radiation patterns of mm-wave array ("pos" indicates positive bias voltage for switching the four PIN diodes at port 4).

3.3 Effects of Practical Design Considerations

As mentioned in Section 1.3, many metal components exist in the practical environment of a mobile terminal, which may influence the performance of the antennas. The effects of several practical design considerations on the performance of the antennas proposed in Paper IV are evaluated. These considerations include the presence of the metal frame and the touch screen, and the thickness of the mobile terminal (which is related to the antenna height). Since the details on the effects of the metal frame have been included in Paper IV, the effects of the touch screen and the terminal thickness are provided in this section as a supplement.

3.3.1. Effects of frame height

The height of the frame (thickness of the mobile terminal) is chosen to be 8mm in Paper IV, which is representative of the thickness of the latest smartphones on the market. For example, based on keyword search in Google, Samsung S20 Ultra is 8.8mm thick and iPhone 13 is 7.65mm thick. When the height of the frame needs to be reduced, the top and bottom edges of the CCEs can be folded, as shown in Fig. 3.4(a). Following this approach, the frame height and the folded edges are chosen to be 6mm and 1mm, respectively, and the antennas are re-simulated. The simulation results in Fig. 3.4(b) show that the mm-wave antenna with the folded ground, which also serves as CCE, can still achieve the original radiation properties.

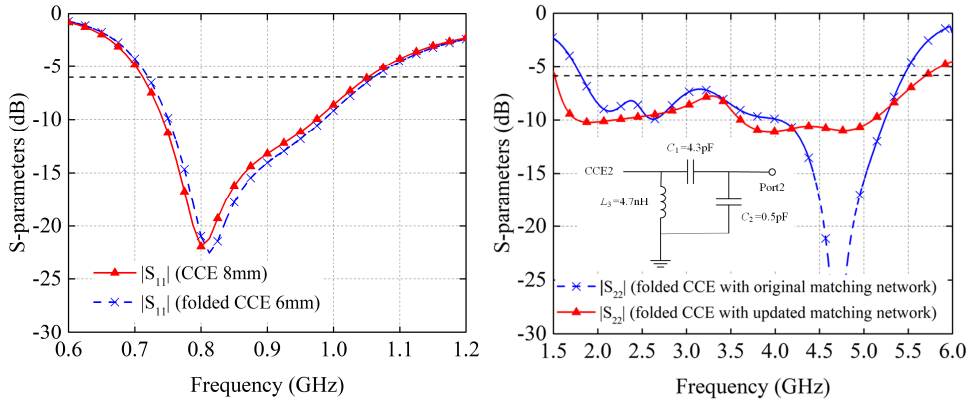

Figure 3.5: (a) Simulated results of $|S_{11}|$. (b) Simulated results of $|S_{22}|$ and updated matching network (inset).

As shown in Fig. 3.5(a), the folded CCE causes almost no change in the matching performance of the LB (0.79-0.96GHz) with the original matching network 1 proposed in Paper IV. In the HB (1.7-5GHz), the impedance matching is slightly degraded at the lower band edge with the original matching network. However, it still covers a wide HB from 1.85 to 5GHz (LTE1900-2600 and 5G NR n77-79 bands). Furthermore, the original working band in HB (1.5-5.7GHz) can be recovered by updating the matching network with the one shown in the inset of Fig. 3.5(b).

3.3.2. Effects of touch screen

A touch screen typically consists of multiple substrate layers and a grounded protective metal plate. For simplicity, it can be modelled by a metal plate due to the limited influence from the thin dielectric layers (see [86] and references therein). Therefore, to take the touch screen into account, it can be modeled by a metal plate that is of the same size as the chassis, and it is placed 4mm above the chassis (see Fig. 3.6). The metal plate is grounded to the chassis through a vertical shorting pin located at the center position.

The terminal antenna was re-simulated with this updated chassis-screen structure. Consistent to the findings of [86], the two-plate model does not affect the fundamental dipole mode of the chassis, which is the primary mode of interest in Paper IV. However, the impedance matching of the sub-6GHz antennas is affected by this addition, which can be restored by updating the matching networks as shown in Fig. 3.7. The performance of the mm-wave antenna is unaffected by the addition

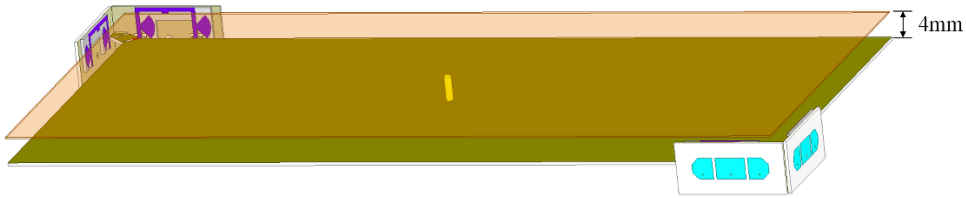

Figure 3.6: Terminal antenna with the metal plate.

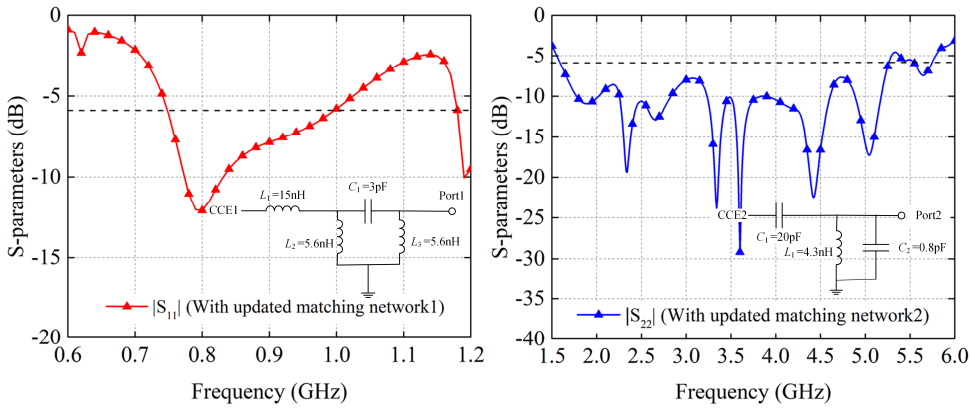

(a) (b)

Figure 3.7: Simulated results of reflection coefficients in (a) LB (port 1) and (b) HB (port 2) with metal plate and updated matching networks.

of the metal plate, due to the CCEs acting as the ground plane, shielding the mm-wave patch elements from any loading effect of the metal plate.

4 Conclusion and Outlook

This chapter briefly summarizes the work performed in each of the research papers included in this thesis, as well as a few promising future research directions. For each paper, the research contributions and my personal contributions as a co-author are highlighted.

4.1 Research Contributions

Paper I

Comparison of Capacitive and Inductive Partially Reflective Surface Antenna Using Ray-tracing

Research Contributions: In this paper, we provide an intuitive explanation for the phenomenon that the capacitive PRS facilitates a larger antenna gain for a broadside beam than the inductive PRS. We extend the classical ray-tracing approach to derive analytically that the superior gain is primarily due to the greater height of the capacitive PRS from the ground plane. The trends of the phase and magnitude distributions across the PRS are predicted from ray-tracing analysis. To verify the analytical study, the simulated phase and magnitude distributions of a capacitive and an inductive PRS antenna are produced and shown to agree with the ray-tracing analysis. This insight into the effect of PRS height on phase delay gives more clarity to the operating principle of a PRS antenna.

Personal Contributions: I am the main contributor of this paper. I performed all theoretical ray tracing derivation and ran all full-wave simulations. I took the lead in writing the paper, with guidance and support of Buon Kiong Lau.

Paper II

Beam-Reconfigurable Antenna with Inductive Partially Reflective Surface and Parasitic Elements

Research Contributions: In this paper, a simple and intuitive ray-tracing model is utilized to analyze the working principle of beam deflected PRS antenna with a nonuniform two-part PRS, based on which the beam deflection capability of different types of PRS is compared for the first time. The better beam deflection capability of the inductive PRS than that of the capacitive PRS is derived from the ray-tracing analysis and validated with full-wave simulation. The phenomenon of the beam deflected feeding source further enhancing the beam deflection angle of the PRS is also explained using ray-tracing analysis. Using the useful guidelines from the theoretical analysis, a new beam-reconfigurable PRS antenna consisting of a reconfigurable inductive PRS and a feeding source with parasitic elements is proposed, where the use of multi-element antenna and lossy feeding network is avoided in the feeding source. The proposed PRS antenna achieves a larger beam deflection angle, lower SLLs, and a smaller gain variation than the existing reconfigurable PRS antennas, while maintaining a low-complexity structure.

Personal Contributions: I am the main contributor of this paper. I conceived and developed the idea. I performed all theoretical ray-tracing derivation and ran all full-wave simulations. I planned the measurement work and the measurements were conducted by Gaonan Zhou. I took the lead in writing the paper, with guidance and support of Buon Kiong Lau.

Paper III

Dual-Band Shared-Aperture Antenna with Single-Layer Partially Reflecting Surface

Research Contributions: In this paper, the feasible frequency ratio range of traditional DS-FPC antennas with single-layer PRS is analyzed and a frequency ratio gap is derived, given a specific reflection magnitude range for gain enhancement. A dual-band shared-aperture antenna integrating a LB SBA and a HB FPC antenna with a shared single-layer PRS is then proposed to fill the gap. The PRS utilizes different unit cells for the inner and outer parts to realize different reflection coefficient distributions for different functions in LB and HB. By using the PRS and a parasitic element, a low-profile SBA working in the LB is achieved. In HB, the FPC antenna works with the first-order FPC mode. Without relying on a traditional dual-band resonance cavity, the proposed antenna achieves more flexible frequency ratio with a simple structure.

Personal Contributions: I am the main contributor of this paper. I performed all theoretical derivation and conceived the idea of antenna design. I ran all full-wave simulations. I planned the measurement work and the measurements were

conducted by Gaonan Zhou. I took the lead in writing the paper, with guidance and support of Buon Kiong Lau.

Paper IV

Co-Designed Millimeter-Wave and Sub-6GHz Antenna for 5G Smartphones

Research Contributions: In this paper, a co-designed mm-wave and sub-6GHz antenna system is proposed for 5G smartphone application. This antenna system utilizes a shared-aperture configuration to accommodate four mm-wave arrays and two sub-6GHz antennas in a compact space. The mm-wave array employs parasitic elements loaded with PIN diodes, providing beam steering capability without lossy feeding network. The CCEs that excite the sub-6GHz bands are shared by the mm-wave arrays as ground plane, facilitating high space utilization and low complexity.

Personal Contributions: I am the main contributor of this paper. I conceived the structure of mm-wave antenna and ran all simulation for the co-designed antenna system. This work is done in collaboration with Hanieh Aliakbari, who conceived the structure of sub-6GHz antenna and designed the initial matching networks. I conducted all the measurements. I took the lead in writing the paper, with guidance and support of the other co-authors.

4.2 General Conclusions

This thesis contains the results obtained from research on low-complexity PRS antennas for base stations and co-designed antenna for mobile terminals. The following are a few general conclusions and observations drawn from the research work in the two research areas.

PRS antennas:

- The superior gain of the capacitive PRS compared to the inductive PRS for a given reflection magnitude can be explained with a ray-tracing model that accounts for the oblique incidence. The capacitive PRS and the inductive PRS exhibit different phases, which correspond to different PRS heights, given the same reflection magnitude. Therefore, the capacitive PRS can achieve less phase delay and more uniform magnitude distribution over the PRS, which result in higher antenna gain.
- A ray-tracing analysis revealed that an inductive nonuniform PRS facilitates a larger beam deflection and a lower SLL than a capacitive one, given the same reflection phase difference. This is because the inductive and capacitive PRSs have opposite trends in the reflection magnitude for the same trend in the reflection phase, and the inductive PRS offers better beam performance due to

the same trend in the reflection magnitude and phase. Additional beam deflection of the PRS antenna can be provided by a beam deflected feeding source because the phase difference created by the feeding source adds constructively with that provided by the PRS.

- The reflection magnitude of the single-layer PRS is related to its reflection phase, based on the analysis of an equivalent two-ports system. The gain enhancement effect of the PRS requires high reflection magnitude, which leads to the reflection phase of the PRS being constrained to a specific range. As a result, the frequency ratio of a traditional DS-FPC antenna with single-layer PRS is also constrained to a specific range, as determined by the FPC modes. By choosing proper structure parameters, an SBA can be integrated with a FPC antenna to facilitate flexible frequency ratio to fill the frequency ratio gap, while maintaining a low profile and a simple structure.

Co-designed terminal antennas:

- It has been validated with measurements that mm-wave antennas with parasitic elements can provide adequate beam steering capability for mobile terminals. The CCEs that excite the sub-6GHz antennas can be shared by the mm-wave antennas as their ground planes, without changing the fundamental radiation modes of the chassis. The co-design scheme can still function properly after taking several practical design considerations into account, such as the presence of a metal screen and a frame, and the potential need for a thinner mobile terminal.

4.3 Future Research

Many aspects within and beyond the studied topics could be investigated further. The following is a selection of the most interesting and promising directions for future research:

PRS antennas:

- To further increase the coverage range, 2-D beam steering PRS antenna may be designed using a reconfigurable inductive PRS that consists of more parts and a 2-D beam-reconfigurable feeding source.
- Based on the existing PRS antennas in this thesis, the dual-polarization feature could be implemented to provide polarization diversity and higher data rate.
- With the clear insight into the working principle of PRS antennas as well as the PRS properties, a promising direction is to design the PRS antennas with diverse beam shapes by reconfiguring the reflection coefficient distributions across the PRS, to cater for more application scenarios.

Co-designed terminal antennas:

- A possible future work for the mm-wave antennas is to provide more refined beam steering with higher gain, by using more parasitic elements with more reconfigurable states. Multiple-input multiple-output (MIMO) operation could be added in the sub-6GHz bands of the co-designed system for higher data rate, by designing more CCEs on the terminal chassis that can excite other modes without affecting the fundamental mode.
- Based on the concept of the PRS antenna, the reconfigurable PRS could be employed in the mm-wave antenna to provide high gain beam steering, as a low-complexity alternative to phased array. However, due to the relatively large wavelength of the 28GHz band, such a concept may be more attractive and feasible for even higher bands such as the D-band, which is being considered for 6G.

Bibliography

[1] J. Navarro Ortiz, P. Romero Diaz, S. Sendra, P. Ameigeiras, J. J. Ramos-Munoz, and J. M. Lopez Soler, "A survey on 5G usage scenarios and traffic models," *IEEE Commun. Surv. Tut*., vol. 22, no. 2, pp. 905- 929, 2020.

[2] C. Yeh, G. D. Jo, Y. J. Ko, and H. K. Chung, "Perspectives on 6G wireless communications," *ICT Express*, in press.

[3] B. T. Jijo, S. R. M. Zeebaree, R. R. Zebari, M. A. M. Sadeeq, A. B. Sallow, S. Mohsin, and Z. S. Ageed, "A comprehensive survey of 5G mm-wave technology design challenges," *Asian J. Comp. Sci. Inf. Technol.*, vol. 8, no. 1, pp. 1-20, 2021.

[4] M. Z. Chowdhury, M. Shahjalal, S. Ahmed, and Y. M. Jang, "6G wireless communication systems: applications, requirements, technologies, challenges, and research directions," *IEEE Open J. Commun. Society*, vol. 1, pp. 957-975, 2020.

[5] X. Lin, *et al*., "5G new radio: unveiling the essentials of the next generation wireless access technology," *IEEE Commun. Stand. Mag.*, vol. 3, no. 3, pp. 30-37, Sept. 2019.

[6] P. Tiwari and P. K. Malik, "Design of UWB antenna for the 5G mobile communication applications: a review," in *Proc. 2020 Int. Conf, Comp. Autom. Knowl. Manag. (ICCAKM)*, 2020, pp. 24-30.

[7] K. L. Wong, H. J. Chang, C. Y. Wang, and S. Y. Wang, "Very-low-profile grounded coplanar waveguide-fed dual-band WLAN slot antenna for on-body antenna application," *IEEE Antennas Wireless Propag. Lett.*, vol. 19, no. 1, pp. 213-217, Jan. 2020.

[8] G. N. Zhou, B. H. Sun, Q. Y. Liang, S. T. Wu, Y. H. Yang, and Y. M. Cai, "Triband dual-polarized shared-aperture antenna for 2G/3G/4G/5G base station applications," *IEEE Trans. Antennas Propag*., vol. 69, no. 1, pp. 97-108, Jan. 2021.

[9] H. C. Huang and J. Lu, "Retrospect and prospect on integrations of millimeter-wave antennas and non-millimeter-wave antennas to mobile phones," *IEEE Access*, vol. 10, pp. 48904-48912, 2022.

[10] M. Shafi, *et al*., "5G: a tutorial overview of standards, trials, challenges, deployment, and practice," *IEEE J. Sel. Areas Commun.*, vol. 35, no. 6, pp. 1201-1221, June 2017.

[11] J. Helander, "Millimeter wave imaging and phased array antennas," *PhD thesis*, Lund University, Sweden, 2019.

[12] W. Hong, *et al*., "Multibeam antenna technologies for 5G wireless communications," *IEEE Trans. Antennas Propag*., vol. 65, no. 12, pp. 6231-6249, Dec. 2017.

[13] R. L. Haupt and Y. Rahmat-Samii, "Antenna array developments: a perspective on the past, present and future," *IEEE Antennas Propaga. Mag.*, vol. 57, no. 1, pp. 86-96, Feb. 2015.

[14] S. M. Moon, S. Yun, I. B. Yom, and H. L. Lee, "Phased array shaped-beam satellite antenna with boosted-beam control," *IEEE Trans. Antennas Propag*., vol. 67, no. 12, pp. 7633-7636, Dec. 2019.

[15] H. T. Chou and D. Torrungrueng, "Development of 2-D generalized tri-focal rotman lens beamforming network to excite conformal phased arrays of antennas for general near/far-field multi-beam radiations," *IEEE Access*, vol.9, pp. 49176-49188, 2021.

[16] C. C. Chang, R. H. Lee, and T. Y. Shih, "Design of a beam switching/steering butler matrix for phased array system," *IEEE Trans. Antennas Propag*., vol. 58, no. 2, pp. 367-374, Feb. 2010.

[17] A. Rudge, "Multiple-beam antennas: offset reflectors with offset feeds," *IEEE Trans. Antennas Propag*., vol. 23, no. 3, pp. 317-322, May 1975.

[18] B. Fuchs, *et al*., "Comparative design and analysis of Luneburg and half Maxwell fish-eye lens antennas," *IEEE Trans. Antennas Propag*., vol. 56, no. 9, pp. 3058-3062, Sept. 2008.

[19] M. Jiang, Z. N. Chen, Y. Zhang, W. Hong, and X. Xuan, "Metamaterial-based thin planar lens antenna for spatial beamforming and multibeam massive MIMO," *IEEE Trans. Antennas Propag*., vol. 65, no. 2, pp. 464-472, Feb. 2017.

[20] G. B. Wu, S. W. Qu, S. Yang, and C. H. Chan, "Low-cost 1-D beam-steering reflectarray with ±70° scan coverage," *IEEE Trans. Antennas Propag*., vol. 68, no. 6, pp. 5009-5014, June 2020.

[21] G. V. Trentini, "Partially reflecting sheet arrays," *IEEE Trans. Antennas Propag*., vol. 4, no. 4, pp. 666-671, Oct. 1956.

[22] R. A. Alhalabi and G. M. Rebeiz, "High-gain Yagi-Uda antennas for millimeter-wave switched-beam systems," *IEEE Trans. Antennas Propag*., vol. 57, no. 11, pp. 3672-3676, Nov. 2009.

[23] R. Li, D. Thompson, M. M. Tentzeris, J. Laskar, and J. Papapolymerou, "Development of a wide-band short backfire antenna excited by an unbalance-fed H-shaped slot," *IEEE Trans. Antennas Propag*., vol. 53, no. 2, pp. 662-671, Feb. 2005.

[24] S. V. Hum and J. Perruisseau-Carrier, "Reconfigurable reflectarrays and array lenses for dynamic antenna beam control: a review," *IEEE Trans. Antennas Propag*., vol. 62, no. 1, pp. 183-198, Jan. 2014.

[25] M. I. Abbasi, M. Y. Ismail, and M. R. Kamarudin, "Development of a PIN diode-based beam-switching single-layer reflectarray antenna," *Int. J. Antennas Propag.*, vol. 2020, no. 8891759, 2020.

[26] M. A. Towfiq, I. Bahceci, S. Blanch, J. Romeu, L. Jofre, and B. A. Cetiner, "A reconfigurable antenna with beam steering and beamwidth variability for wireless communications," *IEEE Trans. Antennas Propag.*, vol. 66, no. 10, pp. 5052-5063, Oct. 2018.

[27] H. Zhai, K. Zhang, S. Yang, and D. Feng, "A low-profile dual-band dual-polarized antenna with an AMC surface for WLAN applications," *IEEE Antennas Wireless Propag. Lett.*, vol. 16, pp. 2692-2695, 2017.

[28] B. Barakali, "Pattern and polarization reconfigurable antennas for gain enhancement," *PhD thesis*, University of Sheffield, UK, 2019.

[29] L. Leszkowska, M. Rzymowski, K. Nyka, and L. Kulas, "High-gain compact circularly polarized X-band superstrate antenna for cubesat applications," *IEEE Antennas Wireless Propag. Lett.*, vol. 20, no. 11, pp. 2090-2094, Nov. 2021.

[30] M. L. Abdelghani, H. Attia, and T. A. Denidni, "Dual- and wideband Fabry–Pérot resonator antenna for WLAN applications," *IEEE Antennas Wireless Propag. Lett.*, vol. 16, pp. 473-476, 2017.

[31] Y. Qin, R. Li, Q. Xue, X. Zhang, and Y. Cui, "Aperture-shared dual-band antennas with partially reflecting surfaces for base-station applications," *IEEE Trans. Antennas Propag*, vol. 70, no. 5, pp. 3195-3207, May 2022.

[32] M. U. Afzal and K. P. Esselle, "Steering the beam of medium-to-high gain antennas using near-field phase transformation," *IEEE Trans. Antennas. Propag*., vol. 65, no. 4, pp. 1680-1690, Apr. 2017.

[33] X. Yang, Y. Liu, H. Lei, Y. Jia, P. Zhu, and Z. Zhou, "A radiation pattern reconfigurable Fabry-Pérot antenna based on liquid metal," *IEEE Trans. Antennas Propag*., vol. 68, no. 11, pp. 7658-7663, Nov. 2020.

[34] R. Guzman Quiros, J. L. Gomez Tornero, A. R. Weily, and Y. J. Guo, "Electronically steerable 1-D Fabry-Pérot leaky-wave antenna employing a tunable high impedance surface," *IEEE Trans. Antennas Propag*., vol. 60, no. 11, pp. 5046-5055, Nov. 2012.

[35] R. Guzman Quiros, J. L. Gomez Tornero, A. R. Weily, and Y. J. Guo, "Electronic full-space scanning with 1-D Fabry-Pérot LWA using electromagnetic band-gap," *IEEE Antennas Wireless Propag. Lett*., vol. 11, pp. 1426-1429, Nov. 2012.

[36] A. Ourir, S. N. Burokur, and A. de Lustrac, "Electronic beam steering of an active metamaterial-based directive subwavelength cavity," in *Proc. 2nd Eur. Conf. Antennas Propag. (EuCAP)*, Edinburgh, U.K., Nov. 2007, pp. 1-4.

[37] L. Ji, P. Qin, J. Li, and L. Zhang, "1-D electronic beam-steering partially reflective surface antenna," *IEEE Access*, vol. 7, pp. 115959-115965, 2019.

[38] R. Guzman Quiros, A. R. Weily, J. L. Gomez Tornero, and Y. J. Guo, "A Fabry-Pérot antenna with two-dimensional electronic beam scanning," *IEEE Trans. Antennas Propag*., vol. 64, no. 4, pp. 1536-1541, Apr. 2016.

[39] P. Xie, G. Wang, H. Li, and J. Liang, "A dual-polarized two-dimensional beam-steering Fabry-Pérot cavity antenna with a reconfigurable partially reflecting surface," *IEEE Antennas Wireless Propag. Lett*., vol. 16, pp. 2370-2374, 2017.

[40] L. Ji, Z. Y. Zhang, and N. W. Liu, "A two-dimensional beam-steering partially reflective surface (PRS) antenna using a reconfigurable FSS structure," *IEEE Antennas Wireless Propag. Lett*., vol. 18, no. 6, pp. 1076-1080, Jun. 2019.

[41] L. Ji, Y. J. Guo, P. Y. Qin, S. X. Gong, and R. Mittra, "A reconfigurable partially reflective surface (PRS) antenna for beam steering," *IEEE Trans. Antennas Propag*., vol. 63, no. 6, pp. 2387-2395, Jun. 2015.

[42] T. Debogovic and J. Perruisseau-Carrier, "Array-fed partially reflective surface antenna with independent scanning and beamwidth dynamic control," *IEEE Trans. Antennas Propag*., vol. 62, no. 1, pp. 446-449, Jan. 2014.

[43] F. Meng and S. K. Sharma, "A dual-band high-gain resonant cavity antenna with a single layer superstrate," *IEEE Trans. Antennas Propag*., vol. 63, no. 5, pp. 2320-2325, May 2015.

[44] Y. Lv, X. Ding, and B. Wang, "Dual-wideband high-gain Fabry-Perot cavity antenna," *IEEE Access*, vol. 8, pp. 4754-4760, Dec. 2020.

[45] J. Chen, Y. Zhao, Y. Ge, and L. Xing, "Dual-band high-gain Fabry-Perot cavity antenna with a shared-aperture FSS layer," *IET Microw. Antennas Propag*., vol. 12, no. 13, pp. 2007-2011, Feb. 2018.

[46] C. Chen, Z. G. Liu, H. Wang, and Y. Guo, "Metamaterial-inspired self-polarizing dual-band dual-orthogonal circularly polarized Fabry-Pérot resonator antennas," *IEEE Trans. Antennas Propag*., vol. 67, no. 2, pp. 1329-1334, Feb. 2019.

[47] A. H. Abdelrahman, F. Yang, A. Z. Elsherbeni, and P. Nayeri. *Analysis and Design of Transmitarray Antennas*, Morgan & Claypool, 2017.

[48] H. Moghadas, M. Daneshmand, and P. Mousavi, "A dual-band high-gain resonant cavity antenna with orthogonal polarizations," *IEEE Antennas Wireless Propag. Lett*., vol. 10, pp. 1220-1223, 2011.

[49] B. A. Zeb, Y. Ge, K. P. Esselle, Z. Sun, and M. E. Tobar, "A simple dual-band electromagnetic band gap resonator antenna based on inverted reflection phase gradient," *IEEE Trans. Antennas Propag*., vol. 60, no. 10, pp. 4522-4529, Oct. 2012.

[50] B. A. Zeb, N. Nikolic, and K. P. Esselle, "A high-gain dual-band EBG resonator antenna with circular polarization," *IEEE Antennas Wireless Propag. Lett*., vol. 14, pp. 108-111, Sep. 2015.

[51] F. Qin, *et. al*., "A simple low-cost shared-aperture dual-band dual-polarized high-gain antenna for synthetic aperture radars," *IEEE Trans. Antennas Propag*., vol. 64, no. 7, pp. 2914-2922, Jul. 2016.

[52] M. L. Abdelghani, H. Attia, and T. A. Denidni, "Dual- and wideband Fabry-Pérot resonator antenna for WLAN applications," *IEEE Antennas Wireless Propag. Lett*., vol. 16, pp. 473-476, Jan. 2017.

[53] Z. Liu, R. Yin, Z. Ying, W. Lu, and K. Tseng, "Dual-band and shared-aperture Fabry-Perot cavity antenna," *IEEE Antennas Wireless Propag. Lett*., vol. 20, no. 9, pp. 1686-1690, Sep. 2021.

[54] A. Pirhadi, M. Hakkak, F. Keshmiri, and R. Karimzadeh Baee, "Design of compact dual band high directive electromagnetic bandgap (EBG) resonator antenna using atificial magnetic conductor," *IEEE Trans. Antennas Propag*., vol. 55, no. 6, pp. 1682-1690, Jun. 2007.

[55] J. Qi, Q. Wang, F. Deng, Z. Zeng, and J. Qiu, "Low-profile uni-cavity high-gain FPC antenna covering entire global 2.4 GHz and 5 GHz WIFI-bands using uncorrelated dual-band PRS and phase compensation AMC," *IEEE Trans. Antennas Propag*., early access. July 2022.

[56] P. Mei, S. Zhang, and G. F. Pedersen, "A dual-polarized and high-gain X-/Ka-band shared-aperture antenna with high aperture reuse efficiency," *IEEE Trans. Antennas Propag*, vol. 69, no. 3, pp. 1334-1344, Mar. 2021.

[57] J. Wu, D. Zhou, X. Lei, J. Gao, and H. Hu, "A high gain Fabry-Perot cavity antenna designed by modified ray tracking model," in *Proc. Int. Workshop Antenna Technol. (iWAT)*, Nanjing, China, Mar. 5-7, 2018, pp. 1-4.

[58] B. Ratni, W. A. Merzouk, A. de Lustrac, S. Villers, G. P. Piau, and S. N. Burokur, "Design of phase-modulated metasurfaces for beam steering in Fabry-Pérot cavity antennas," *IEEE Antennas Wireless Propag. Lett*., vol. 16, pp. 1401-1404, 2017.

[59] A. Foroozesh and L. Shafai, "Investigation into the effects of the reflection phase characteristics of highly-reflective superstrates on resonant cavity antennas," *IEEE Trans. Antennas Propag*., vol. 58, no. 10, pp. 3392-3396, Oct. 2010.

[60] A. Foroozesh and L. Shafai, "On the characteristics of the highly directive resonant cavity antenna having metal strip grating superstrate," *IEEE Trans. Antennas Propag*., vol. 60, no. 1, pp. 78-91, Jan. 2012.

[61] C. Lee, M. K. Khattak, and S. Kahng, "Wideband 5G beamforming printed array clutched by LTE-A 4 × 4-multiple-input-multiple-output antennas with high isolation," *IET Microw. Antennas Propag*., vol. 12, no. 8, pp. 1407-1413, Mar. 2018.

[62] J. Kurvinen, H. Kähkönen, A. Lehtovuori, J. Ala-Laurinaho, and V. Viikari, "Co-designed mm-wave and LTE handset antennas," *IEEE Trans. Antennas Propag*., vol. 67, no. 3, pp. 1545-1553, Mar. 2019.

[63] M. Ikram, R. Hussain, and M. S. Sharawi, "4G/5G antenna system with dual function planar connected array," *IET Microw. Antennas Propag*., vol. 11, no. 12, pp. 1760-1764, Sep. 2017.

[64] M. M. Samadi Taheri, A. Abdipour, S. Zhang, and G. F. Pedersen, "Integrated millimeter-wave wideband end-fire 5G beam steerable array and low-frequency 4G LTE antenna in mobile terminals," *IEEE Trans. Veh. Technol*., vol. 68, no. 4, pp. 4042-4046, Apr. 2019.

[65] H. Wang, "Overview of future antenna design for mobile terminals," *Engineering*, vol. 11, no. 4, 12-14, 2022.

[66] R. Hussain, A. T. Alreshaid, S. K. Podilchak, and M. S. Sharawi, "Compact 4G MIMO antenna integrated with a 5G array for current and future mobile handsets," *IET Microw. Antennas Propag*., vol. 11, no. 2, pp. 271-279, Jan. 2017.

[67] M. S. Sharawi, M. Ikram, and A. Shamim, "A two concentric slot loop based connected array MIMO antenna system for 4G/5G terminals," *IEEE Trans. Antennas Propag*., vol. 65, no. 12, pp. 6679-6686, Dec. 2017.

[68] Y. Liu, Y. Li, L. Ge, J. Wang, and B. Ai, ‘‘A compact hepta-band mode-composite antenna for sub (6, 28, and 38) GHz applications,’’ *IEEE Trans. Antennas Propag*., vol. 68, no. 4, pp. 2593-2602, Apr. 2020.

[69] M. Ikram, E. A. Abbas, N. Nguyen-Trong, K. H. Sayidmarie, and A. Abbosh, “Integrated frequency-reconfigurable slot antenna and connected slot antenna array for 4G and 5G mobile handsets,” *IEEE Trans. Antennas Propag*., vol. 67, no. 12, pp. 7225-7233, Dec. 2019.

[70] R. M. Moreno, *et al*., “Dual-polarized mm-wave endfire antenna for mobile devices,” *IEEE Trans. Antennas Propag*., vol. 68, no. 8, pp. 5924-5934, Aug. 2020.

[71] R. C. Rocio, S. Zhang, K. Zhao, and G. F. Pedersen, “Mm-wave beam-steerable endfire array embedded in a slotted metal-frame LTE antenna,” *IEEE Trans. Antennas Propag*., vol. 68, no. 5, pp. 3685-3694, May 2020.

[72] S. Zhang, I. Syrytsin, and G. F. Pedersen, “Compact beam-steerable antenna array with two passive parasitic elements for 5G mobile terminals at 28 GHz,” *IEEE Trans. Antennas Propag*., vol. 66, no. 10, pp. 5193-5203, Oct. 2018.

[73] C. A. Balanis, *Antenna Theory Analysis and Design*, 3rd ed., John Wiley & Sons, 2005.

[74] D. M. Pozar, *Microwave Engineering*, 3rd ed., John Wiley & Sons, Inc., 2005.

[75] B. A. Munk, *Frequency Selective Surfaces: Theory and Design*, John Wiley & Sons, 2000.

[76] L. Zhou, X. Chen, Y. Cui, and X. Duan, “Comparative effects of capacitive and inductive superstrates on the RCA’s gain,” *IET Microw. Antennas Propag*., vol. 12, pp. 1834-1838, May 2018.

[77] IEEE145-2013, *IEEE Standard Definition of Terms for Antennas*, Antenna Standards Committee of the IEEE Antennas and Propagation Society, Dec. 1993.

[78] J. Huang and A. C. Densmore, “Microstrip Yagi array antenna for mobile satellite vehicle application,” *IEEE Trans. Antennas Propag*., vol. 39, no. 7, pp. 1024-1030, Jul. 1991.

[79] R. Li, D. Thompson, M. M. Tentzeris, J. Laskar, and J. Papapolymerou, “Development of a wide-band short backfire antenna excited by an unbalance-fed H-shaped slot,” *IEEE Trans. Antennas Propag*., vol. 53, no. 2, pp. 662-671, Feb. 2005.

[80] G. Zhou, B. Sun, Q. Liang, Y. Yang, and J. Lan, “Beam-deflection short backfire antenna using phase-modulated metasurface,” *IEEE Trans. Antennas Propag*., vol. 68, no. 1, pp. 546-551, Jan. 2020.

[81] J. Villanen, J. Ollikainen, O. Kivekas, and P. Vainikainen, "Coupling element based mobile terminal antenna structures," *IEEE Trans. Antennas Propag*., vol. 54, no. 7, pp. 2142-2153, Jul. 2006.

[82] H. Aliakbari and B. K. Lau, "Low-profile two-port MIMO terminal antenna for low LTE bands with wideband multimodal excitation," *IEEE Open Journal of Antennas and Propag*., vol. 1, pp. 368-378, 2020.

[83] R. Valkonen, M. Kaltiokallio, and C. Icheln, "Capacitive coupling element antennas for multi-standard mobile handsets," *IEEE Trans. on Antennas Propag*., vol. 61, no. 5, pp. 2783-2791, May 2013.

[84] H. Aliakbari and B. K. Lau, "Impact of capacitive coupling element design on antenna bandwidth," in *Proc. 12th Europ. Conf. Antennas Propag. (EuCAP)*, London, UK, Apr. 9-13, 2018, pp. 1-4.

[85] Betamatch. (2019). MNW Scan Pte Ltd, Version 3.7.6. Accessed: Nov. 11, 2021. [Online]. Available: http://www.mnw-scan.com

[86] H. Aliakbari, L. Y. Nie, and B. K. Lau, "Large screen enabled tri-port MIMO handset antenna for low LTE bands," *IEEE Open J. Antennas Propag.*, vol. 2, pp. 911-920, Aug. 2021.

Part II

Included Papers

Paper I

Comparison of Capacitive and Inductive Partially Reflective Surface Antenna Using Ray-Tracing

A partially reflective surface (PRS) antenna is a low-cost high gain antenna, which is often classified by the capacitive or inductive nature of the PRS. It has been shown that, for a given reflection magnitude, capacitive PRS facilitates a larger antenna gain than inductive PRS, based on leaky-wave model and practical design examples. In this paper, we extend the classical ray-tracing approach to derive analytically that the superior gain is primarily due to the greater height of the capacitive PRS from the ground plane, which leads to a smaller phase delay and a more uniform magnitude distribution across the PRS. To verify the analytical study, the simulated phase and magnitude distributions of a capacitive and an inductive PRS antenna were produced and shown to agree with the predicted trends of the phase and magnitudes distributions from ray-tracing. The gain of the antenna with the capacitive PRS is 16.6dBi, which is 1.8dBi higher than that of the antenna with the inductive PRS. This insight on the effect of PRS height on phase delay gives more clarity to the operating principle of PRS antenna.

©2022 IEEE. Reprinted, with permission, from
Qiuyan Liang and Buon Kiong Lau,
"Comparison of Capacitive and Inductive Partially Reflective Surface Antenna Using Ray-Tracing,"
in *Proc. 16th Europ. Conf. Antennas Propag. (EuCAP'2022)*, Madrid, Spain, Mar. 27- Apr. 1, 2022.

1 Introduction

A partially reflective surface (PRS) antenna, consisting of a feeding source, a PRS and a completely reflecting ground, can be used to provide high directivity with simple structure and low cost [1]. According to the classical working principle of PRS antenna, the waves from the feed are reflected multiple times between the PRS and the ground, with each incident wave at the PRS also producing a transmitted wave. The PRS is designed so that the multiple transmitted waves are in-phase over the PRS, thus achieving high directivity in the broadside direction.

PRSs have been classified into two types according to the equivalent susceptance of their periodic structures: capacitive PRS with susceptance larger than 0, and inductive PRS with susceptance less than 0 [2], [3]. Based on the analysis of different unit cell structures, it has been observed that the capacitive PRS exhibits higher gain than inductive PRS, for a given reflection magnitude [4], [5]. This observation has been explained using the leaky-wave model [3], with the PRS antenna being modelled as a (leaky) waveguide surrounded by the PRS and ground. It is concluded that the capacitive PRS offers a smaller propagation constant, which leads to a bigger radiation aperture and a smaller variation of the aperture field phase, thus resulting in a higher gain.

In the classical article that first proposed PRS antenna [1], its working principle and design parameters are all based on an intuitive ray-tracing (or ray-tracking) model. However, the emphasis is on the ray with normal incidence at the PRS. Ray-tracing has also been used to in many subsequent designs of such antennas [6]-[8]. In [7] and [8], rays from oblique angles are utilized to achieve higher gain and beam-steering, showing the usefulness of accounting for oblique incidence.

In this work, we apply the general model with oblique incident rays to offer an alternative and arguably more intuitive explanation for the superior antenna gain afforded by capacitive PRS over inductive PRS, than that provided using the leaky-wave model [3]. The phase delay distribution of rays with different oblique incident angles, which is not considered in the classical work [1], is studied in detail using ray-tracing. When considering capacitive PRS and inductive PRS designed with different reflection phases but the same reflection magnitude, different phase delay and magnitude distributions are observed over the surface, resulting in different antenna gains. Ray-tracing reveals that the higher gain of the capacitive PRS is attributed to its greater height above the ground than the inductive PRS, which provides more uniform phase delay and magnitude distributions across the PRS. This in turn facilitates more uniform wave fronts across the PRS, leading to higher antenna gain. The capacitive and inductive PRS antennas were simulated in a full-wave solver to verify the predicted trends in the phase delay and magnitude distributions.

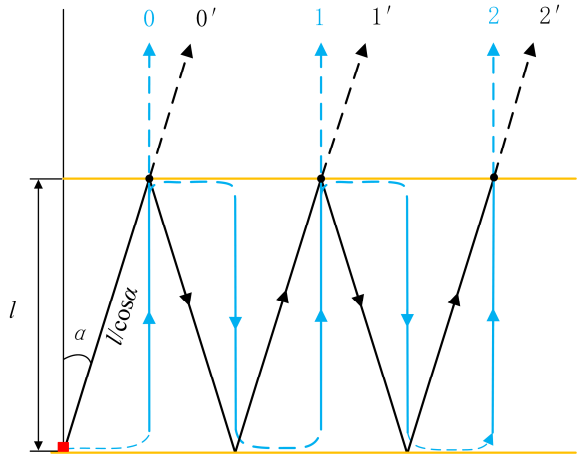

Figure 1: Path of the ray with oblique incident angle (in black), contributing to phase delays across the PRS, relative to that of normal incidence (in blue).

2 Derivation of Phase Delay Distribution

In the following, the influence of the incident angle of a single ray on the phase delay distribution is derived. This result is then extended to compare the phase delays of multiple rays transmitted by the PRS at the same point. Finally, the impact on the phase delay from a ray of a larger incident angle is demonstrated. These basic results are then utilized in Section 3 to explain the superior antenna gain facilitated by capacitive PRS.

2.1 Phase Delay Analysis of Rays with Oblique Incidence

The original ray-tracing analysis framework allowed for an arbitrary incident angle α of the ray from the source (α is the angle between the ray and broadside direction, i.e., $\alpha \in [0°, 90°]$) [1]. However, to simplify the theoretical analysis of directivity in the broadside direction, only the normal incident angle $\alpha = 0°$ is considered. According to this assumption, the path length of the reflected ray between the PRS and completely reflecting ground is equal to the vertical distance l (or PRS height), which means the ray will never go beyond the center of the PRS even after multiple reflections. To assume otherwise would be unphysical, as illustrated by the dashed blue (horizontal) part of the ray path in Fig. 1. The transmitted wave rays drawn in the figure are only used to distinguish the initial angle of incidence. Each transmitted wave does not continue to propagate along this initial angle. Instead, it can be regarded as a new source re-radiating in the upper half space.

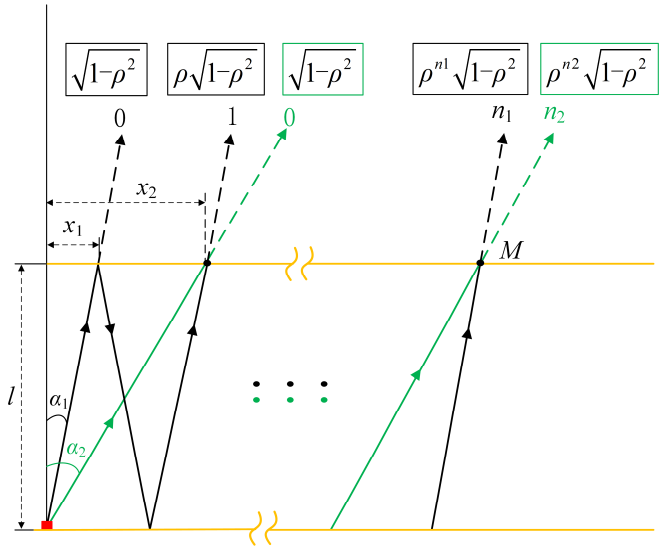

Figure 2: Paths of rays with two different oblique incident angles (in black and green, respectively), giving different phase delay distributions across the PRS. The proportions of power in the transmitted rays are also indicated, with ρ being the reflection magnitude of the PRS.

In practice, the waves transmitted through the off-center positions of the PRS are from oblique incident angles, with path lengths in odd multiples of $l/\cos\alpha$, which cause phase discrepancies along the PRS compared with the simplified model that assumes $\alpha = 0°$. To simplify the analysis, it is assumed that the reflection and transmission phase and magnitude of the PRS are independent of the incident angle. The phase delay between the practical ray n' and the simplified ray n can be expressed as

$$\Phi_n = \frac{2\pi}{\lambda}(2n+1)l\left(1-\frac{1}{\cos\alpha}\right), \tag{1}$$

where λ is the wavelength in free space and n = 0, 1, 2, etc. When the ray is from the incident angle of $\alpha > 0°$, the phase error Φ_n takes a negative value, representing an excess phase delay of ray n' relative to the simplified ray n. The ray with a constant incident angle has more delay when it is reflected more times (corresponding to a larger n), This explains why the edge position at PRS has more phase delay than the middle position. Moreover, this result can be used to analyze the dependence of phase delay on oblique incident angle, for a given location on the PRS.

2.2 Phase Delays of Rays with Different Incident Angles

At a particular location of the PRS, the transmitted wave is composed of rays originating from different angles. These rays are reflected by different numbers of times and arrive at the same location with different ray indices. In such a condition, their incident angles are related to each other in a specific manner. Two rays with incident angles of α_1 and α_2 ($\alpha_2 > \alpha_1$), as depicted in Fig. 2, can be used to explain this relationship. Ray 0 of these two rays arrive at the PRS with the distances of x_1 and x_2 from the center, respectively, and these distances can be related to the incident angles and l as

$$l = \frac{x_1}{\tan\alpha_1} = \frac{x_2}{\tan\alpha_2}. \tag{2}$$

If the ray 1 with incident angle of α_1 meets ray 0 with incident angle of α_2 at x_2, then x_1 and x_2 should satisfy the following equation

$$x_2 = 3x_1. \tag{3}$$

Similarly, if ray n_1 with the incident angle of α_1 meets ray n_2 with the incident angle of α_2 at point M, the relationships in (2) and (3) can be generalized as follows

$$(2n_2+1)x_2 = (2n_1+1)x_1, \tag{4}$$

$$\tan\alpha_2 = \frac{2n_1+1}{2n_2+1}\tan\alpha_1. \tag{5}$$

From (1) and (2), the phase delay of ray n_1 with the incident angle of α_1 and that of ray n_2 with the incident angle of α_2 can be expressed as follows

$$\Phi_{n1} = \frac{2\pi}{\lambda}(2n_1+1)x_1 G(\alpha_1), \tag{6}$$

$$\Phi_{n2} = \frac{2\pi}{\lambda}(2n_2+1)x_2 G(\alpha_2), \tag{7}$$

$$G(\alpha) = \frac{1}{\tan\alpha}\left(1 - \frac{1}{\cos\alpha}\right). \tag{8}$$

Since the function $G(\alpha)$ with $\alpha > 0°$ is a monotonically decreasing function of variable α, it can be proven using (4) that $\Phi_{n2} < \Phi_{n1}$, which means that the ray n_2 with a larger incident angle causes a larger phase delay than the ray n_1 at point M. However, the net impact of the phase delay due to the two rays transmitted through a point M is dependent on the proportion of power in these rays, which will be explored next.

2.3 Impact of Phase Delay from Increasing Power in a Ray with a Larger Incident Angle

Assuming no transmission loss and the total ray at point M to be composed of only ray n_1 and ray n_2, with the amplitudes of the ray n_1 and ray n_2 being proportional to $\rho^{n_1}\sqrt{1-\rho^2}$ and $\rho^{n_2}\sqrt{1-\rho^2}$ at point M, then the proportion of power in ray n_2 can be expressed as

$$\beta(\alpha_2)=\frac{\rho^{2n_2}(1-\rho^2)f^2(\alpha_2)}{\rho^{2n_1}(1-\rho^2)f^2(\alpha_1)+\rho^{2n_2}(1-\rho^2)f^2(\alpha_2)}, \tag{9}$$

where ρ is the reflection magnitude of the PRS and $f^2(\alpha)$ represents the power pattern of the feeding element source at the angle α. The denominator of (9) represents the total power of the waves from both angles α_1 and α_2. Dividing (9) by $\rho^{2n_2}(1-\rho^2)f^2(\alpha_2)$ in the numerator and denominator, it can be seen that (9) is dependent on (n_1-n_2).

Equation (9) can be further expressed in terms of ray n_2 by inserting (2) and (4) into (9) to remove n_1, resulting in

$$\beta(\alpha_2)=\frac{f^2(\alpha_2)}{\rho^{(2n_2+1)\left(\frac{\tan\alpha_2}{\tan\alpha_1}-1\right)}f^2(\alpha_1)+f^2(\alpha_2)}. \tag{10}$$

From (10), it can be deduced that, if the two rays maintain the incident angles of α_1 and α_2, the proportion of power in ray n_2 increases with its index n_2. This causes a larger total phase delay since ray n_2 has more phase delay than ray n_1 at point M according to Section 2.2. This conclusion can be proven by the addition of (complex) phasor representations of these rays.

3 Phase Delay Distributions of Different PRSs

3.1 Phase Delay Analysis of Different PRSs

As shown in Fig. 3, a typical PRS unit cell composed of two metal loops was used to analyze the difference between the capacitive and inductive PRS at the operating frequency of 5.5 GHz. The substrate used for the PRS is F4BM-2 (ε_r = 2.55, tan δ = 0.001) with the thickness of 1.5 mm. As the structural parameter l_o changes, the unit cell exhibits different reflection magnitudes and phases (see Fig. 4). Figure 5 presents the equivalent reflection reactance variation of the unit cell, indicating that the unit cell becomes inductive with increasing l_o. A reasonable reflection

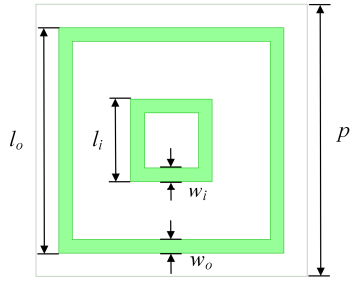

Figure 3: Structure of the unit cell.

Table 1: Parameters of capacitive and inductive unit cells. (Unit: mm)

Unit cell	l_o	l_i	w_o	w_i	p
Capacitive	12.2	6	1	1	20
Inductive	16.6	6	1	1	20

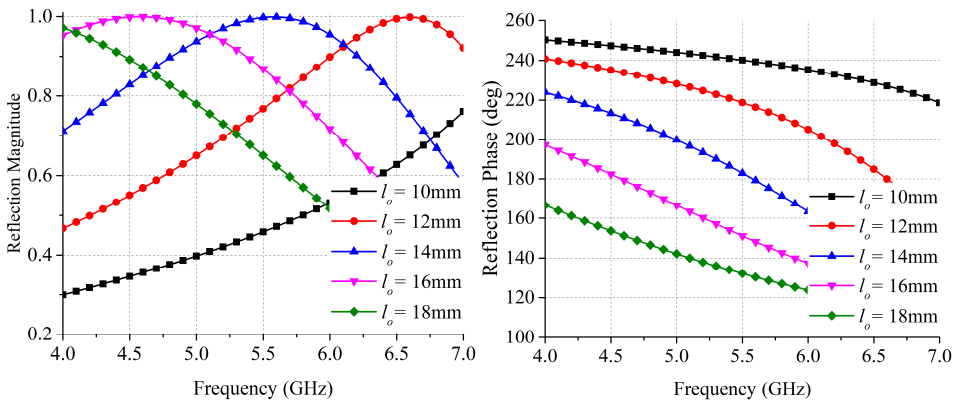

(a) (b)

Figure 4: Reflection (a) magnitude and (b) phase variation with different l_o.

magnitude for a uniform PRS is between 0.7 to 0.9 [1], so the reflection magnitude of 0.8 was chosen for the capacitive and inductive PRS unit cell, based on which lo was determined to be 12.2 mm and 16.6 mm for the capacitive and inductive unit cells, respectively. The parameters of the unit cells are provided in Table 1.

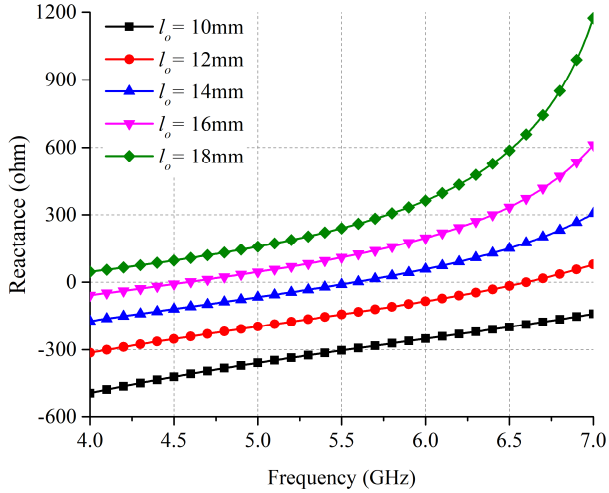

Figure 5: Reactance variation of unit cells with different l_o.

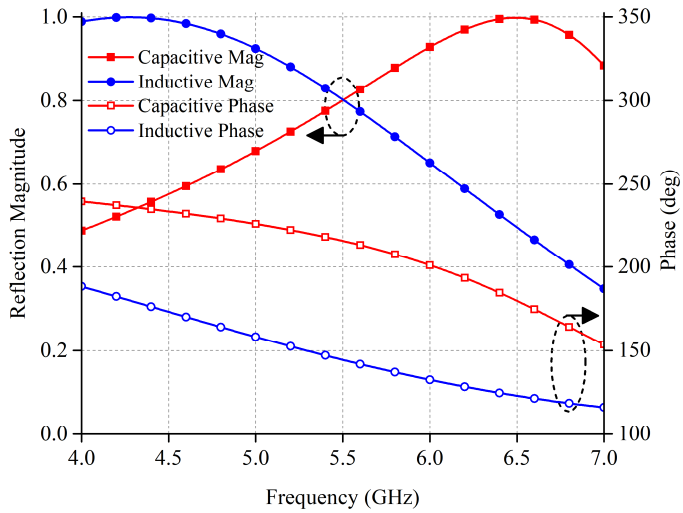

Figure 6: Reflection magnitude and phase of capacitive and inductive unit cells.

As shown in Fig. 6, at the operating frequency of 5.5 GHz, the capacitive unit cell has the reflection phase of $\varphi_{rc} = 216°$ and the inductive unit cell has the reflection phase of $\varphi_{ri} = 144°$. The capacitive unit cell always has a larger reflection phase than the inductive one, given the same reflection magnitude, since its fully reflecting resonant frequency due to the outer loop is higher. The required height of the PRS

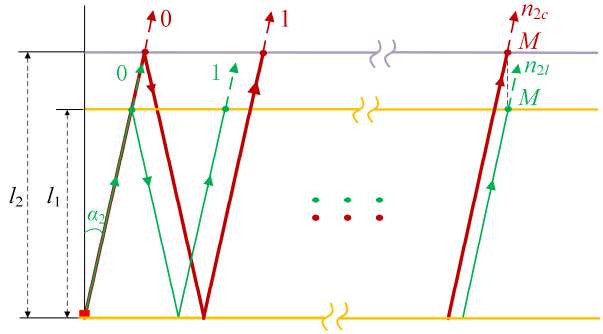

Figure 7: Propagation of ray with same incident angle along PRSs of different heights.

from the ground (to achieve co-phase transmitted waves assuming $\alpha = 0°$) can be calculated using to the classical equation [1]

$$l = \left(\frac{\varphi_r}{360} - 0.5 \right) \frac{\lambda}{2} + N \frac{\lambda}{2} , \tag{11}$$

where $N = 0, 1, 2$, etc. Choosing $N = 1$ to minimize the PRS height (while being a physical solution), the capacitive PRS has a larger height ($l_2 = 30$ mm) than the inductive one ($l_1 = 24.5$ mm).

For each PRS antenna of a given height, the proportion of power in the ray with index n_2 can be calculated using (10), showing that a larger index n_2 gives more proportion of power. As shown in Fig. 7, when the ray with the same incident angle of α_2 arrive at the same point M on the capacitive and inductive PRSs with different heights, the index of ray n_{2l} on the inductive PRS will be larger than n_{2c} on the capacitive one, because the inductive PRS is lower than the capacitive one (i.e., $l_1 < l_2$). Therefore, the proportion of power in the ray with the (same) incident angle of α_2 is larger for the inductive PRS than the capacitive one. Since the ray n_2 with the incident angle of α_2 causes more phase delay than the ray n_1 at point M, based on the derivation in Section 2.2 (for a given PRS height), the total phase delay is larger on the inductive PRS for a given surface location on the two PRSs.

Similarly, the index of ray with the incident angle of α_1 on the inductive PRS is also larger than the capacitive one. With smaller n_1 and n_2, the capacitive PRS obtains a larger total power of rays with the two incident angles at point M, as can be calculated from the denominator of (9). This result indicates that the capacitive PRS can achieve more uniform magnitude distribution than the inductive one, which facilitates a bigger radiation aperture. The predicted behavior of the phase and magnitude distributions for the two different PRSs based on ray-tracing agree well with the conclusion in [3], which is obtained by a leaky wave model.

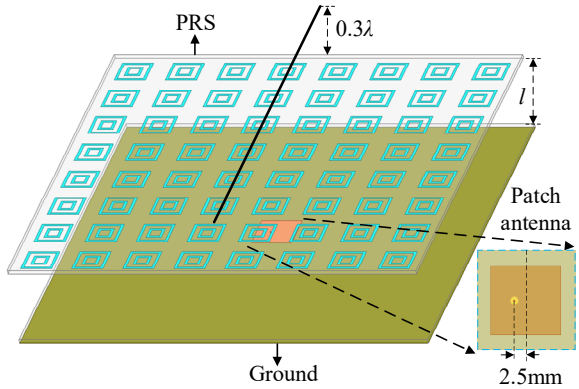

Figure 8: Structure of simulated PRS antenna.

3.2 Verification Using Full-Wave Simulations

To verify above phase distribution analysis of phase delay for different PRSs, two PRS antennas with capacitive and inductive unit cells were simulated using the Finite Element Method (FEM) method of ANSYS HFSS with radiation boundary. As depicted in Fig. 8, each PRS consists of 8×8 unit cells printed on the bottom surface of the PRS substrate. The parameters of the unit cells and the PRS heights are provided in Section 3.1. The dimensions of the PRS substrate are $0.16 \times 0.16 \times 0.0015$ m^3. The feeding source is a patch antenna placed on a fully perfect electric conductor (PEC) reflecting ground. The patch antenna has the dimensions of 0.0154×0.0154 m^2. The substrate of the patch antenna is F4BM-2 and it has the same thickness and material properties as the PRS substrate. The patch is fed from the bottom, with an offset of 2.5 mm from the patch center. The normalized phase and magnitude distribution results and gain results of these two PRS antennas are simulated and compared.

The normalized phase front distributions along a line 0.3λ at 5.5GHz above the two PRS antennas (the line is shown in Fig. 8) are shown in Fig. 9. The antenna with the capacitive PRS achieves a flatter phase front than the inductive one, which indicates that the capacitive PRS achieves less phase delay than the inductive one. The normalized magnitude distributions are shown in Fig. 10. The results show that the capacitive PRS achieves a more uniform magnitude distribution than the inductive one. Even though the capacitive and inductive unit cells have the reflection magnitude variation of 0.08 and -0.05, as well as the reflection phase variation of -8° and -4°, for the incident angle $|\alpha| < 45°$, these minor variations did not affect the conclusions obtained with the ray-tracing model, which assumes no reflection magnitude and angle variation with incident angle.

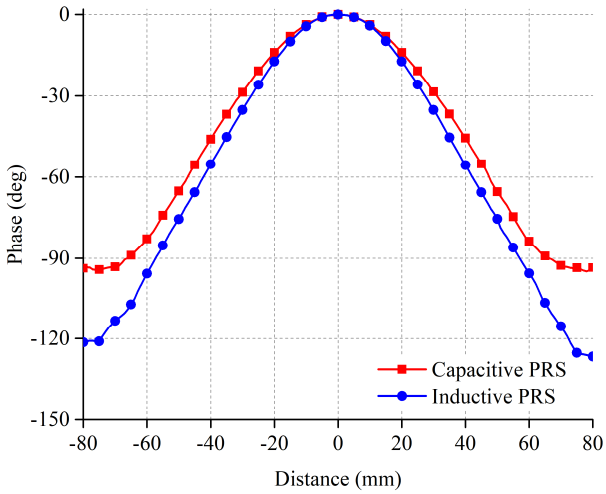

Figure 9: Normalized phase front distributions.

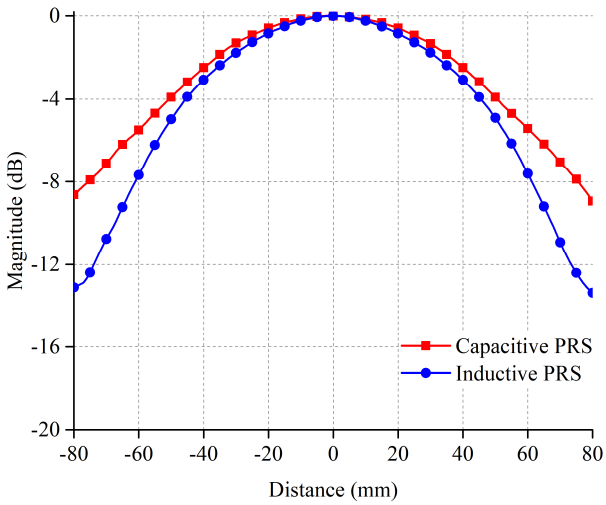

Figure 10: Normalized magnitude distributions.

The antenna gains of the two PRS antennas (assuming 100% total efficiency) are shown in Fig. 10. The antenna with the capacitive PRS has a gain of 16.6dBi, which is 1.8dBi higher than the antenna with the inductive PRS. The different phase and magnitude delay distributions of the two antennas affect their gains, as expected.

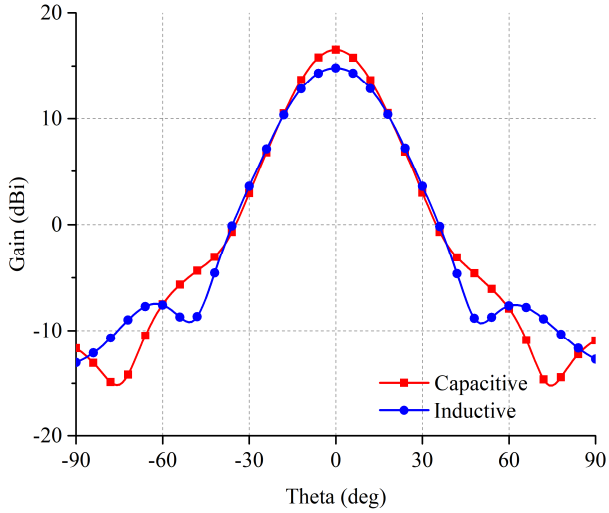

Figure 11: Gains of the capacitive and inductive PRS antennas.

4 Conclusion

In this paper, different gains of the capacitive and inductive PRS antennas are analyzed by using a ray-tracing model that accounts for oblique incident angles. The phase and magnitude distributions over the capacitive and inductive PRSs are compared with respect to their different heights. The derivations show that the capacitive PRS can achieve less phase delay and more uniform magnitude distribution over the surface, which result in higher antenna gain. These conclusions have been verified using full-wave simulations. Therefore, ray-tracing can be utilized to provide an intuitive explanation on the operating principle of PRSs.

5 Acknowledgment

This work is supported by Vetenskapsrådet under Grant no. 2018-04717.

References

[1] G. V. Trentini, “Partially reflecting sheet arrays,” *IEEE Trans. Antennas Propag.*, vol. 4, no. 4, pp. 666-671, Oct. 1956.

[2] A. S. Barlevy and Y. Rahmet-Samii, “Fundamental constraints on the electrical characteristics of frequency selective surfaces,” *Electromagn.*, vol. 17, no. 1, pp. 41-68, Oct. 2007.

[3] L. Zhou, X. Chen, Y. Cui, and X. Duan, “Comparative effects of capacitive and inductive superstrates on the RCA’s gain,” *IET Microw. Antennas Propag*., vol. 12, pp. 1834-1838, May 2018.

[4] A. Foroozesh, and L. Shafai, “Investigation into the effects of the reflection phase characteristics of highly-reflective superstrates on resonant cavity antennas,” *IEEE Trans. Antennas Propag.*, vol. 58, no. 10, pp. 3392-3396, Oct. 2010.

[5] A. Foroozesh and L. Shafai, “On the characteristics of the highly directive resonant cavity antenna having metal strip grating superstrate,” *IEEE Trans. Antennas Propag*., vol. 60, no. 1, pp. 78-91, Jan. 2012.

[6] M. D. Hougs, O. S. Kim, and O. Breinbjerg, “A ray-tracing method to analyzing modulated planar Fabry-Perot antennas,” in *Proc. 9th Europ. Conf. Antennas Propag.* (*EuCAP*), Lisbon, Portugal, Apr. 12-17, 2015, pp. 1-4.

[7] J. Wu, D. Zhou, X. Lei, J. Gao, and H. Hu, “A high gain Fabry-Perot cavity antenna designed by modified ray tracking model,” in *Proc. Int. Workshop Antenna Technol. (iWAT)*, Nanjing, China, Mar. 5-7, 2018, pp. 1-4.

[8] B. Ratni, W. A. Merzouk, A. de Lustrac, S. Villers, G. Piau, and S. N. Burokur, “Design of phase-modulated metasurfaces for beam steering in Fabry-Perot cavity antennas,” *IEEE Antennas Wireless Propag. Lett.*, vol. 16, pp. 1401-1404, Dec. 2017.

Paper II

Beam-Reconfigurable Antenna with Inductive Partially Reflective Surface and Parasitic Elements

A reconfigurable partially reflective surface (PRS) antenna can offer low-cost and low-complexity beam steering, traditionally implemented using a phased array with a bulky feeding network. This paper utilizes ray-tracing to prove analytically that an inductive nonuniform PRS facilitates larger beam deflection and lower sidelobe level (SLL) than a capacitive one, given the same reflection phase difference. With a suitable tradeoff in the beam deflection angle and gain variation between the reconfigurable states, an inductive reconfigurable PRS is designed for a ±13° steering range. To enhance the steering range with minimal complexity, two parasitic elements loaded with PIN diodes are added to the feeding source, resulting in the overall steering range of ±30°. The fabricated prototype verified that the pencil-shape beam can be steered towards 0º and ±30º with SLLs of less than -19dB at 5.5GHz. The antenna achieved peak realized gains of 9.5-10.4dBi for the three states with gain variation of less than 0.9dBi. The measured overlapped impedance band covers 5.41-5.63GHz for all states.

Qiuyan Liang, Buon Kiong Lau and Gaonan Zhou,
"Beam-Reconfigurable Antenna with Inductive Partially Reflective Surface and Parasitic Elements,"
IEEE Trans. Antenna Propag., 2023, Manuscript finished.

1 Introduction

Mobile communications have experienced rapid growth in the recent decade, driven by applications that benefit from the high data rates and improved coverage [1]-[3]. Since beam steering antennas can facilitate even higher data rates and larger coverage areas, they have become popular [4].

The conventional approach to realize beam steering is to use a phased array antenna. However, it requires a sophisticated transmission-line feeding network to achieve multiple phase distributions, which can cause considerable insertion loss and occupy a relatively large implementation space [5], [6]. Hence, pattern reconfigurable antenna is seen as a simpler and cheaper alternative to achieve beam steering, as its main beam can be steered electronically by loading the antenna with tunable semiconductor devices or mechanically by rotating the radiation structure [7]-[9].

Another type of pattern configuration antennas that has attracted more attention recently is based on partially reflective surface (PRS) antenna. PRS antennas can achieve medium-to-high gains by relying on multiple reflections of the wave between the PRS and a fully reflecting ground [10]-[12]. Conventionally, a PRS antenna uses a uniform PRS of uniform phase response to generate a broadside beam. By using a nonuniform phase-varying PRS, the radiated beam can be tilted from the broadside direction [13]-[15]. To enable beam steering, pattern reconfigurable PRS antennas have been proposed based on mechanical rotation [16], liquid materials [17], or electronic elements [18]-[26]. Compared with the former two implementations, the beam reconfiguration of the latter is realized electronically, facilitating fast beam steering.

PRSs consisting of reconfigurable unit cells with electronic elements have been proposed for beam steering. By varying the direct current (DC) biasing voltages, the phase distribution along the PRS, and hence the generated beam direction, can be controlled. A parallel-plate leaky wave-guide formed by a PRS and a varactor-loaded tunable high impedance surface (HIS) is used to steer the beam in one-dimensional (1-D) over 9°-30° [18] and ±25° [19], respectively. However, as the beam tilting angle increases, the thermal loss of the HIS increases, which decreases the total antenna efficiency (<60% for angles larger than 16° [18]). The 1-D beam steering PRS antennas designed with varactors or PIN diodes in [20] and [21] achieve the scanning ranges of ±7º and ±18º, respectively, and the sidelobe levels (SLLs) are around -7dB at the center frequency.

PRS antennas with 2-D beam steering have also been achieved by dividing the PRS into four independently controlled sectors [22]-[24]. In [22], based on a tunable HIS with varactors, the pencil beam can be steered within the scanning range of ±23º. However, the reduction in realized gain from the broadside to the tilted direction is more than 10dBi and -10dB impedance matching is not achieved for all states. Using PRSs with PIN diodes, the scanning range of ±10º and ±22º are achieved in [23] and

[24], respectively. However, when the deflection angle increases, the SLLs of the radiation patterns increase and the pencil-shape of the beams is not preserved [24]. In short, existing reconfigurable PRS antennas with different unit cell structures can offer different beam deflection angles, but they suffer from some common performance degradations, such as small beam deflection angles, high SLLs, severe gain variations between different reconfigurable states and non-pencil beam. Therefore, it is important to conduct a theoretical analysis on the working principle of PRS relating to beam steering, to obtain insights that can be used to improve the performance of PRS antennas.

In addition to reconfigurable PRSs, some research efforts have also been devoted to introducing reconfigurability at the feeding source for beam steering. Although an intuitive theoretical analysis has not been provided, it can be seen from practical examples that applying a phased array as the feeding source can enable beam deflection in the PRS antenna. In [25], ±10º beam steering is achieved by a PRS antenna fed by a phased array antenna with a reconfigurable feeding network composed of separate phase shifter network and matching network. On the other hand, the phase shifter network can be integrated into the matching network in a compact aperture-feed structure [26], resulting in a ±15º total beam steering range when combined with the ±5º steering range brought by the reconfigurable PRS. However, these feeding networks are still complicated and they lead to extra insertion losses. Therefore, it is desirable to understand how a reconfigurable feeding source can extend the beam steering range of a PRS and to propose a simple structure for such a feeding source.

In this context, this paper proposes a new beam steering antenna consisting of a reconfigurable inductive PRS and a feeding source with parasitic elements. The contributions are:

- A simple and intuitive ray-tracing model is utilized to analyze the working principle for beam deflection of PRS antenna with a nonuniform two-part PRS, based on which the beam deflection capability of different types of PRS is compared for the first time. It is concluded that an inductive nonuniform PRS yields larger beam deflection and lower SLL than a capacitive one, given the same reflection phase difference. This result was validated with full-wave simulation.
- Additional beam deflection for the PRS antenna has been provided by adding two parasitic elements to the feeding source, hence avoiding the use of multi-element antenna and lossy feeding network (i.e., phased array) to achieve the same result. The associated analysis confirms that the phase difference created by the reconfigurable feeding source adds constructively with that provided by the PRS.

- Compromising between large beam deflection and low gain variation among reconfigurable states, an inductive reconfigurable PRS antenna is designed to achieve ±13º beam steering, which is enhanced to ±30º by combining it with the beam steering capability of the feeding source.
- The proposed antenna achieves three pencil-shape beams pointing at 0º and ±30º with SLLs below -19dB at 5.5GHz. The peak realized gains are 9.5-10.4dBi for the three states with gain variation of less than 0.9dBi. The overlapped impedance bandwidth is 4% (5.41-5.63GHz) over all three states.

The rest of the paper is organized as follows: Section 2 provides a ray-tracing analysis of nonuniform PRS, which is then used to compare the beam deflection capability of inductive and capacitive PRSs. Section 3 presents the ray-tracing analysis of the reconfigurable PRS antenna fed with a beam deflected feeding source. Using the insights gained, a new reconfigurable PRS antenna is proposed in Section 4. Section 5 presents the measurement results of the fabricated prototype. Finally, Section 6 provides the conclusions.

2 Ray-Tracing Analysis of Nonuniform PRS

In the classical article that first proposed PRS antenna [10], its working principle and design parameters are all based on an intuitive ray-tracing model. In some subsequent designs of PRS antennas, the ray-tracing method has also been used to achieve faster optimization [27], higher gain [28], and arbitrary beam deflection angle [15]. In [15], ray-tracing is employed to derive the required phase distributions for a phase-modulated PRS to achieve a desired beam deflection angle. In the simplified model, only the four middle cells situated above the feeding source are considered for the phase derivation. The model was then used to design a fixed-beam prototype that achieves 30° deflection angle and -7dB SLL.

Although a phase-modulated PRS can be used to achieve beam steering by incorporating varactor diodes in the unit cells, such a design will require multiple voltage states to form different phase distributions across the PRS for different beam deflection angles, which increases the complexity of the DC biasing network. In addition, varactor diodes require relatively high actuated voltage [7], [29]. Therefore, many existing reconfigurable PRSs employ PIN diodes with simple DC biasing network, consisting only of two or four PRS parts to realize 1-D [21], [26] or 2-D [23], [24] beam steering. To realize symmetric 1-D deflected beams, the unit cells' structural parameters on the two sides of the PRS need to be identical, relying only on PIN diode switching to provide mirror symmetric nonuniform phase distributions across the two PRS parts (or uniform phase distribution with the same diode state [21]).

In the following, the principle underlying beam deflection using nonuniform two-part PRS is analyzed with a ray-tracing model. The analysis facilitates the comparison of different types of PRS in terms of beam deflection capability.

2.1 Working Principle of PRS Antenna

The ray-tracing model of a conventional PRS antenna is shown in Fig. 1(a). It consists of a feeding source, a uniform PRS and a perfectly reflecting ground. According to the classical working principle of PRS antenna, the waves from the feeding source are partially reflected multiple times between the PRS and the ground, which results in the multiple transmitted waves along the PRS functioning as new wave sources that radiate to the upper half space. The uniform PRS is placed at a specific distance l from the ground so that the multiple transmitted rays towards the left (L_0 to L_n) and the right (R_0 to R_n) are in-phase over the PRS, thus achieving a phase front parallel to the PRS and a broadside beam. The required distance l (or PRS height) can be calculated using the classical equation [10]

$$l = \left(\frac{\varphi_r}{360} - 0.5 \right) \frac{\lambda}{2} + N \frac{\lambda}{2} , \tag{1}$$

where λ is the wavelength in free space, φ_r is the reflection phase of the PRS, $N = 0$, 1, 2, … and $N = 1$ is normally chosen to minimize l (while being a physical solution). In the original ray-tracing analysis, (1) is derived by assuming normal wave incidence, as illustrated by the solid blue lines in Fig. 1(a). This was done to simplify the analysis of directivity in the broadside direction [10], at the expense of nonphysical wave propagation. The dashed blue (horizontal) line portions in Fig. 1(a) are added for continuity in the two left and right ray paths, but they are neither physical nor considered in the derivation. According to this assumption, the path length of the reflected ray between the PRS and ground is equal to the vertical distance l.

The phase shift of ray L_n (or ray R_n) φ_{rayLn} (or φ_{rayRn}) is the sum of the phases due to the ray path, the reflections on the PRS φ_r and the ground plane φ_g, as well as the transmission through the PRS φ_t, expressed as

$$\varphi_{rayLn} = \varphi_{rayRn} = -\frac{2\pi}{\lambda}(2n+1)l + n\varphi_r + n\varphi_g + \varphi_t , \tag{2}$$

where the index n (n = 0, 1, 2, …) represents that the wave has been reflected n times before it is transmitted through the PRS, and $\varphi_g = \pi$ [10]. With $N = 1$ chosen and PRS height l satisfying (1), it can be derived from (2) that the rays with adjacent index, such as rays L_{n+1} and L_n, have the phase difference of 0° and being in-phase, as depicted in Fig. 1(a).

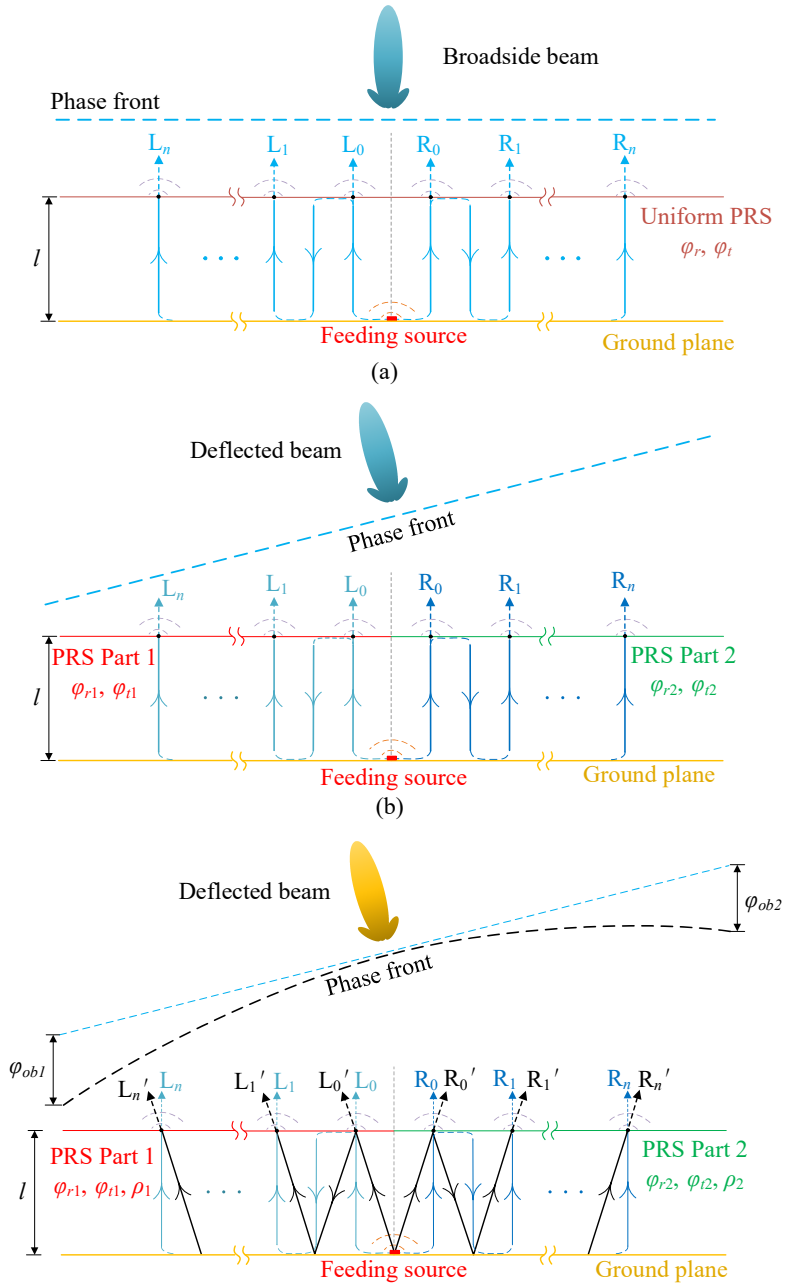

Figure 1: Ray-tracing models of PRS antennas for (a) uniform PRS with only normal incidence, (b) nonuniform two-parts PRS with only normal incidence, (c) nonuniform two-part PRS with oblique incidence.

Nonuniform PRSs with different phase-varying unit cells can be used to achieve phase front tilting. As shown in Fig. 1(b), the PRS is composed of two parts, with the reflection and transmission phases of φ_{r1}, φ_{t1} and φ_{r2}, φ_{t2}, respectively. The PRS height l is set using (1) from the average value of φ_{r1} and φ_{r2}. As a result, the rays with adjacent index on each PRS part have non-zero phase difference, and the in-phase condition in (1) is not satisfied for both parts. In this scenario, the phase front becomes tilted due to gradually increasing phase lag and phase lead to the left and right sides of the PRS, respectively. The resulted phase differences between the rays transmitted through the two PRS parts can be derived as follows.

From (2), the phase shifts φ_{rayLn} and φ_{rayRn} of rays L_n and R_n through PRS Part 1 and PRS Part 2 (at symmetric positions about the center) can be expressed as

$$\varphi_{rayLn} = -\frac{2\pi}{\lambda}\left(2n+1\right)l + n\varphi_{r1} + n\varphi_g + \varphi_{t1}, \tag{3}$$

$$\varphi_{rayRn} = -\frac{2\pi}{\lambda}\left(2n+1\right)l + n\varphi_{r2} + n\varphi_g + \varphi_{t2}. \tag{4}$$

From (3) and (4), with the same PRS height l and φ_g, the phase difference between the rays L_n and R_n is deduced as

$$\Delta\varphi = n\left(\varphi_{r1} - \varphi_{r2}\right) + \varphi_{t1} - \varphi_{t2}. \tag{5}$$

The phase difference $\Delta\varphi$ increases linearly with the number of reflections n. This explains why the two PRS parts have more phase difference near the edges than near the center, resulting in the smoothly tilting phase front across the PRS and a deflected beam, as depicted in Fig. 1(b).

However, in practice, the waves transmitted through the off-center positions of the PRS are from multiple oblique incident angles. Due to the longer ray paths, the oblique incidence causes additional phase delay along the PRS as compared to the simplified model considering only the normal incidence [30]. To distinguish from the blue lines of the simplified model, the solid black lines in Fig. 1 illustrate the two (left and right) ray paths of an oblique incident angle.

The cumulative phase delay due to all oblique incident angles compared to normal incidence is represented by φ_{ob}, which takes a negative value, representing an excess phase delay. It was derived that φ_{ob} is related to the reflection magnitude ρ of the PRS [31] – a larger ρ leads to a smaller phase delay. With different reflection magnitudes ρ_1 and ρ_2 of the two PRS parts, the phase shifts $\varphi_{rayLn'}$, $\varphi_{rayRn'}$ of rays L_n' and R_n', and their phase difference $\Delta\varphi'$ can be expressed as

$$\varphi_{rayLn'} = -\frac{2\pi}{\lambda}\left(2n+1\right)l + n\varphi_{r1} + n\varphi_g + \varphi_{t1} + \varphi_{ob1}, \tag{6}$$

$$\varphi_{rayRn'} = -\frac{2\pi}{\lambda}(2n+1)l + n\varphi_{r2} + n\varphi_g + \varphi_{t2} + \varphi_{ob2}, \tag{7}$$

$$\begin{aligned}\Delta\varphi' &= n(\varphi_{r1} - \varphi_{r2}) + \varphi_{t1} - \varphi_{t2} + \varphi_{ob1} - \varphi_{ob2} \\ &= n\Delta\varphi_r + \Delta\varphi_t + \Delta\varphi_{ob}\end{aligned}. \tag{8}$$

Therefore, the phase difference between rays L_n' and R_n' in the more practical model depicted in Fig. 1(c) is determined by the reflection phase difference $\Delta\varphi_r$, the transmission phase difference $\Delta\varphi_t$ and the phase delay difference $\Delta\varphi_{ob}$ due to different reflection magnitudes. The resulting phase front is illustrated as the black dashed line.

2.2 Effect of PRS Type on Beam Deflection

PRSs have been classified into two types according to the equivalent reactance of their periodic structures: capacitive PRS with reactance less than 0, and inductive PRS with reactance larger than 0 [32]. The two PRS types have different effects on PRS antenna properties, e.g., the capacitive PRS is more suitable for broadside beam, as it facilitates higher gain [30], [33]. However, the effect of PRS type on beam deflected PRS antenna has not been studied for existing reconfigurable PRS antennas. In this context, the previous ray-tracing analysis is utilized here to prove that the inductive PRS is more suitable for beam deflection.

In [34], a unit cell of a single-layer PRS is considered as a two-port system, and the reflection and transmission magnitudes and phases are analyzed regardless of the unit cell shape. The relationship between the reflection phase and the transmission phase was derived as [34]

$$\varphi_r - \varphi_t = \pm\frac{\pi}{2}, \tag{9}$$

where the positive and negative signs correspond to the inductive and capacitive PRSs, respectively, according to the theory of linear two-port networks [35]. The equation (9) also implies that when the same type of PRS unit cell is employed, designing beam deflection for PRS antennas with the simplified normal incidence PRS model shown in Fig. 1(b) only requires a certain reflection phase difference $\Delta\varphi_r$ to be achieved.

To investigate the difference between the capacitive and inductive PRSs more clearly, a typical PRS unit cell shown in Fig. 2 is simulated using the frequency domain finite element method (FEM) solver of ANSYS HFSS 2021 at 5.5GHz [12]. The unit cell is composed of an outer loop and an inner square patch, printed on the top and bottom sides of a dielectric substrate, respectively. The substrate for the PRS is F4BM-2 (dielectric constant $\varepsilon_r = 2.65$, loss tangent $\tan\delta = 0.001$) with the

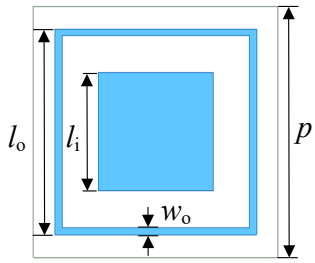

Figure 2: A classical unit cell structure (l_i = 8mm, w_o = 0.5mm, p = 17mm).

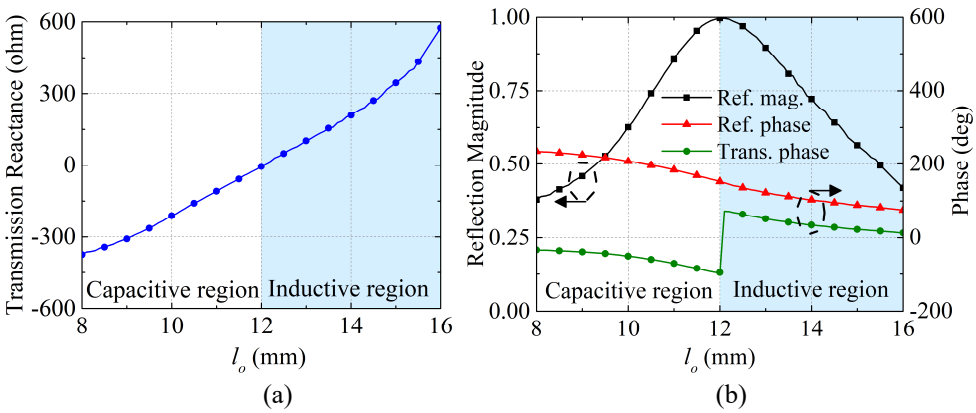

Figure 3: (a) The PRS type regions and (b) reflection and transmission properties of the unit cell with different variable l_o.

thickness of 1.5mm. The unit cell was simulated with different values of the structural parameter l_o, and the resulting equivalent transmission reactances (criteria of unit cell type), reflection magnitudes, as well as reflection and transmission phases are shown in Fig. 3.

As can be seen from the transmission reactance result in Fig. 3(a), the PRS unit cell is initially capacitive as l_o increases from 8mm, but later becomes inductive after a maximum reflection resonance point at l_o = 12mm. Moreover, it is observed in Fig. 3(b) that the reflection phase φ_r decreases monotonically as l_o increases. By choosing different l_{o1} and l_{o2} for PRS Parts 1 and 2, the two PRS parts can exhibit different reflection phases and form a non-zero reflection phase difference $\Delta\varphi_r$. The transmission phase φ_t has the same decreasing trend as the reflection phase φ_r in both the capacitive and inductive region, although φ_t is discontinuous between the two regions separated by a maximum reflection resonance point, which agrees with (9). Inserting (9) in (8), the phase difference between rays L_n' and R_n' becomes

$$\Delta\varphi' = (n+1)\Delta\varphi_r + \Delta\varphi_{ob}, \tag{10}$$

which shows that if $\Delta\varphi_r$ is fixed, then the total phase difference $\Delta\varphi'$ and the corresponding beam deflection (see the curved phase front in Fig. 1(c)) is only dependent on the phase delay difference $\Delta\varphi_{ob}$ due to different reflection magnitudes.

In addition, as l_o increases, the reflection magnitude ρ decreases in the inductive region, whereas it increases in the capacitive region (see Fig. 3(b)). For example, assuming that a nonuniform PRS is composed of inductive PRS Parts 1 and 2 with structural parameters of l_{o1} and l_{o2}, respectively. If $l_{o1} > l_{o2}$, then their reflection magnitudes become $\rho_1 < \rho_2$, which leads to $\varphi_{ob1} < \varphi_{ob2}$ and $\Delta\varphi_{ob} < 0$ [31]. The negative $\Delta\varphi_{ob}$ causes more phase difference, and providing that $\Delta\varphi_r$ is kept constant, the total phase difference $\Delta\varphi'$ will also increase and facilitate a larger beam deflection angle.

Following a similar argument, a capacitive nonuniform PRS with $l_{o1} > l_{o2}$ will lead to a positive $\Delta\varphi_{ob}$ and hence a smaller beam deflection angle than the inductive case. In essence, since the inductive and capacitive PRSs exhibit opposite trends in ρ as l_o increases, the resulting $\Delta\varphi_{ob}$ have opposite effects on the total phase difference. This leads to different extents of beam deflection, with the inductive PRS inherently leveraging large beam deflection.

2.3 Full-Wave Verification

To verify the above analysis of working principle and effect of PRS type on phase distribution, three PRS antennas using different types of PRSs but with the same reflection phase difference $\Delta\varphi_r$ (see Table 1) were simulated to achieve beam deflection at 5.5GHz. Based on (10), $\Delta\varphi_r$ is fixed to equalize the deflection angle for the simplified model in Fig. 1(b) and to highlight the contribution in actual beam deflection from $\Delta\varphi_{ob}$. As depicted in Fig. 4, the PRS consists of two PRS parts, each with 4 × 8 unit cells (unit cell dimensions given in Fig. 2), printed on a F4BM-2 substrate. The dimensions of the PRS substrate are $0.136 \times 0.136 \times 0.0015\text{m}^3$. The feeding source is a patch antenna printed on the top side of another F4BM-2 substrate with the same dimensions as the PRS substrate, with the bottom side being a perfect electric conductor (PEC) ground plane. The patch antenna and the ground plane are infinitely thin in the simulation models. In Case 1 and Case 2, the nonuniform two-part PRS utilizes inductive and capacitive unit cells, respectively. For the sake of completeness, Case 3 is a PRS that utilizes both types of unit cells. The parameters of the three PRS antennas are provided in Table 1. Following the PRS height setting in Section 2.1, l is taken to be the average value of φ_{r1} and φ_{r2}, calculated from (1) with $N = 1$.

The normalized phase and magnitude distributions of the electric field 0.3λ above along the center line of the three PRS antennas (i.e., the dash blue line in Fig. 4) are

Table 1: Parameters of three PRS antennas with different types of PRSs.

Three cases	PRS Part 1			PRS Part 2			
	l_{o1} (mm)	φ_{r1} (deg)	ρ_1	l_{o2} (mm)	φ_{r2} (deg)	ρ_2	l (mm)
Case 1	15.5	82	0.5	13.6	111	0.8	20.9
	Inductive			Inductive			
Case 2	10.8	191	0.8	9.3	220	0.5	29.2
	Capacitive			Capacitive			
Case 3	12.5	136	0.97	11.6	165	0.97	25.1
	Inductive			Capacitive			

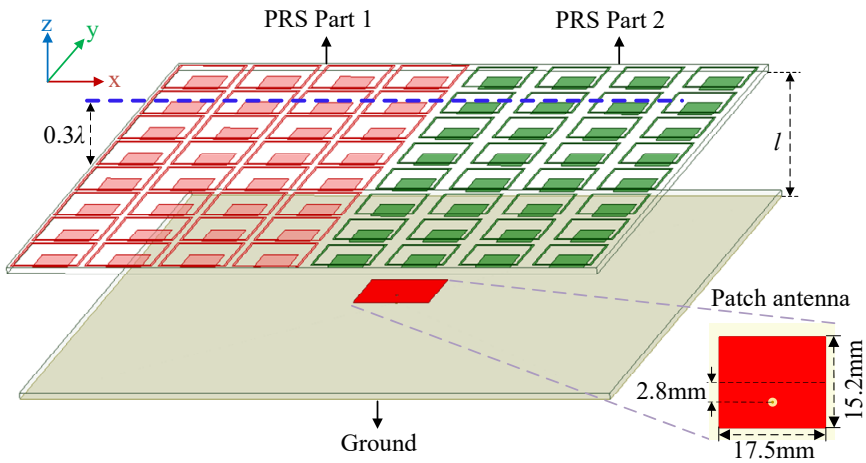

Figure 4: Structure of simulated PRS antenna fed with a patch antenna.

shown in Fig. 5. As can be seen from Fig. 5(a), the phase front for Part 1 is delayed more in Case 1 than in Case 2 due to a smaller ρ_1, whereas for Part 2 it is the opposite due to a larger ρ_2. Consequently, the inductive nonuniform PRS in Case 1 achieves more phase front tilting than the capacitive one in Case 2. The phase front in Case 3 has severe discontinuity because the PRS is composed of two types of unit cells with discontinuous transmission phases. Therefore, the phase distribution results from full-wave simulation agree with the predicted trends from ray-tracing.

Furthermore, as analyzed previously, the inductive PRS and capacitive PRS have opposite trends in reflection magnitude, given the same reflection phase variation (see Fig. 3), which leads to different results in terms of the superposition of the waves. Due to $\rho_1 < \rho_2$ in Case 1, the transmitted waves through Part 1 have larger amplitudes than the ones through Part 2, which facilitate stronger superposition of

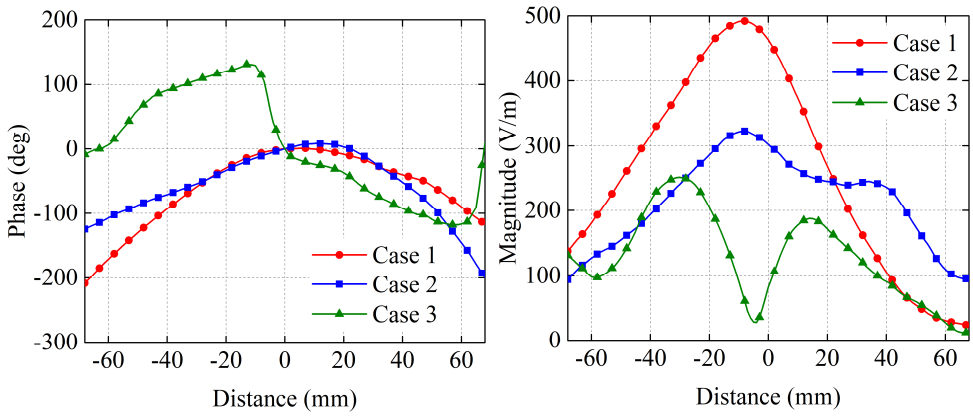

(a) (b)

Figure 5: (a) Normalized phase front distributions (line center as phase reference) and (b) magnitude distribution of PRS antennas with three different types of nonuniform PRS at 5.5GHz.

power in the phase front contributing to the main beam lobe (tilting towards the -x direction) than the side beam lobes (tilting towards the +x direction). In contrast, due to the smaller ρ_2 in Case 2, a considerably larger amount of the waves is transmitted through Part 2 than that of Case 1, leading to the strong superposition of power in the phase fronts contributing to the sidelobes, resulting in relatively high SLLs. In Case 3, due to the high reflection magnitudes, the transmitted waves through the PRS are of lower magnitudes. Based on these different effects of wave superposition, the magnitude distributions for the three cases are formed (see Fig. 5(b)).

The observed magnitude and phase distributions contribute to the simulated radiation patterns of the three antennas shown in Fig. 6. The PRS antennas in Case 1 and Case 2 achieve -14° and -5° deflection angles with SLL of -22dB and -9.8dB, respectively. The antenna gain in Case 1 is 1.7dBi lower than that in Case 2, which is due to the lower PRS height l [30]. In Case 3, the antenna achieves -34° deflection angle due to the large transmission phase difference, but at the cost of the high SLL of -3.3dB.

Therefore, based on the full-wave simulation results, the deflected beam can be formed by giving non-zero reflection phase difference, and the type of PRS has an impact on the effect of beam deflection, which agrees with the ray-tracing analysis. It can be concluded that the inductive nonuniform PRS can achieve more phase front tilting and more tapering in the magnitude distribution, which facilitate larger beam deflection and lower SLL than the capacitive one, given the same reflection phase difference.

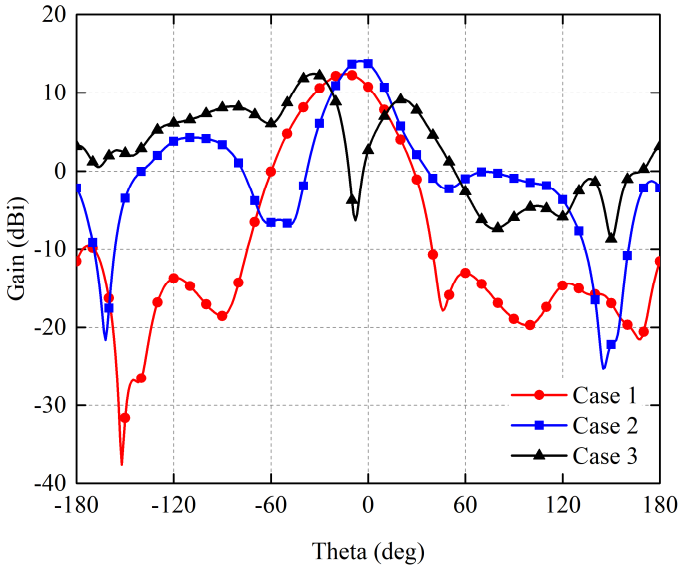

Figure 6: Simulated radiation patterns of PRS antennas with three different types of nonuniform PRS at 5.5GHz.

3 Beam-Reconfigurable PRS and Feeding Source

3.1 Design Tradeoff in Beam-Reconfigurable PRS

In the previous section, the working principle of PRS antenna was analyzed with respect to beam deflection and then applied to show that inductive PRS is preferred for deflecting a fixed beam. However, steerable beam is required in many applications, e.g., mobile communications [5], [12].

To design a beam-reconfigurable PRS, the unit cells in the previous two-part PRS can be loaded with PIN diodes. The reflection phase difference of the unit cells between the ON and OFF states in the two parts enables phase front tilting and hence deflected beam. By setting all the PIN diodes in the same state (ON-ON/OFF-OFF), uniform unit cell distribution and hence broadside beam is realized. However, since the PRS height is determined by the average value of the phases in ON and OFF states, the height will cause phase lagging or leading of the transmitted rays when ON or OFF state is selected for a uniform PRS, as analyzed in Section 2.1. As a result, the in-phase condition of (1) is no longer satisfied, thus affecting the antenna gain and radiation pattern performance of the broadside beam [21]. The degree of performance degradation to the broadside beam state was evaluated as follows.

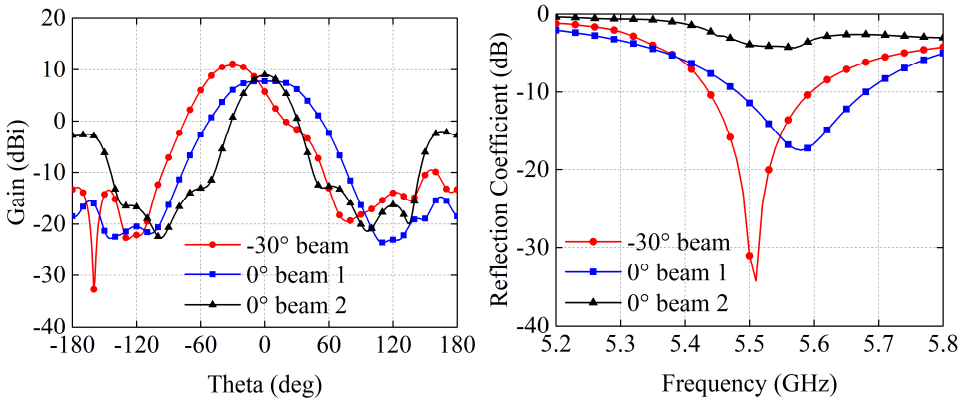

(a) (b)

Figure 7: (a) Simulated broadside (θ = 0°) and deflected (θ = 30°) radiation patterns at 5.5GHz. (b) Simulated reflection coefficients.

Table 2: Parameters of the modelled reconfigurable PRS antennas in three states.

Beams	PRS Part 1			PRS Part 2		
	l_{o1} (mm)	φ_{r1} (°)	ρ_1	l_{o2} (mm)	φ_{r2} (°)	ρ_2
-30° beam	16.7	62	0.3	12.8	128	0.93
0° beam 1	16.7	62	0.3	16.7	62	0.3
0° beam 2	12.8	128	0.93	12.8	128	0.93

As an illustration, a nonreconfigurable (beam deflecting) two-part inductive PRS can be formed by two different unit cells with l_o of 16.7mm and 12.8mm, giving reflection phases of 62° and 128°, respectively (see Table 2). The two different unit cells are used to model the ON and OFF states of a reconfigurable unit cell. As listed in Table 2, three PRSs composed of the two different unit cells are used to model three states of a reconfigurable PRS (actual PIN diode loaded unit cell will be designed in the next section). The fixed-beam PRS antennas using the three PRSs fed by a patch antenna (see Fig. 4) were simulated. The PRS height was set to l = 20.9mm, determined by the average reflection phase of 95°. As can be seen in Fig. 7(a), -30° deflected beam and two 0° broadside beams are achieved, and the reflection coefficients are shown in Fig. 7(b). The gain of the 0° beam 1 is 3.4dBi lower than that of the -30° beam, whereas 0° beam 2 has a narrower beamwidth and slightly higher gain than 0° beam 1, but the back lobe of the 0° beam 2 is as high as -11.2dB.

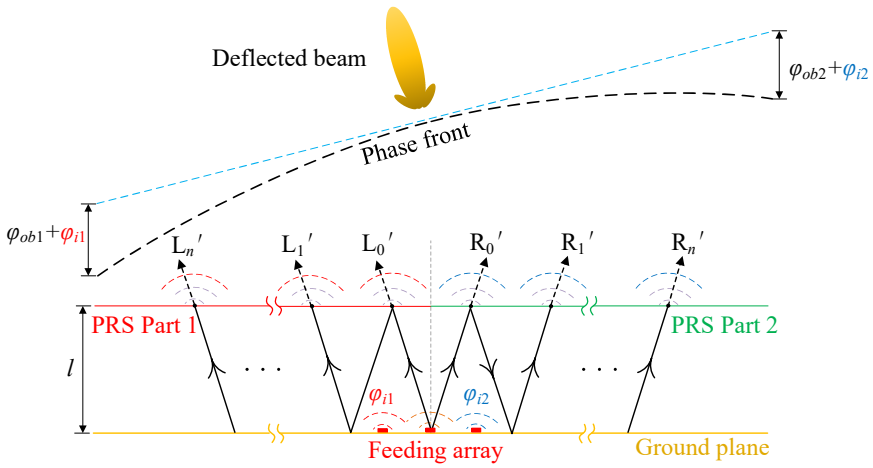

Figure 8: Working principle of PRS antenna composed of a nonuniform PRS and phase distributed feeding source based on a ray-tracing model.

Therefore, a tradeoff is needed between the broadside beam pattern properties and the size of the deflection angle, with a larger angle requiring a larger reflection phase difference for the reconfigurable PRS design. It is also observed in Fig. 7(b) that the PRS corresponding to 0° beam 2 incurs a larger impedance mismatch than the other two PRSs. This is due to the much higher ρ (0.93) causing more waves to be reflected from the PRS to the feeding source.

3.2 Ray-Tracing Analysis of PRS Antenna with Beam Deflected Feeding Source

Given the aforesaid design tradeoff in obtaining desired properties for both broadside and deflected beams (see Fig. 7(a)), a beam deflected feeding source can be used instead to deflect the beam further while retaining good broadside beam. As mentioned in Section 1, phased array has been used as such a feeding source [25]-[26]. However, the role of a phased array in extending the beam deflection in a PRS antenna has not been explained analytically.

Using the ray-tracing analysis of the nonuniform two-part PRS in Section 2, the working principle of the PRS antenna fed with a phased array can be explained intuitively as follows. As illustrated in Fig. 8, the array elements in the array have different initial phases φ_{i1} and φ_{i2}. Since each array element contributes more to the incident rays in the PRS part just above it, the phase difference between rays L_n' and R_n' is

$$\Delta\varphi' = (n+1)\Delta\varphi_r + \Delta\varphi_{ob} + \Delta\varphi_i, \tag{11}$$

where the $\Delta\varphi_i = \varphi_{i1} - \varphi_{i2}$ is the initial phase difference from the feeding source. Therefore, the phase distributed feeding source can further increase the phase difference across the PRS, thus further increasing the beam deflection angle induced by the PRS. In other words, (11) shows that the beam deflection capability of the feeding source adds constructively to the beam deflection effect of the PRS.

4 Reconfigurable PRS Antenna Design

The ray-tracing analyses in Sections 2 and 3 give more clarity to the working principle of beam deflected PRS antenna, which provides useful guidelines for PRS antenna design: 1) Given the specific reflection phase difference, the inductive PRS is preferred to achieve larger beam deflection angle with lower SLL; 2) The beam deflected feeding source can further enhance the deflection angle. Based on these guidelines, a novel PRS antenna with reconfigurability in both the inductive PRS and the feeding source is designed below.

4.1 Reconfigurable PRS Design

As shown in Fig. 9, the inductive PRS is composed of three parts, where Parts 1 and 2 are on the two sides with 3×8 reconfigurable unit cells and Part 3 in the middle with 2×8 nonreconfigurable unit cells. Part 3 provides a reflection phase between those of the other two parts (in opposite diode states) to reduce the number of PIN diodes needed. The nonreconfigurable unit cells in Part 3 utilizes the structure in Fig. 2 but with updated parameters to achieve the required reflection phase. The reconfigurable unit cells in Part 1 and Part 2 have identical structural parameters and were modified from the nonreconfigurable one by dividing the inner square patch in the bottom surface into two halves with a 0.8mm slot and inserting two PIN diodes (see Fig. 9). The equivalent circuits of the PIN diode (SMP1340-079LF [36]) for the ON and OFF states, as shown in Fig. 10, were used in the simulation model of the PRS antenna, where the insertion loss of the PIN diode in the ON and OFF states were modelled with 0.85Ω and 3kΩ resistors, respectively [34].

The substrate for the PRS antenna and feeding source is F4BM-2 and the dimensions are $0.16 \times 0.16 \times 0.0015\text{m}^3$. The surface area of the substrate is slightly larger than that of the simulated example in Section 2.3 to fit the DC biasing circuit for the PIN diodes as well as the nylon spacers for supporting the PRS substrate above the ground plane. The final structural parameters of the PRS unit cells were obtained by finding a suitable tradeoff between reflection coefficients and beam-pattern properties over all reconfigurable states. The DC biasing lines of 0.3mm width for

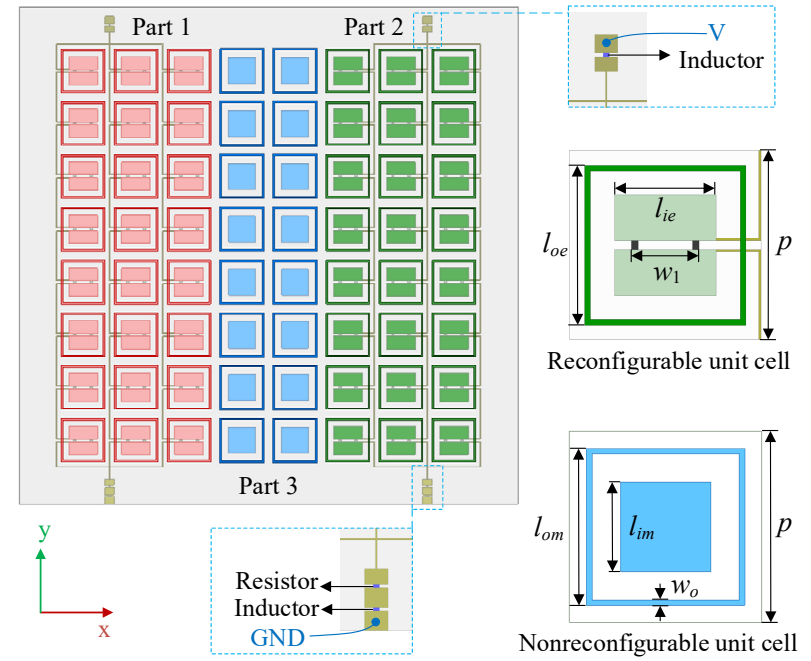

(a)

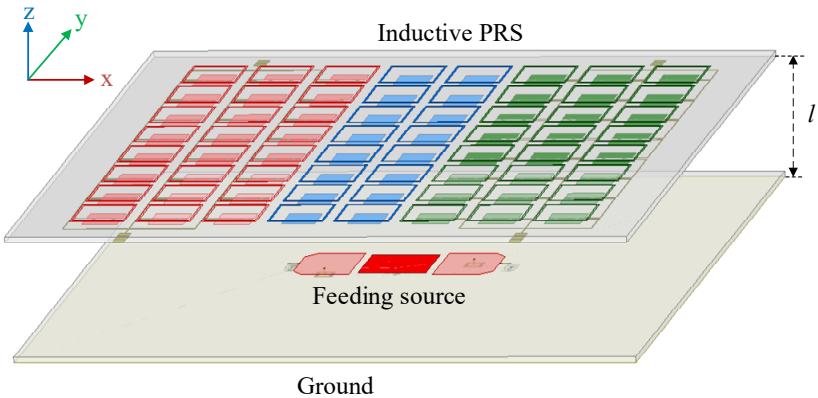

(b)

Figure 9: (a) PRS structure (l_{oe} = 14mm, l_{ie} = 9.2mm, l_{om} = 14.3mm, l_{im} = 8.5mm, w_1 = 6mm, w_o = 0.5mm, p = 17mm). (b) 3D view of the PRS antenna (l = 20mm).

Parts 1 and 2 were printed in the bottom surface of the PRS and connected to the two halves of the inner patches to control the states of the PIN diodes. Two RF choke inductors of 56nH and a current protection resistor are used in the biasing network of each part.

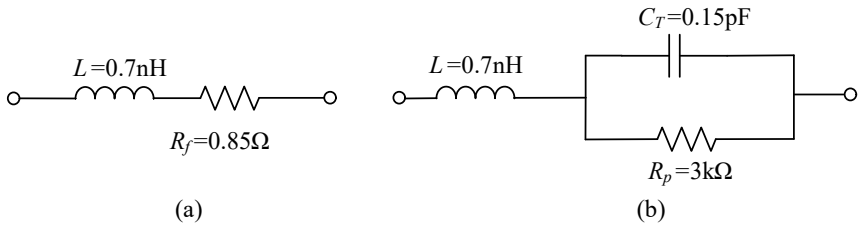

Figure 10: Equivalent circuits of PIN diode in (a) ON state and (b) OFF state.

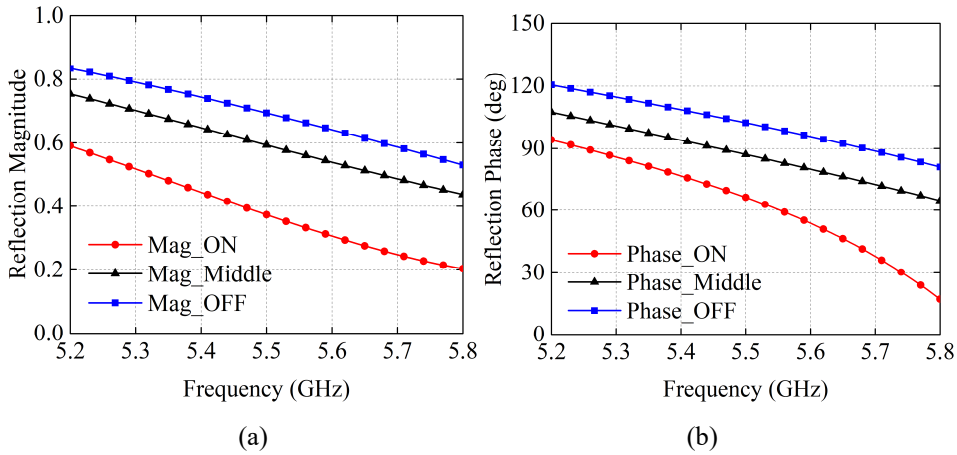

Figure 11: (a) Reflection magnitudes and (b) phases of the unit cells.

The reflection phases and magnitudes of the unit cells are shown in Fig. 11. The reflection magnitudes and phases of the reconfigurable unit cell in the ON and OFF states at 5.5GHz are $\rho_1 = 0.37$, $\varphi_{r1} = 66°$ and $\rho_2 = 0.69$, $\varphi_{r2} = 102°$, respectively. As explained previously, the PRS height l was calculated using (1) from the average value of φ_{r1} and φ_{r2}. When the PIN diodes are switched ON, the two halves of the inner patches of the reconfigurable unit cells are connected to each other, which results in a larger equivalent inner patch size than in the OFF state, leading to a lagging reflection phase and a smaller reflection magnitude. Accordingly, the nonreconfigurable unit cell was designed to provide the reflection magnitude and phase of $\rho_3 = 0.59$ and $\varphi_{r3} = 87°$, respectively.

4.2 Feeding Source Design

The feeding source is composed of an active element and two passive elements located on two sides [37]. The active element is fed with a SMA connectors. Each passive element is connected to a metal sheet on the ground plane through a shorting

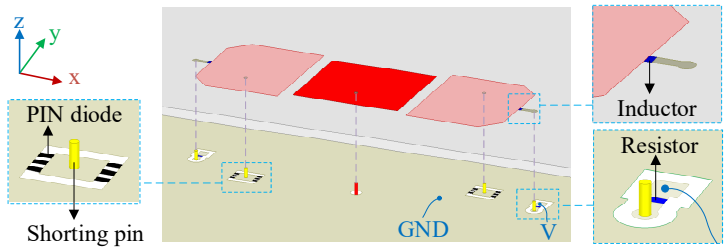

(a)

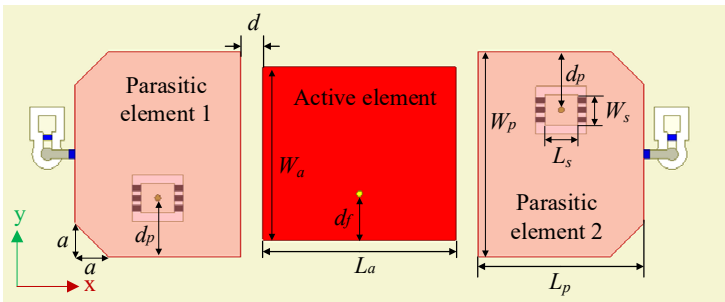

(b)

Figure 12: Geometry of the phase distributed feeding source. (a) 3D exploded view. (b) Top view (a = 3mm, d = 2mm, d_f = 4.3mm, d_p = 5.3mm, L_a = 17.5mm, W_a = 15.8mm, L_p = 15mm, W_p = 18.6mm, L_s = 3mm, W_s = 2.7mm).

pin. The metal sheet is loaded with six PIN diodes bonded over a square slot etched on the ground. The shorting pins of two parasitic elements are installed in rotationally symmetric positions to eliminate the asymmetry of the radiation pattern with respect to the *x*-axis due to the off-center installation. The six PIN diodes are installed with bias direction from the metal sheet to the ground. A RF choke inductor of 56nH and a current protection resistor are used in the biasing network of each parasitic element. Since the PIN diodes has different equivalent circuits in the ON and OFF states, which affects the electrical size of the parasitic element, the parasitic element acts as reflector/director when the diodes are in ON/OFF states and the beam can be steered to the director based on the principle of Yagi-Uda antenna [37]. The broadside beam is obtained in the OFF/OFF states. Moreover, the switched beam parasitic antenna can be seen as a simplified phased array, since the parasitic elements provide phase-shifted radiation via capacitive coupling to the active element. As mentioned in the introduction, this choice avoids the need for a feeding network and the associated losses.

Figure 13 shows the simulated radiation patterns at 5.5GHz and the reflection coefficients of the feeding source in the three states. In States A and B, the feeding

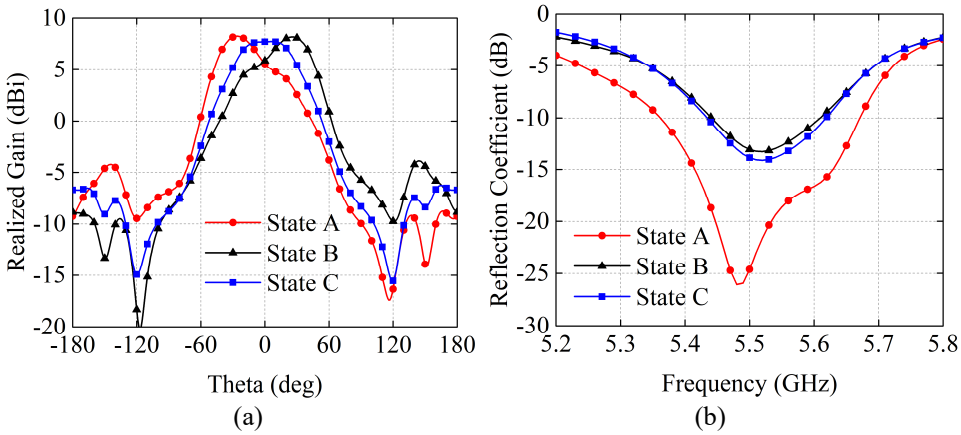

Figure 13: Simulated (a) radiation patterns at 5.5GHz and (b) reflection coefficients of the feeding source in three states (State A: parasitic 1 and 2 in OFF and ON states, State B: parasitic 1 and 2 in ON and OFF states, State C: parasitic 1 and 2 in OFF and OFF states).

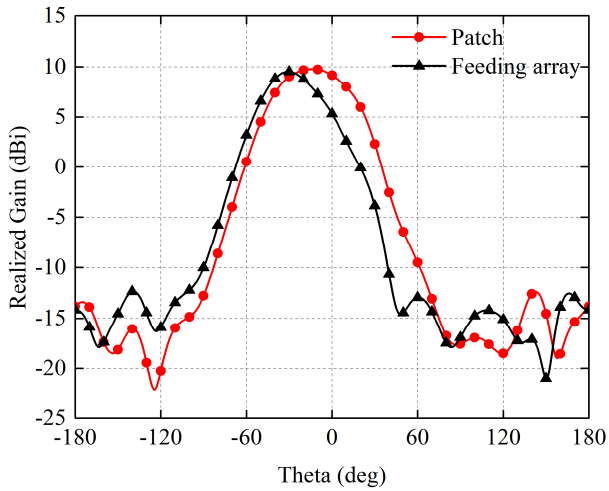

Figure 14: Simulated radiation patterns of the PRS antenna fed with different sources at 5.5GHz.

source achieves the deflection angle of θ = -26° and θ = 26°, respectively. From the simulation, it was observed that the beam deflection angle and SLL of the feeding source increase with the operating frequency. Therefore, trading between the beam deflection angle and the SLL of the PRS antenna in the band 5.4-5.6GHz, the deflection angle of 26° was chosen for the final feeding source. In State C, the

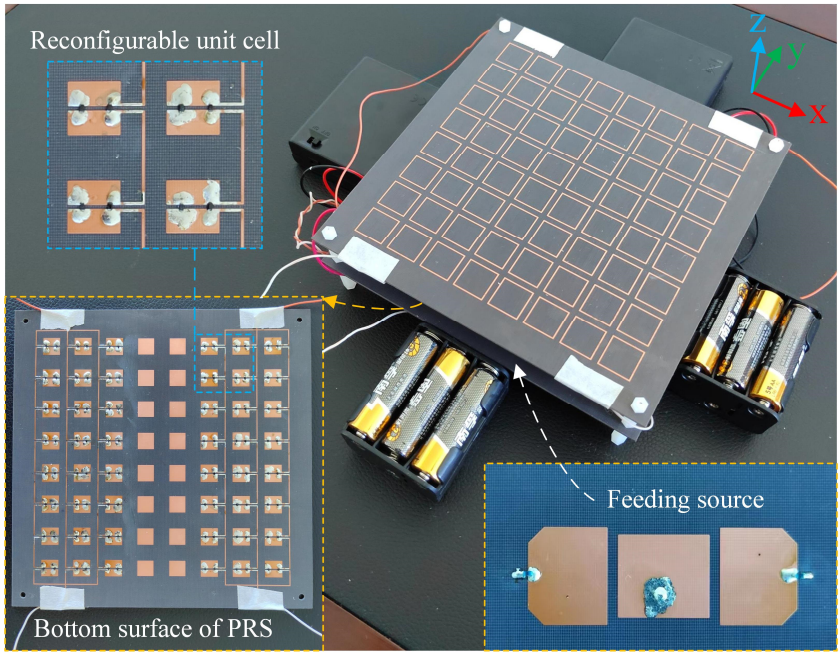

Figure 15: Prototypes of the proposed PRS antenna.

broadside beam is achieved with both parasitic elements in the OFF state. It can be seen in Fig. 13(b) that the feeding source in State C has a wider impedance bandwidth than those of the other two states. This is because the parasitic element in the OFF state has a smaller effective electrical size, which introduces a second resonance at a slightly higher frequency. Since State C has two parasitic elements in the OFF state, the bandwidth is wider than the other two cases with only one parasitic element in the OFF state. The bandwidth broadening effect due to the parasitic elements also benefits the impedance matching of the PRS antenna, as will be presented in Section 5. The reflection coefficients in States A and B are slightly different, because the biasing states of the two sets of diodes are not completely symmetric with respect to the active element in the two states.

With the PRS Parts 1 and 2 in the ON and OFF states, respectively, the PRS antennas fed with a patch antenna (see the schematic in Fig. 4) and the beam deflected feeding source (see Fig. 12) were simulated to validate the effect of the parasitic-loaded feeding source on the beam deflection. Figure 14 shows that the beam deflection angle achieved by the PRS with the simple patch antenna is -13°, and this is increased to -30° by using the beam deflected feeding source, consistent to the analysis in Section 3.2.

Table 3: Reconfigurable states of the PRS antenna.

States	PRS part 1	PRS part 2	Parasitic element 1	Parasitic element 2	Beam angles
State 0	OFF	OFF	OFF	OFF	0°
State 1	ON	OFF	OFF	ON	-30°
State 2	OFF	ON	ON	OFF	30°

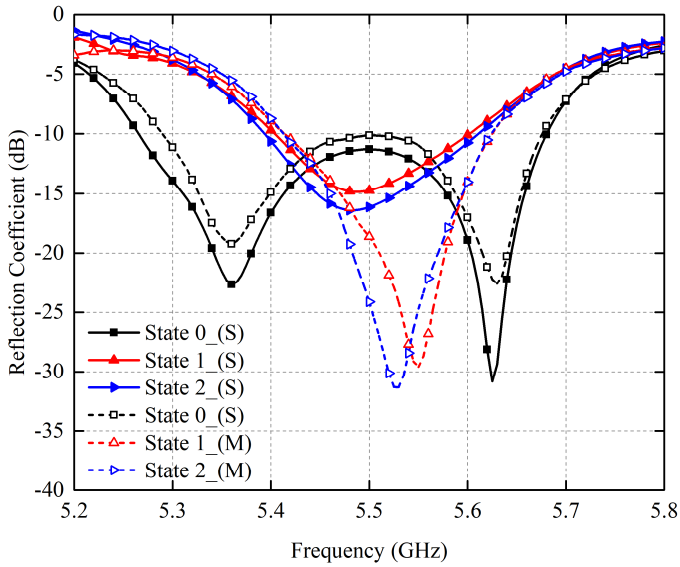

Figure 16: Simulated and measured reflection coefficients of the PRS antenna.

5 Simulated and Measured Results

A prototype of the proposed reconfigurable PRS antenna was fabricated (see Fig. 15). Nylon spacers are used to support the PRS substrate above the ground plane. The DC biasing voltages for the two PRS parts and two parasitic elements are supplied with four sets of batteries, which are placed at the back of the ground plane in the measurement. The three reconfigurable states of the PRS antenna are list in Table 3.

The simulated and measured reflection coefficients of the PRS antenna in the three states are shown in Fig. 16. As explained, State 0, corresponding to the broadside beam, has a wider measured impedance bandwidth (5.29-5.68GHz) than the other two states due to both parasitic elements being in the OFF state. The measured overlapped impedance bandwidth of 5.41-5.63GHz is achieved for all states. The

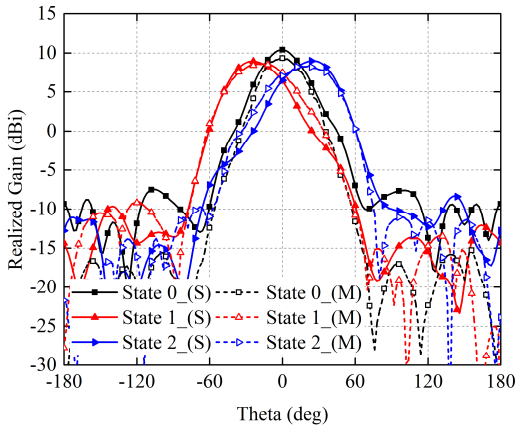

(a)

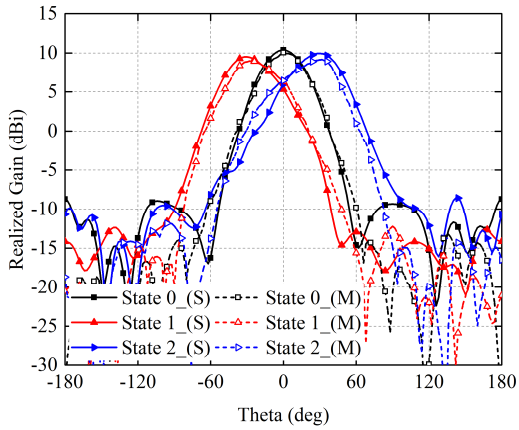

(b)

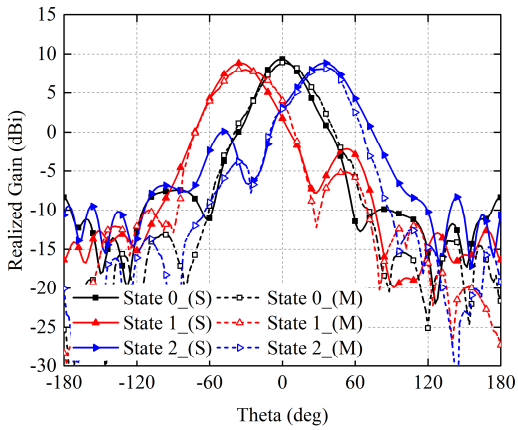

(c)

Figure 17: Simulated and measured radiation patterns of the PRS antenna. (a) 5.4GHz. (b) 5.5GHz. (c) 5.6GHz.

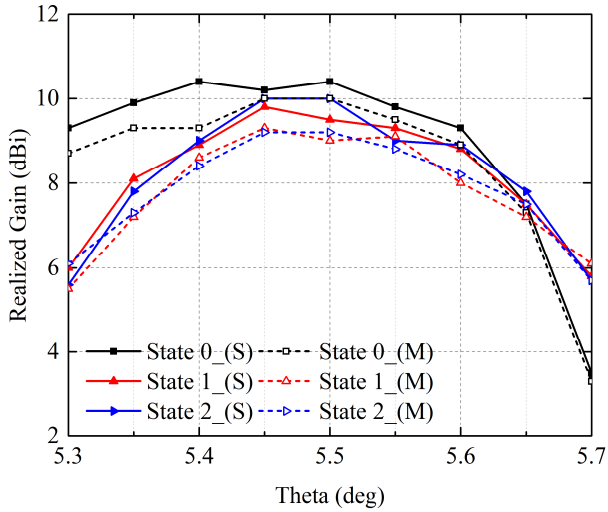

Figure 18: Simulated and measured realized gains of the PRS antenna.

Table 4: Comparison between the proposed and previous reconfigurable PRS antennas.

	Maximum Deflection Angle	SLL (dB)	Realized Gain (dBi)	Volume/λ^3	Overlapped Impedance Bandwidth
[21]	18°	-6	10.7-11.7	2.75×2.75×0.59	3.6%
[23]	10°	-10	8.7-9.7	1.8×1.8×0.51	3.6%
[24]	22°	-5	9.6-10.4	2.75×2.75×0.45	4%
[26]	15°	-8	12-15.5	3.1×3.1×0.55	4.4%
This work	30°	-19	9.5-10.4	2.9×2.9×0.37	4%

discrepancies between the simulated and measured results are primarily due to the tolerance in the soldering of the SMA connectors.

The radiation patterns in *x-z* plane of the PRS antenna at 5.4, 5.5 and 5.6GHz are shown in Fig. 17. The simulated and measured radiation patterns are seen to be in good agreement with each other. At 5.4, 5.5 and 5.6GHz, the beam deflection angles are ±25º, ±30º and ±35º, respectively. The increase of deflection angle with operating frequency is mainly because of that the deflection angle of the feeding source increases with the frequency, as mentioned in Section 4.2. At the center frequency of 5.5GHz, the PRS antenna can radiate three pencil-shape beams towards 0º and ±30º with SLLs of less than -19dB. The simulated and measured peak realized gains of the PRS antenna in the three states are shown in Fig. 18. At 5.5GHz, the predicted simulation peak realized gains of the PRS antenna in States

0, 1 and 2 are 10.4, 9.5 and 10dBi, respectively. The minor differences (< 1dB) between the simulated and measured results are mainly attributed to the tolerance of the measurement system and slight pattern shape discrepancy, the latter of which was caused by inaccuracies in the PIN diode's equivalent circuits. The simulated gain variation between the broadside and the deflected beams at 5.4, 5.5 and 5.6GHz are less than 1.4, 0.9, and 0.7dBi, respectively.

A comparison of recent reconfigurable PRS antennas using PIN diodes based on the maximum beam deflection angle, SLL, realized gain, and volume is presented in Table 4. The proposed PRS antenna achieves larger beam deflection angle and lower SLL than other antennas, which is due to the use of inductive PRS in combination with the beam-reconfigurable feeding source. The inductive PRS of the proposed antenna leads to a lower antenna profile with moderate gains [30], and the gain variation from the broadside beam to the deflected beam is relatively small. Compared with the phased array feeding source in [26], the proposed feeding source with parasitic elements offers a simpler structure to achieve the 4% overlapped impedance bandwidth, without extra matching network and phase shifters, which reduces the insertion loss and further enhances the beam steering range.

6 Conclusion

A reconfigurable PRS antenna with inductive PRS and parasitic elements in the feeding source is proposed in this work for beam steering. First, the working principle of beam deflected PRS antenna is analyzed using ray-tracing. It is concluded that the inductive PRS facilitates larger beam deflection angle and lower SLL than the capacitive one, given the same reflection phase difference. Based on the ray-tracing analysis, it is shown that the beam deflected feeding source can further enhance the beam deflection angle of the reconfigurable PRS antenna limited by the gain variation between the different unit-cell states in the two-part PRS. A prototype is then designed and fabricated for the center frequency of 5.5GHz using these insights. The measured results show that the PRS antenna provides three pencil-shape beams towards 0° and ±30º with SLLs and gain variation lower than -19dB and 0.9dBi, respectively, at 5.5GHz. The measured overlapped impedance bandwidth is 5.41-5.63GHz for all states.

References

[1] A. Gupta and R. K. Jha, "A survey of 5G network: architecture and emerging technologies," *IEEE Access*, vol. 3, pp. 1206-1232, 2015.

[2] J. Navarro Ortiz, P. Romero Diaz, S. Sendra, and P. Ameigeiras, J. J. Ramos-Munoz, and J. M. Lopez-Soler, "A survey on 5G usage scenarios and traffic models," *IEEE Commun. Surv. Tut.*, vol. 22, no. 2, pp. 905-929, 2020.

[3] M. Z. Chowdhury, M. Shahjalal, S. Ahmed, and Y. M. Jang, "6G wireless communication systems: applications, requirements, technolo-gies, challenges, and research directions," *IEEE Open J. Commun. Society*, vol. 1, pp. 957-975, 2020.

[4] W. Hong, *et al*., "Multibeam antenna technologies for 5G wireless communications," *IEEE Trans. Antennas Propag*., vol. 65, no. 12, pp. 6231-6249, 2017.

[5] K. Tekkouk, M. Ettorre, L. Le Coq, and R. Sauleau, "Multibeam SIW slotted waveguide antenna system fed by a compact dual-layer Rotman lens," *IEEE Trans. Antennas Propag*., vol. 64, no. 2, pp. 504-514, Feb. 2016.

[6] C. C. Chang, R. Lee, and T. Shih, "Design of a beam switching/steering butler matrix for phased array system," *IEEE Trans. Antennas Propag*., vol. 58, no. 2, pp. 367-374, Feb. 2010.

[7] C. G. Christodoulou, Y. Tawk, S. A. Lane, and S. R. Erwin, "Reconfigurable antennas for wireless and space applications," *Proc. IEEE*, vol. 100, no. 7, pp. 2250-2261, July 2012.

[8] W. Li, *et al*., "Programmable coding metasurface reflector for reconfigurable multibeam antenna application," *IEEE Trans. Antennas Propag*., vol. 69, no. 1, pp. 296-301, Jan. 2021.

[9] S. V. Hum and J. Perruisseau-Carrier, "Reconfigurable reflectarrays and array lenses for dynamic antenna beam control: a review," *IEEE Trans. Antennas Propag*., vol. 62, no. 1, pp. 183-198, Jan. 2014.

[10] G. V. Trentini, "Partially reflecting sheet arrays," *IEEE Trans. Antennas Propag*., vol. 4, no. 4, pp. 666-671, Oct. 1956.

[11] L. Zhou, X. Chen, and X. Duan, "Fabry-Pérot resonator antenna with high aperture efficiency using a double-layer nonuniform superstrate," *IEEE Trans. Antennas Propag*, vol. 66, no. 4, pp. 2061-2066, Apr. 2018.

[12] A. Goudarzi, M. M. Honari, and R. Mirzavand, "Resonant cavity antennas for 5G communication systems: a review," *Electron*., vol. 9, no. 7, pp. 1080, July 2020.

[13] A. Ourir, S. N. Burokur, and A. de Lustrac, "Phase-varying metamaterial for compact steerable directive antennas," *Electron. Lett*., vol. 43, no. 9, pp. 493-494, Apr. 2007.

[14] H. Nakano, S. Mitsui, and J. Yamauchi, "Tilted-beam high gain antenna system composed of a patch antenna and periodically arrayed loops," *IEEE Trans. Antennas Propag*., vol. 62, no. 6, pp. 2917-2925, Jun. 2014.

[15] B. Ratni, W. A. Merzouk, A. de Lustrac, S. Villers, G. P. Piau, and S. N. Burokur, "Design of phase-modulated metasurfaces for beam steering in Fabry-Pérot cavity antennas," *IEEE Antennas Wireless Propag*. Lett., vol. 16, pp. 1401-1404, 2017.

[16] M. U. Afzal, and K. P. Esselle, "Steering the beam of medium-to-high gain antennas using near-field phase transformation," *IEEE Trans. Antennas. Propag*., vol. 65, no. 4, pp. 1680-1690, Apr. 2017.

[17] X. Yang, Y. Liu, H. Lei, Y. Jia, P. Zhu, and Z. Zhou, "A radiation pattern reconfigurable Fabry-Pérot antenna based on liquid metal," *IEEE Trans. Antennas Propag*., vol. 68, no. 11, pp. 7658-7663, Nov. 2020.

[18] R. Guzman-Quiros, J. L. Gomez-Tornero, A. R. Weily, and Y. J. Guo, "Electronically steerable 1-D Fabry-Pérot leaky-wave antenna employing a tunable high impedance surface," *IEEE Trans. Antennas Propag*., vol. 60, no. 11, pp. 5046-5055, Nov. 2012.

[19] R. Guzman Quiros, J. L. Gomez Tornero, A. R. Weily, and Y. J. Guo, "Electronic full-space scanning with 1-D Fabry-Pérot LWA using electromagnetic band-gap," *IEEE Antennas Wireless Propag. Lett*., vol. 11, pp. 1426-1429, Nov. 2012.

[20] A. Ourir, S. N. Burokur, and A. de Lustrac, "Electronic beam steering of an active metamaterial-based directive subwavelength cavity," in *Proc. 2nd Eur. Conf. Antennas Propag. (EuCAP)*, Edinburgh, U.K., Nov. 2007, pp. 1-4.

[21] L. Ji, P. Qin, J. Li, and L. Zhang, "1-D electronic beam-steering partially reflective surface antenna," *IEEE Access*, vol. 7, pp. 115959-115965, 2019.

[22] R. Guzman Quiros, A. R. Weily, J. L. Gomez Tornero, and Y. J. Guo, "A Fabry-Pérot antenna with two-dimensional electronic beam scanning," *IEEE Trans. Antennas Propag*., vol. 64, no. 4, pp. 1536-1541, Apr. 2016.

[23] P. Xie, G. Wang, H. Li, and J. Liang, "A dual-polarized two-dimensional beam-steering Fabry-Pérot cavity antenna with a reconfigurable partially reflecting surface," *IEEE Antennas Wireless Propag. Lett*., vol. 16, pp. 2370-2374, 2017.

[24] L. Ji, Z. Y. Zhang, and N. W. Liu, "A two-dimensional beam steering partially reflective surface (PRS) antenna using a reconfigurable FSS structure," *IEEE Antennas Wireless Propag. Lett*., vol. 18, no. 6, pp. 1076-1080, Jun. 2019.

[25] T. Debogovic and J. Perruisseau-Carrier, "Array-fed partially reflective surface antenna with independent scanning and beamwidth dynamic control," *IEEE Trans. Antennas Propag*., vol. 62, no. 1, pp. 446-449, Jan. 2014.

[26] L. Ji, Y. J. Guo, P. Y. Qin, S. X. Gong, and R. Mittra, "A reconfigurable partially reflective surface (PRS) antenna for beam steering," *IEEE Trans. Antennas Propag*., vol. 63, no. 6, pp. 2387-2395, Jun. 2015.

[27] M. D. Hougs, O. S. Kim, and O. Breinbjerg, "A ray-tracing method to analyzing modulated planar Fabry-Perot antennas," in *Proc. 9th Europ. Conf. Antennas Propag.* (*EuCAP*), Lisbon, Portugal, Apr. 12-17, 2015, pp. 1-4.

[28] J. Wu, D. Zhou, X. Lei, J. Gao, and H. Hu, "A high gain Fabry-Perot cavity antenna designed by modified ray tracking model," in *Proc. Int. Workshop Antenna Technol. (iWAT)*, Nanjing, China, Mar. 5-7, 2018, pp. 1-4.

[29] Y. Luo, Y. He, S. Xu, and G. Yang, "Programmable zeroth-order resonance with uniform manipulation using the nonlinearity of PIN diodes," *IEEE Antennas Wireless Propag. Lett*., vol. 18, no. 11, pp. 2419-2423, Nov. 2019.

[30] Q. Liang and B. K. Lau, "Comparison of capacitive and inductive partially reflective surface antenna using ray-tracing," *in Proc. 16th Europ. Conf. Antennas Propag. (EuCAP'2022)*, Madrid, Spain, Mar. 27- Apr. 1, 2022.

[31] Q. Liang and B. K. Lau, "Analysis of partially reflective surface antenna with different reflection magnitudes using ray-tracing," in *Proc. 2022 2022 IEEE Int. Symp. Antennas Propag. USNC/URSI Nat. Radio Sci. Meeting (APS'2023)*, Denver, USA, July 10-15, 2022.

[32] L. Zhou, X. Chen, Y. Cui, and X. Duan, "Comparative effects of capacitive and inductive superstrates on the RCA's gain," *IET Microw. Antennas Propag*., vol. 12, pp. 1834-1838, May 2018.

[33] A. Foroozesh and L. Shafai, "Investigation into the effects of the reflection phase characteristics of highly-reflective superstrates on resonant cavity antennas," *IEEE Trans. Antennas Propag*., vol. 58, no. 10, pp. 3392-3396, Oct. 2010.

[34] A. H. Abdelrahman, F. Yang, A. Z. Elsherbeni, and P. Nayeri, *Analysis and Design of Transmitarray Antennas*. Morgan & Claypool, 2017.

[35] D. M. Pozar. *Microwave Engineering*, 3rd ed., John Wiley & Sons, Inc., 2005.

[36] Skyworks. Products: SMP1340-079LF. [Online]. Available: https:// www.skyworksinc.com/en/Products/Diodes/SMP1340-Series

[37] Q. Liang and B. K. Lau, "Co-designed millimeter-wave and sub-6GHz antenna for 5G smartphones," *IEEE Antennas Wireless Propag*. *Lett*., vol. 21, no. 10, pp. 1995-1999, Oct. 2022.

Paper III

Dual-Band Shared-Aperture Antenna with Single-Layer Partially Reflecting Surface

Dual-band shared-aperture Fabry-Pérot cavity (DS-FPC) antennas with single-layer partially reflective surface (PRS) are inherently limited in the achievable frequency ratio. This paper analyzes such antennas to derive the feasible range of frequency ratio and thereafter proposes a dual-band shared-aperture antenna that can fill the frequency ratio gap. The proposed antenna integrates a short backfire antenna (SBA) for the low band (LB) and a Fabry-Pérot cavity (FPC) antenna for the high band (HB), utilizing a shared single-layer PRS and a parasitic element. In LB, using a parasitic element that is transparent for HB, the SBA works well despite its low profile. In HB, the FPC antenna works with the first-order FPC mode. A prototype working at 5.5GHz and 9GHz was fabricated and measured. The overall height of the antenna is 0.36 and 0.59 wavelength in LB and HB, respectively. The prototype achieves 7.3% and 6.7% of measured overlapping 10dB impedance bandwidth and 3dB realized gain bandwidth, as well as peak realized gains of 10.3 and 14.6dBi, in LB and HB, respectively.

Qiuyan Liang, Buon Kiong Lau and Gaonan Zhou,
"Dual-Band Shared-Aperture Antenna with Single-Layer Partially Reflecting Surface,"
IEEE Trans. Antenna Propag., 2023, Submitted.

1 Introduction

The demand for high speed wireless connectivity has grown tremendously over the past decade [1], [2]. To meet this demand, a diverse range of standards with different operating frequencies and protocols have been put forward and adopted for mobile communications [3]. This trend has led to the increasing need for multi-band antennas. A shared-aperture antenna is an attractive multi-band solution since it integrates antennas of different frequency bands in a shared space and provides high space utilization [4]-[7]. In addition, due to the adoption of higher frequency bands and hence smaller cells, there is also a growing need for low-cost antennas that can offer higher gains than classical antennas.

The Fabry-Pérot cavity (FPC) antenna can achieve medium-to-high gains with low cost and low complexity [8]-[9]. In recent years, dual-band shared-aperture FPC (DS-FPC) antennas have been proposed for a variety of applications, such as synthetic aperture radars, satellite communications, dual-band wireless local area network (WLAN) and mobile communications [10]-[23]. Based on the working principle of FPC antenna, the waves from the feeding source are reflected multiple times in the cavity formed by a partial reflective surface (PRS) and a fully reflecting ground, with each incident wave at the PRS also producing a transmitted wave [8]. An FPC antenna achieves resonance when the multiple transmitted waves are in-phase, which requires that the cavity length l (or PRS height) satisfies the classical equation

$$l = \left(\frac{\varphi_r}{2\pi} - 0.5 \right) \frac{\lambda}{2} + N \frac{\lambda}{2} \ , \tag{1}$$

where λ is the wavelength in free space, φ_r is the reflection phase of the PRS and N ($N = 0, 1, 2, \ldots$) is the order of the FPC mode [8], [10]. For a DS-FPC antenna, the FPC antenna's resonance condition (1) needs to be satisfied in both bands.

DS-FPC antennas could be implemented with a single-layer PRS [10]-[14]. In [10]-[12], the DS-FPC antennas are realized with a shared PRS height l but with different N's for the low band (LB) and high band (HB). The achieved HB-to-LB frequency ratios are 1.88, 1.9 and 1.79, respectively. In [13], with a shared PRS height l and the same N for the two bands, the achieved frequency ratio is 1.1. It can be observed that using a shared single-layer PRS, the frequency ratio tends to be close to the ratio of N's, the orders of the utilized FPC modes, which can be explained from (1), as follows: A unit cell of a single-layer PRS can be considered as a two-port system, and the reflection phase of the PRS is related to its reflection magnitude [24]. To achieve high gain for the antenna, a sufficiently high reflection magnitude is required [16], which results in the reflection phase φ_r being constrained within a specific range. Therefore, with the same l and the narrow range of feasible φ_r values, the ratio of the two wavelengths (and the two corresponding operating frequencies) is mainly determined by the ratio of N's for the two bands as obtained from (1).

In [14], the frequency ratio of 1.49 is obtained with a shared PRS height l and the same N by employing a PRS substrate with thickness of 0.16λ in HB (30GHz). However, this method may not be practical for some low frequency applications due to the relatively thick PRS substrate needed. Therefore, existing DS-FPC antennas implemented with single-layer PRS do not offer flexible frequency ratio in general, which limit their usefulness in dual-band applications that involve some commonly used frequency bands, such as S-band (2-4GHz), C-band (4-8GHz), and X-band (8-12GHz).

To realize a more flexible frequency ratio, artificial-magnetic-conductor (AMC) ground planes have been adopted in DS-FPC antennas to compensate for the propagation phases in LB [15] or HB [16]. However, these antennas exhibit relatively narrow overlapping bandwidths between the 10dB impedance bandwidths and the 3dB realized gain bandwidths in the corresponding bands. Another approach to realize a flexible frequency ratio is to use two separate PRS layers for the two FPCs working in the two bands [17]-[22]. With different cavity heights l's but with the same N, the resonance condition can be satisfied individually in both bands. However, the overall profiles of these antennas are relatively high, especially for HB due to the presence of LB resonant cavity. Moreover, the two required PRS layers also increase the complexity of the antenna structure.

In addition to designing dual-band FPCs, dual-band shared-aperture antennas can also be implemented using two types of antennas with different working principles. A dual-band shared-aperture antenna combining a folded transmitarray antenna working in HB and a FPC antenna working in LB with a large frequency ratio of 2.8 has been proposed [23]. However, since phase-shifting surface and electrically larger volume are required for the folded transmitarray antenna to work normally, four layers of PRS are employed in the antenna, which leads to a bulky overall structure. Therefore, it is important to integrate a suitable type of antenna with a FPC antenna to realize a dual-band shared-aperture antenna with a flexible frequency ratio, a low-complexity structure, and a low antenna profile.

In this context, this paper proposes a new dual-band shared-aperture antenna design integrating a short backfire antenna (SBA) working in LB and a FPC antenna working in HB by using a shared single-layer PRS and a parasitic element. The contributions are:

- The range of feasible frequency ratio in a traditional DS-FPC antenna with single-layer PRS is calculated for the first time. This range is obtained from the ranges of the PRS's reflection phase in the two bands, given a specific reflection magnitude range for gain enhancement.
- A PRS with different unit cells for the inner and outer parts is utilized to realize different reflection coefficient distributions in LB and HB. In LB, the operation of a low-profile SBA is achieved by utilizing a PRS with nonuniform

distribution in the reflection coefficient and a parasitic element that is transparent for HB. In HB, the FPC antenna is resonant at the first-order FPC mode. The proposed antenna provides more flexible frequency ratio with a simple structure and it fills the frequency ratio gap of traditional DS-FPC antennas.

- To demonstrate the significance of the proposed design philosophy, a prototype working at 5.5GHz and 9GHz with HB-to-LB frequency ratio of 1.64 is designed, fabricated and measured. The antenna has an overall profile height of 0.36λ and 0.59λ in LB and HB, respectively. The measured overlapping 10dB impedance bandwidths and 3dB realized gain bandwidths in LB and HB are 7.3% and 6.7%, respectively. The measured peak realized gains in LB and HB are 10.3 and 14.6dBi, respectively. The proposed antenna not only provides a flexible frequency ratio, but it also compares favorably with recent dual-band shared aperture designs in impedance-gain bandwidth, height, and overall size.

The rest of the paper is organized as follows: Section 2 analyzes the range of feasible frequency ratio for traditional DS-FPC antennas with single-layer PRS. The design of the proposed dual-band shared-aperture antenna is described in detail in Section 3. Section 4 presents the measurement results of the fabricated prototype. Finally, Section 5 provides the conclusions.

2 Frequency Ratio Analysis For DS-FPC Antennas

As mentioned in the introduction, traditional DS-FPC antennas with single-layer PRS exhibit inflexible frequency ratio since the reflection phases of the PRS is constrained within a specific range. This section analyzes the above limitation to determine the feasible range of the frequency ratio, both without and with the requirement for a low-profile antenna structure. In this paper, the studied range of frequency ratio is between 1 and 2, for potential dual-band applications that combine commonly used bands in the S-band, C-band, and X-band.

2.1 Analysis of Reflection Phase Range for Enhanced Gain

As mentioned, high gain PRS antennas require sufficiently large reflection magnitude to confine the power between the PRS and the fully ground plane [16]. In this subsection, the PRS type and the reflection phase variation near the resonance frequency with maximum reflection is first analyzed. Then, the relationship between the reflection magnitude and reflection phase is derived, which shows that capacitive and inductive PRSs have opposite trends in reflection phase as reflection magnitude decreases. These relationships define the upper and lower boundaries of

Table 1: Variations of PRS properties near resonant frequency.

Frequency f	$f_0 - \Delta f$	f_0	$f_0 + \Delta f$
Reactance	< 0	0	> 0
φ_r	$\pi + \Delta\varphi_r$	π	$\pi - \Delta\varphi_r$
PRS Type	Capacitive	-	Inductive

the reflection phase, given a specific range of reflection magnitude for gain enhancement, as detailed in the following.

A unit cell of a single-layer PRS can be considered as a two-port system regardless of the unit cell shape. It is equivalent to a series LC circuit and acts essentially as a short circuit at the resonance frequency (i.e., f_0), providing maximum reflection [24]-[25]. In circuit terms, the PRS properties (i.e., equivalent reactance and reflection phase) vary near the resonance frequency [26], as listed in Table 1. At the resonance frequency f_0, the equivalent reactance is 0Ω and the reflection phase of the PRS is π. As the frequency increases from $f_0 - \Delta f$ to $f_0 + \Delta f$, the equivalent reactance increases monotonically from a negative to a positive value, whereas the reflection phase of the PRS decreases monotonically from $\pi + \Delta\varphi_r$ to $\pi - \Delta\varphi_r$ (Δf and $\Delta\varphi_r$ are small and positive values). The PRS is changed from being a capacitive one to an inductive one with the frequency variation, according to the sign of the equivalent reactance [27]. Therefore, the reflection phase of the capacitive PRS unit cell is larger than π, whereas that of the inductive PRS unit cell is less than π near the resonance frequency with maximum reflection.

Assuming that the PRS layer is lossless, symmetric and reciprocal, and neglecting the higher order harmonics of the PRS layer, the relationships between the reflection magnitude ρ and the reflection and transmission phases φ_r and φ_t have been derived [24]. The expressions, which are independent of the unit cell structure, are given by [24]

$$\rho = \pm \sin \varphi_t , \tag{2}$$

$$\varphi_r - \varphi_t = \pm \frac{\pi}{2}. \tag{3}$$

Inserting (3) into (2), the reflection magnitude ρ near the resonant frequency with maximum reflection becomes

$$\rho = -\cos \varphi_r . \tag{4}$$

From (4), and based on the range of reflection phase φ_r of two types of PRS provided in Table 1, it can be deduced that when the reflection magnitude ρ decreases, the reflection phase φ_r of the inductive PRS decreases, whereas that of the capacitive PRS increases. Given the range of reflection magnitude $1 > \rho > 0.707$ (-3dB) where there is more power in the reflected waves than the transmitted ones to facilitate

gain enhancement, the corresponding reflection phase ranges are ($3\pi/4$, π) and (π, $5\pi/4$) for inductive and capacitive PRSs, respectively.

2.2 Analysis of Frequency Ratio Range for Enhanced Gain

Traditional DS-FPC antennas with single-layer PRS use a shared resonant cavity for both bands. By using a proper unit cell structure, the shared PRS exhibits desirable reflection magnitudes and phases to satisfy the FPC resonance condition in both LB and HB. From (1), with a shared l for both bands, the frequency ratio can be expressed as

$$\frac{f_H}{f_L} = \frac{\frac{\varphi_{rH}}{2\pi} - 0.5 + N_H}{\frac{\varphi_{rL}}{2\pi} - 0.5 + N_L}, \tag{5}$$

where f_L and f_H represent the resonant frequency of the FPC in LB and HB, respectively. N_L and N_H are the orders of the FPC modes for LB and HB, respectively. N_L is chosen as 1 to minimize the cavity height (while being a physical solution). Therefore, with a chosen N_H, the frequency ratio is determined by the upper and lower limits of the reflection phases φ_{rH} and φ_{rL}. Since the range of φ_r has been obtained in Section 2.1, the range of frequency ratio for a specific N_H can be calculated.

When $N_H = 1$, both the LB and HB FPCs operate at the first-order FPC mode. The frequency ratio range of (1, 1.29) can be obtained with $\varphi_{rH} > \varphi_{rL}$, where 1.29 corresponds to the PRS having the reflection phases of $\varphi_{rH} = 5\pi/4$ (capacitive) and $\varphi_{rL} = 3\pi/4$ (inductive) in HB and LB, respectively. The upper limit of 1.29 corresponds to a PRS height of $l = 0.56\lambda_H$, calculated from (1). The frequency ratio could be increased further by increasing φ_{rH} or decreasing φ_{rL}, but the reflection magnitudes of the PRS in HB and LB will further decrease according to (4), leading to a lower gain due to the lack of reflection.

Furthermore, for a fixed frequency ratio, there is a tradeoff between the gain performances in the two bands. For example, given a frequency ratio, when a higher reflection magnitude is chosen for a higher gain in HB (corresponding to a smaller φ_{rH} for capacitive PRS unit cell), the calculated φ_{rL} for LB will decrease according to (5). The smaller φ_{rL} corresponds to a lower reflection magnitude, which leads to a lower antenna gain in LB.

When $N_H = 2$, the HB FPC operates at the second-order FPC mode with a larger profile (or height) than the case of $N_H = 1$. The frequency ratio range of (1.67, 2.43) can be obtained, where 1.67 corresponds to the PRS with the reflection phases of $\varphi_{rH} = 3\pi/4$ (inductive) and $\varphi_{rL} = 5\pi/4$ (capacitive), and 2.43 corresponds to the PRS with the reflection phases of $\varphi_{rH} = 5\pi/4$ (capacitive) and $\varphi_{rL} = 3\pi/4$ (inductive),

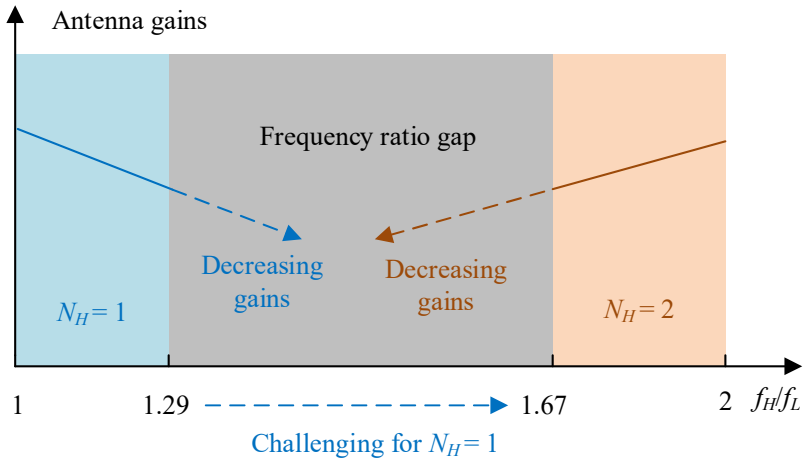

Figure 1: Illustration of the frequency ratio gap and predicted gain variation.

respectively. The lower limit of 1.67 corresponds to a PRS height of $l = 0.94\lambda_H$, as calculated from (1). Similarly, the frequency ratio outside this range can only be achieved by decreasing the reflection magnitudes of the PRS, which decreases the antenna gains in both bands according to (4).

The achievable frequency ratio ranges given $1 > \rho > 0.707$ (-3dB) and the predicted trends in gain variation of traditional DS-FPC antennas with $N_H = 1$ and $N_H = 2$ are illustrated in Fig. 1, within the range of interest (1, 2). Therefore, the frequency ratio gap is given by [1.29, 1.67].

2.3 FPC Mode Order Consideration for Low-Profile Single-Layer PRS Antenna

As discussed, the frequency ratio gap given the reflection magnitude requirement of $1 > \rho > 0.707$ cannot be filled with either $N_H = 1$ or $N_H = 2$ for a traditional shared dual-band FPC formed by a single-layer PRS, due to gain degradation. However, achieving the frequency ratio of beyond 1.67 with $N_H = 2$ comes at a cost. It can be seen from (1) a higher FPC order leads to a larger PRS height given a specific reflection phase of the PRS. In fact, the analysis in Section 2.2 shows that a relatively large PRS height of $0.94\lambda_H$ is required with $N_H = 2$ to achieve a design at the upper boundary of the frequency ratio gap (i.e., 1.67). Therefore, if low-profile design is the only requirement, then $N_H = 1$ would be preferable to $N_H = 2$. However, as depicted in Fig. 1, utilizing a frequency ratio beyond 1.29 with $N_H = 1$ will result in smaller and smaller antenna gain. For example, consider the extreme case where

the frequency ratio is 1.67 (lower limit for $N_H = 2$), which can be achieved with $\varphi_{rH} = 3\pi/2$ (capacitive) and $\varphi_{rL} = \pi/2$ (inductive) in HB and LB, respectively, for the case of $N_H = 1$. The corresponding theoretical reflection magnitudes of the PRS, as calculated from (4) with these two reflection phases are zero, implying no gain enhancement to the feeding source in both bands. In contrast, this ratio is feasible for $N_H = 2$, as discussed in Section 2.2. Therefore, when a low-profile solution is desired, it is even more challenging to design a DS-FPC antenna with single-layer PRS for flexible frequency ratio.

3 Proposed Dual-Band Shared-Aperture Antenna

Given the aforesaid fundamental limitations in realizing a low-profile DS-FPC antenna with single-layer PRS, a shared-aperture design approach is adopted in this work, where the single-layer PRS is utilized for FPC resonance in HB and a different function in LB. To demonstrate the frequency ratio flexibility of the approach, a dual-band shared-aperture antenna with single-layer PRS is designed to achieve the frequency ratio of 1.64 (LB at 5.5GHz, HB at 9GHz). The ratio is chosen to be significantly above the upper boundary of frequency ratio for $N_H = 1$ (i.e., 1.29). A similar dual-band requirement in 5GHz and 9GHz was previously considered for a dual-layer PRS design [20].

Unlike the traditional DS-FPC antenna with a shared dual-band FPC, the proposed antenna integrates a FPC antenna and a short backfire antenna (SBA), which is a type of high gain antenna with a typical profile of 0.5 free-space wavelength (0.5λ) [28]. The single-layer PRS is designed to be capacitive, to achieve a higher gain for the FPC antenna [27]. In addition, the PRS height calculated from (1) for the capacitive PRS is larger than 0.5λ, so the FPC antenna is designed for HB, such that the shared PRS height can still be close to the typical SBA profile of 0.5λ in LB. Moreover, as will be detailed in Section 3.2, a low-profile SBA working in LB is designed with a PRS and a parasitic element, to facilitate a smooth integration with the HB FPC antenna with a large frequency ratio of 1.64.

3.1 Antenna Structure and Shared-Aperture Principle

The simulation model of the proposed antenna is depicted in Fig. 2. It consists of a PRS, a reflecting ground, feeding sources for the two bands and a parasitic element placed above the LB feeding source. The supporting Nylon spacers in the simulated model has the diameter of 2mm (with dielectric constant $\varepsilon_r = 4.3$ and loss tangent $\tan\delta = 0.004$). The PRS consists of a single-layer substrate (RO4350 with $\varepsilon_r = 3.66$, $\tan\delta = 0.004$, and thickness $t_1 = 0.508$mm). The unit cells are printed on the bottom side of the substrate.

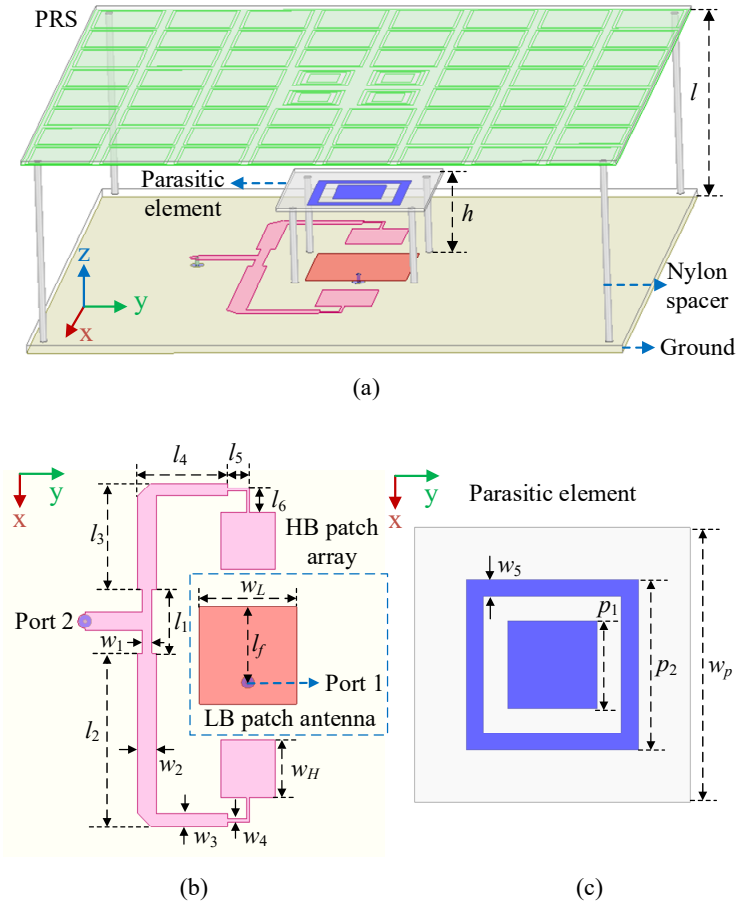

Figure 2: Geometry of the proposed antenna. (a) 3D view (l = 19mm, h = 10mm). (b) Feeding sources (l_1 = 9mm, l_2 = 24.3mm, l_3 = 14.9mm, l_4 = 12.6mm, l_5 = 3mm, l_6 = 3.4mm, w_1 = 1.3mm, w_2 = 2.6mm, w_3 = 1.8mm, w_4 = 0.4mm, w_L = 13.8mm, l_f = 11.1mm, w_H = 8mm, l_H = 7.6mm). (c) Parasitic element (w_5 = 1.3mm, p_1 = 6.5mm, p_2 = 12.5mm, w_p = 21mm).

As shown in Fig. 3, the PRS of 8 × 8 unit cells uses a different unit cell structure for the inner four elements as compared to the outer ones. Each inner unit cell consists of two square slots, whereas each outer unit cell consists of only one square slot. The substrate for the feeding source is also RO4350 but with the thickness of t_2 = 1.016mm. The HB antenna employs a 1 × 2 patch array as the feeding source. The feeding network for the patch array is printed on the top layer of the substrate and excited with Port 2. The LB antenna employs a patch antenna with a parasitic element above as the feeding source. The substrate for the parasitic element is the same as that of the PRS. The parasitic element consists of an outer ring and an inner patch printed on the bottom side of the substrate.

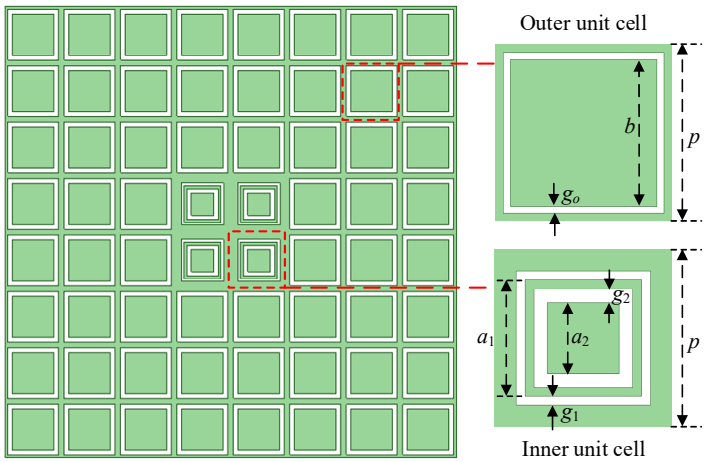

Figure 3: Layout of PRS (a_1 = 6.5mm, a_2 = 4mm, b = 8.2mm, p = 10mm, g_o = 0.4mm, g_1 = 0.5mm, g_2 = 0.8mm).

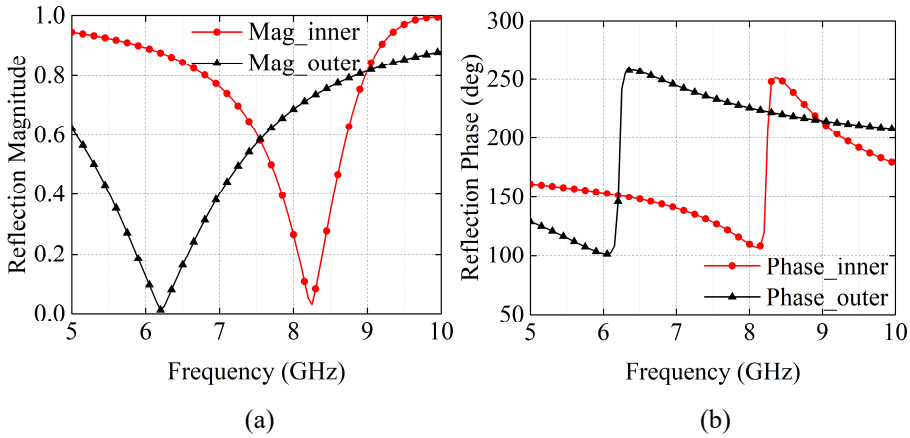

Figure 4: (a) Reflection magnitudes and (b) reflection phases of the unit cells.

The reflection coefficients of the unit cells are shown in Fig. 4. At 9GHz, both the inner and outer unit cells are designed for the reflection magnitude and phase of ρ_{1H} = ρ_{2H} = 0.82 and φ_{1H} = φ_{2H} = 214° (capacitive), respectively. With large reflection magnitudes, the PRS enables the antenna to operate as FPC antenna in HB, as illustrated in Fig. 5(a). The theoretical PRS height for the first order FPC mode (N_H = 1), as determined by φ_{1H} and φ_{2H} is l = 18.2mm. The optimized value for the final structure is l = 19mm, to account for practical aspects (e.g., oblique wave incidence, presence of substrate materials) that are neglected in the theoretical model as well as to achieve a good tradeoff in the gain and bandwidth performance.

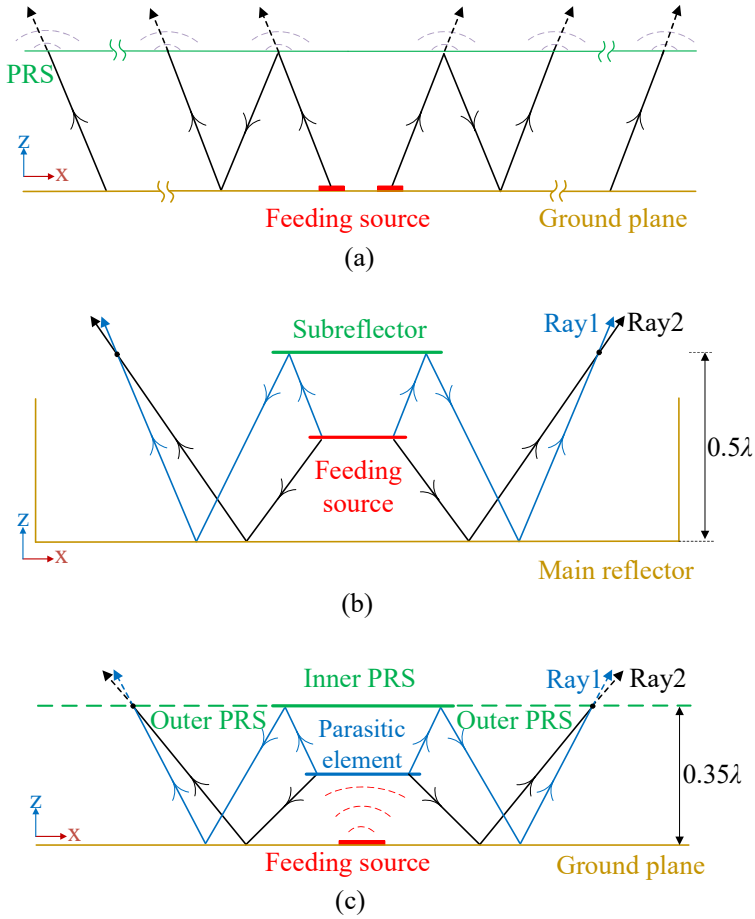

Figure 5: Working principle of (a) proposed HB antenna, (b) traditional SBA, and (c) proposed LB antenna.

In contrast, the inner and outer unit cells of the PRS are designed to behave differently at 5.5GHz, such that the LB antenna operates as an SBA. As shown in Fig. 5(b), a traditional SBA consists of a main reflector, a small subreflector and a feeding source between the two reflectors [28]. The waves from the feeding source are reflected by the two reflectors and the wave components along different paths satisfy an in-phase condition as shown in Fig. 5(b) [29]. The difference in the path lengths of Ray1 and Ray2 are mainly attributed to the initial upward path of Ray1 from the feeding source to the subreflector, the reflection at the metallic surface of the subreflector (giving an equivalent path length of 0.5λ), and part of the continuing downward path of Ray1 from the subreflector until it reaches the height of the feeding source. For Ray1 and Ray2 to be in phase, this additional path of Ray1

relative to Ray2 should be close to a positive integer multiple of 1λ. Therefore, the proposed PRS is designed for high reflection in the inner parts and low reflection in the outer parts, to mimic a subreflector in LB. Specifically, at 5.5GHz, the inner unit cell has the reflection magnitude and phase of $\rho_{1L} = 0.92$ and $\varphi_{1L} = 158°$ (inductive), respectively, whereas the outer unit cell has the reflection magnitude and phase of $\rho_{2L} = 0.41$ and $\varphi_{2L} = 115°$ (inductive), respectively. As will be elaborated in the next subsection, the relatively low reflection magnitude of the outer unit cell is also designed to enable the SBA operation at a profile lower than the conventional requirement of around 0.5λ.

As opposed to a traditional SBA, the "floating" LB feeding source is replaced with a parasitic element and a feeding source (patch antenna) built onto the main reflector, as shown in Fig. 5(c). The parasitic element, with energy coupled from the excited patch antenna (fed with Port 1), acts as an equivalent feeding source between the subreflector (inner PRS) and the main reflector (ground plane). Apart from simplifying the feeding structure, the parasitic element also functions as a stacked patch and introduces a second (higher) resonance, which can be used to enhance the LB impedance bandwidth. As such, the frequency of the higher resonance can be tuned by the distance between the feeding patch and the parasitic element, and a tradeoff exists between the bandwidth and the depth of the dual-resonances. Moreover, the patch's feeding position l_f (see Fig. 2(b)) is also optimized for impedance matching. However, it was observed in the simulation that the slight variations in the height of the parasitic element within this tradeoff has little effect on the LB antenna gain. Furthermore, the parasitic element is designed as a transparent unit cell in HB, with a low reflection magnitude of 0.02 at 9GHz. Given its self-resonant structure and low coupling design (with large empty space around the metallic parts), the standalone unit cell can be expected to show similar behavior as a periodic structure. Hence, the parasitic element has minimal impact on the HB FPC mode.

3.2 Working Principle of LB SBA with Reduced Profile Height

Having described the basic operation of the HB FPC antenna and the LB SBA antenna, the focus in this subsection is on describing how the traditional SBA (in Fig. 5(b)) was modified to work for the PRS height determined for normal FPC antenna operation in HB.

As stated earlier, the height of the PRS (above the ground plane) is l = 19mmm, or $0.35\lambda_L$ at 5.5GHz (λ_L is the free-space wavelength at 5.5GHz), which is smaller than the typical subreflector height of 0.5λ used in a traditional SBA. It can be seen in Fig. 5(c) that the vertical distance between the subreflector (inner PRS) and the equivalent feeding source (parasitic element) is reduced (being $\sim 0.14\lambda_L$) in the proposed antenna, as compared to the traditional SBA shown in Fig. 5(b). The

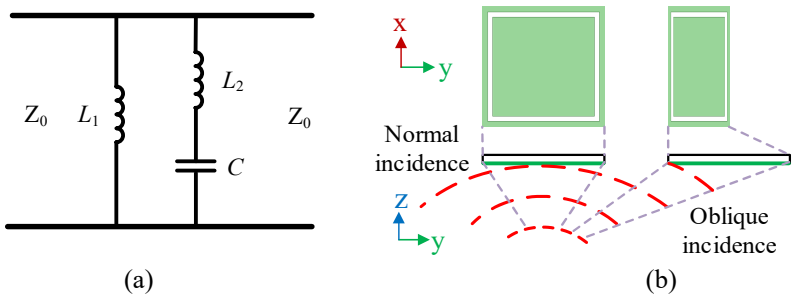

Figure 6: (a) Equivalent circuit of outer PRS unit cell, and (b) equivalent cross section for normal incidence and oblique incidence.

reduced height shortens the propagation path of Ray1 and disturbs the in-phase condition between Ray1 and Ray2, which can lead to a reduced antenna gain.

For the proposed LB antenna, the expected gain degradation due to the reduced PRS height is mitigated by utilizing the outer unit cells of PRS. An outer unit cell of the PRS with an etched slot has the equivalent circuit shown in Fig. 6(a) [30]. When the incident angle of the wave increases, the effective cross section area of the unit cell changes as shown in Fig. 6(b). As a result, the equivalent capacitance C between the inner patch and the outer edge decreases and the equivalent inductance L_2 of the inner patch increases, which leads to a decrease in the equivalent reactance of the inductive outer unit cell and an increase in the transmission phase [26]. As the simulation results in Fig. 7 show, the outer unit cell has positive and increasing transmission phase at 5.5GHz as the incident angle increases. This means that a smaller phase delay is introduced to the wave with a larger incident angle. As can be seen in Fig. 5(c), the incident angle of Ray2 is larger than that of Ray1, so the phase delay introduced by the outer unit cells would be larger for Ray1 than for Ray2, thus reducing the phase difference due to the reduced profile height.

In addition to Ray1 and Ray2 that are reflected by the two reflectors (i.e., subreflector and ground), there are also wave components from the parasitic element and the feeding patch (not depicted in Fig. 5) that transmit directly through the outer PRS. And since the transmitted power is more dominant than the reflected power for the outer unit cells of the PRS (that has low reflection magnitude in LB), the outer PRS cells have a function equivalent to a lens. The outer cells at the edges of the PRS provide more phase compensation for the transmitted waves than those near the middle, due to the larger angles of the incident waves. This leads to a flatter phase front to the transmitted wave components across the PRS, which facilitates a higher gain than that of a low-profile SBA that has no outer unit cell. Therefore, it can be concluded the outer unit cells' transmission phase variation with incident angle enables the in-phase condition to be achieved by an SBA (for both direct and indirect propagation paths), despite the PRS (specifically, its inner unit cells with the role of a subreflector) having a reduced profile.

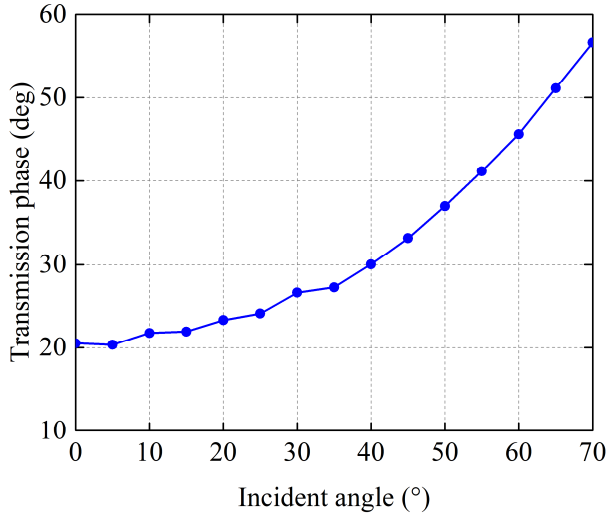

Figure 7: Transmission phase variation of outer unit cell with oblique incident angle at 5.5GHz.

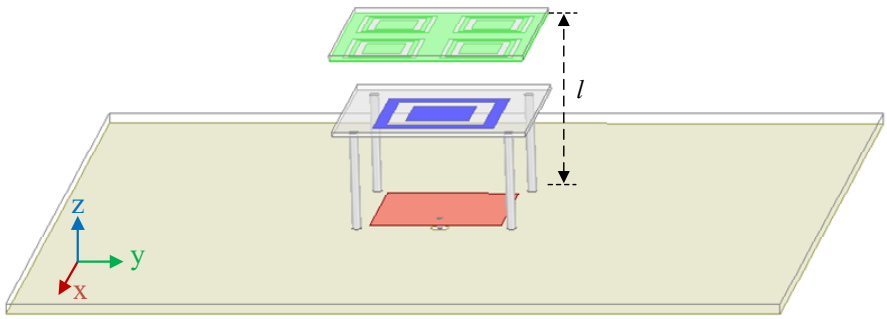

Figure 8: SBA without outer PRS unit cell, used for comparison.

To better quantify the gain enhancement effect of the outer unit cells, a LB SBA antenna without the outer PRS unit cells (see Fig. 8) is simulated at 5.5GHz with $l = 0.35\lambda_L$, for comparison with the proposed antenna (with outer PRS unit cells). The SBA antenna without the outer PRS unit cells and with $l = 0.5\lambda_L$ is also simulated for comparison. The resulting radiation patterns in the *y*-*z* plane are shown in Fig. 9. It can be seen that, without the outer unit cells, the gain is decreased significantly from 11.9dBi to 4.7dBi when the antenna profile is reduced from $l = 0.5\lambda_L$ to $0.35\lambda_L$. However, by employing the outer unit cells, the gain of the SBA is almost fully restored to that of the typical profile of $0.5\lambda_L$ (i.e., 11.1dBi), representing an increase

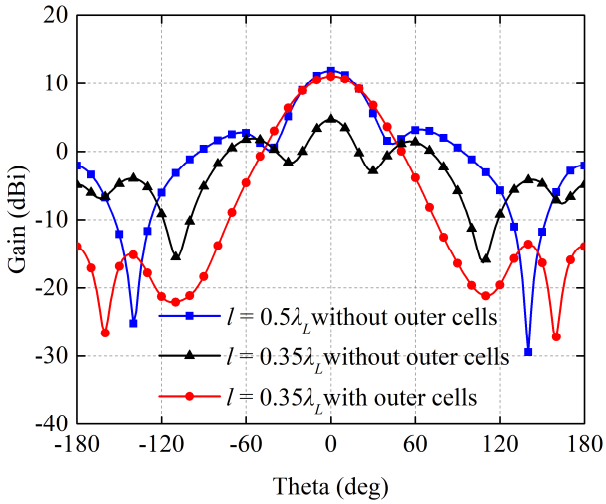

Figure 9: Radiation patterns of SBAs in *y*-*z* plane at 5.5GHz.

of 6.4dBi relative to that of the reduced profile SBA (with $l = 0.35\lambda_L$). In addition, the sidelobe level of the proposed antenna is 16dB lower than that of the SBA with $0.5\lambda_L$, which can be attributed to the PRS extending the effective antenna aperture and providing suitable amplitude tapering for sidelobe reduction.

3.3 Comparison of LB SBA with Traditional DS-FPC Antenna

Based on the theoretical analysis in Section 2.2, a large frequency ratio can result in low antenna gains for traditional DS-FPC antennas with single-layer PRS, when the FPC resonance condition is satisfied in both bands with $N_L = N_H = 1$.

To further verify the gain enhancement effect of the proposed dual-band shared-aperture antenna, a quasi-DS-FPC antenna consisting of a uniform PRS, a ground plane, and two feeding sources for the two bands is simulated. As before, the targeted frequency ratio is 1.64, to cover the 5.5GHz and 9GHz bands. Compared to the proposed antenna, the quasi-DS-FPC antenna has no parasitic element and the PRS consists of only the outer unit cells shown in Fig. 3.

Since the unit cells of the quasi-DS-FPC antenna have the same reflection magnitude as both the outer and inner ones of the proposed antenna at 9GHz, the quasi-DS-FPC antenna satisfies the FPC resonance condition in HB and hence retains similar HB performance as the proposed antenna. However, its unit cells provide $\varphi_{rL} = \varphi_{2L} = 115°$ and $\varphi_{rH} = \varphi_{2H} = 214°$ at $f_L = 5.5$GHz and $f_H = 9$GHz, respectively, as obtained for the outer unit cells in Section 3.1. Therefore, the DS-

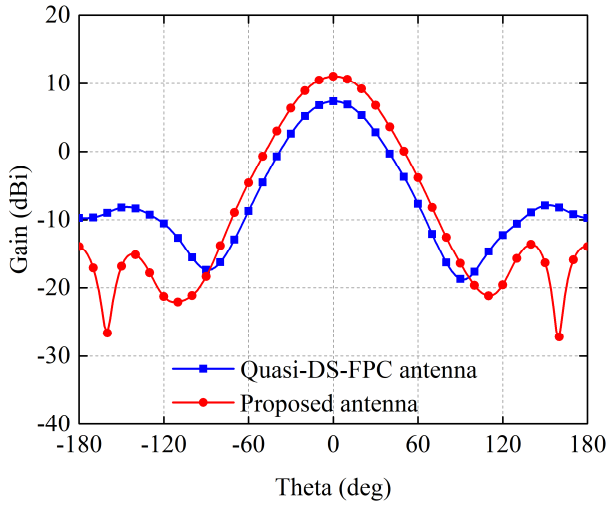

Figure 10: Radiation patterns of quasi-DS-FPC antenna and proposed SBA in *y*-*z* plane at 5.5GHz.

FPC resonance condition in (5) is not satisfied in LB, given $N_L = N_H = 1$, due to insufficient PRS height in LB. This leads to gain degradation of the quasi-DS-FPC antenna in LB. To quantify the benefit of replacing the quasi-FPC operation with the low-profile SBA of the proposed antenna, the radiation patterns in the *y*-*z* plane at 5.5GHz are shown in Fig. 10 for the quasi-DS-FPC antenna and the proposed antenna. As can be seen, the gain of the proposed antenna is 3.7dBi higher than that of the quasi-DS-FPC antenna at 5.5GHz. It is noted that the DS-FPC condition can be satisfied for a shared PRS height with a larger φ_{2H} and a smaller φ_{2L}, but the antenna gain in both bands will be low due to the small reflection magnitude, as explained in Section 2.2.

3.4 Analysis of Frequency Ratio Flexibility

The proposed dual-band antenna realizes the frequency ratio of 1.64 with $N_H = 1$. This ratio is far above the frequency ratio limitation for $N_H = 1$ of 1.29, and hence it cannot be realized with good gain by a traditional DS-FPC antenna with $N_H = 1$, as analyzed in Section 3.3. On the other hand, the frequency ratio beyond 1.67 can be achieved for $N_H = 2$, albeit with a higher antenna profile.

To analyze the potential for the proposed SBA-FPC antenna to fill the entire frequency ratio gap of [1.29, 1.67], the frequency ratio flexibility of the proposed antenna is investigated for a fixed LB center frequency f_L of 5.5GHz. For the proposed antenna, the PRS height l as determined by the HB FPC condition

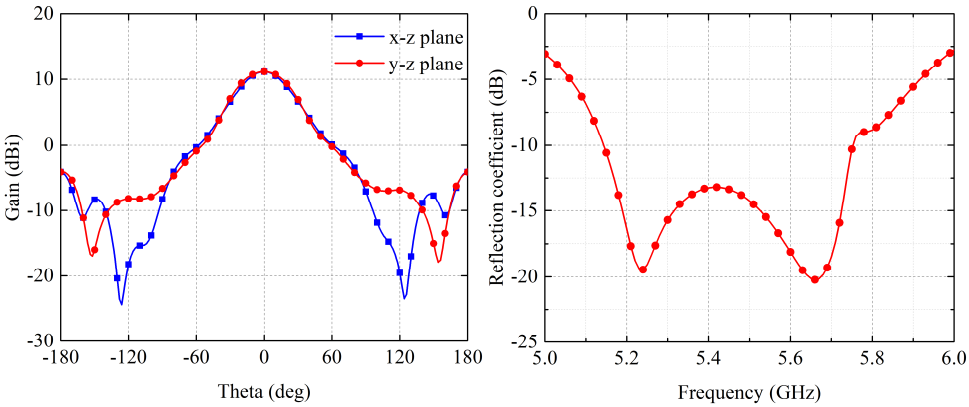

(a) (b)

Figure 11: (a) Radiation patterns in *x-z* and *y-z* planes at 5.5GHz and (b) reflection coefficient of LB SBA with $l = 0.44\lambda_L$ (24mm), h = 7mm and l_f = 11.5mm.

guarantees good HB performance. A smaller frequency ratio than that of the proposed antenna (i.e., $f_H/f_L < 1.64$) corresponds to a smaller f_H (i.e., $f_H <$ 9GHz) and a larger electrical length in LB. To ensure that the SBA part of the proposed antenna can still work well for a smaller frequency ratio (i.e., $1.29 < f_H/f_L < 1.64$), the LB SBA with different PRS heights (electrical lengths) is simulated at 5.5GHz.

With the frequency ratio of f_H/f_L = 1.64 (LB at 5.5GHz, HB at 9GHz), the PRS height l as determined by the HB FPC condition is $0.57\lambda_H$, which corresponds to $0.35\lambda_L$ in LB. However, for the frequency ratio of f_H/f_L = 1.3 (LB at 5.5GHz, HB at 7.15GHz), the PRS height is $l = 0.57\lambda_H$ (24mm) assuming unit cells with the same $\rho_{1H} = \rho_{2H} = 0.82$ and $\varphi_{1H} = \varphi_{2H} = 214°$ at 7.15GHz. This height (24mm) corresponds to $0.44\lambda_L$. Therefore, a LB SBA with $l = 0.44\lambda_L$ is simulated at 5.5GHz. As mentioned in Section 3.1, the impedance matching of the LB dual resonances is optimized by adjusting the parasitic element height h and the patch's feeding position l_f. With the vertical distance between the subreflector and the parasitic element of $0.28\lambda_L$, the waves reflected by the two reflectors (see Fig. 5(c)) can roughly satisfy the in-phase condition. Moreover, the outer unit cells of the PRS as an equivalent lens provides gain enhancement, as mentioned in Section 3.2. The LB radiation pattern cuts and reflection coefficient magnitude are given in Fig. 11. It can be seen that the LB SBA antenna can still achieve a similar high gain of 11.2dBi as for the previous ratio 1.64 (simulated gain of 10.7dBi). Therefore, it can be projected that the LB SBA antenna can be integrated with the HB FPC antenna with flexible frequency ratio from 1.3 to 1.64 with different profile heights. It is noted that the required reflection magnitudes and phases of the PRS in two frequency bands with different frequency ratios can be realized by choosing proper structural parameters for the unit cells.

To compare the antenna gain obtained by the proposed design method with that obtained by the traditional DS-FPC antenna design method for the frequency ratio of 1.3, a DS-FPC antenna with $l = 0.44\lambda_L$ at 5.5GHz is simulated. This comparison is interesting since the ratio of 1.3 is close to the upper boundary of 1.27 for $N_H = 1$. This means that a traditional DS-FPC antenna may provide competitive gain performance and should therefore be investigated. The required reflection phase of the PRS for the LB FPC antenna is 123°, which is calculated from (5) with the PRS height of $l = 0.44\lambda_L$, $N_L = N_H = 1$ and $\varphi_{2H} = 214°$ (for the same HB performance). The simulated gain of the LB FPC antenna is 9.4dBi at 5.5GHz, which is almost 2dB lower than the proposed antenna with the ratio of 1.3. The lower gain of the LB FPC antenna is due to the tradeoff of the reflection magnitudes of the PRS in two frequency bands, as mentioned in Section 2.2. Here, the utilized PRS yields a low reflection magnitude of 0.52 (corresponding to the reflection of 123°) in LB, given a high reflection magnitude of 0.82 (corresponding to the reflection of 214°) in HB.

Therefore, the proposed antenna not only provides flexible frequency ratio while retaining a low-complexity structure, it also facilitates competitive gain performance relative to traditional DS-FPC antennas with single-layer PRS even for the case where the frequency ratio is close to the upper bound of the frequency ratio limit for $N_H = 1$.

4 Measurement Verification

A prototype of the proposed dual-band shared-aperture antenna presented in Section 3.1 was fabricated (see Fig. 12). Nylon spacers are used to support the PRS substrate and parasitic element above the ground plane. The size of the antenna is 80 × 80 × 19.5mm^3.

Figure 13 shows the simulated and measured S-parameters of the proposed antenna in LB and HB. The measured 10dB impedance bandwidth of Port 1 for LB is 0.56GHz (5.29-5.85GHz). The measured bandwidth is larger than the simulated one, which can be due to the effect of soldering and slight differences in the heights of the PRS and parasitic element between the fabricated prototype and the simulation model. As described in Section 3.1, the LB dual resonance is enabled by the parasitic element. In the operating LB, the measured isolation $|S_{21}|$ between Port 1 and Port 2 is larger than 24dB. The measured 10dB impedance bandwidth of Port 2 for HB is 0.77GHz (8.66-9.43GHz). The dual resonance observed in HB is introduced by the feeding network for the patch array, depicted in Fig. 2(b). In the operating HB, the measured isolation $|S_{21}|$ between Port 1 and Port 2 is likewise larger than 24dB.

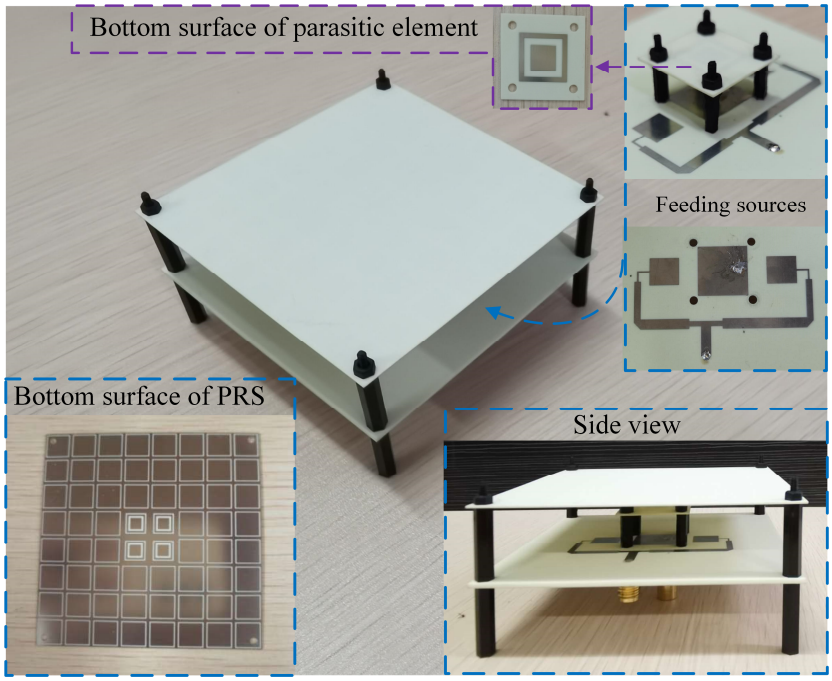

Figure 12: Prototype of the proposed dual-band shared-aperture antenna.

The simulated and measured radiation patterns of the proposed antenna in the E-plane (*x-z* plane) and H-plane (*y-z* plane) are provided for 5.5GHz (LB) and 9GHz (HB) in Fig. 14. At 5.5GHz, the antenna facilitates a pencil-shape beam with the measured realized gain of 10.2dBi and side lobe level (SLL) of -17dB. The measured realized gain and SLL are 13.9dBi and -12dB, respectively, at 9GHz. The measured cross-polarization levels of the dual-band antenna are higher than 29.0 dB and 24.0 dB at 5.5GHz and 9GHz, respectively. Figure 15 shows the realized gains of the antenna in both bands. The simulated peak realized gains of the antenna in LB and HB are 10.7dBi at 5.5GHz and 15dBi at 9.1GHz, respectively. The measured results are in general consistent with the simulation ones. The differences between the measured and simulated results are primarily due to fabrication and measurement system tolerances. It can be seen from the measured results in Figs. 13 and 15 that the overlapping bandwidth between the 10dB impedance bandwidths and 3dB realized gain bandwidths in LB and HB are 7.3% (5.3-5.7GHz) and 6.7% (8.8-9.4GHz), respectively.

To facilitate comparison with state-of-the-art designs, Table 2 presents the key parameters of 8 recent dual-band shared-aperture antennas that utilize PRS, alongside those of the proposed antenna. These antennas are designed based on the typical approaches mentioned in the introduction. The key parameters include the

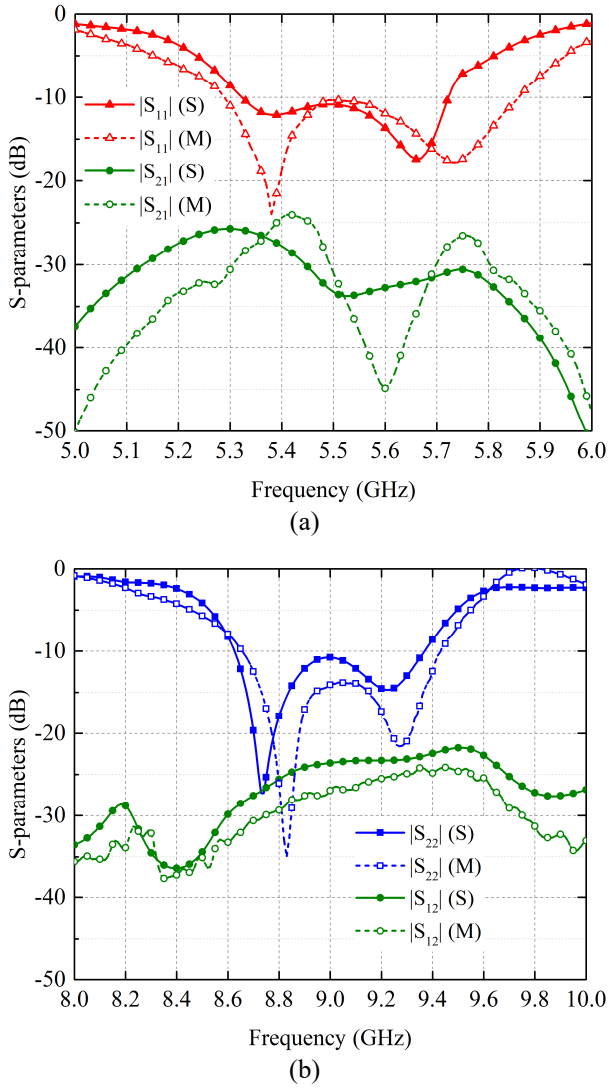

Figure 13: Simulated (S) and measured (M) S-parameters of proposed antenna in (a) LB and (b) HB.

frequency ratio, the number of PRS layers, the overlapping bandwidth between 10dB impedance bandwidth and 3dB realized gain bandwidth, the peak gain and the volume. It can be observed that the achieved frequency ratios of the DS-FPC antennas with single-layer PRS tend to be close to 1 or 2 (i.e., the ratios of FPC modes), which is consistent with the frequency ratio range analysis in Section 2.2. As verified in Section 3.4, the proposed antenna can fill the frequency ratio gap [1.3, 1.64] with proper structural design, without using traditional dual-band FPC

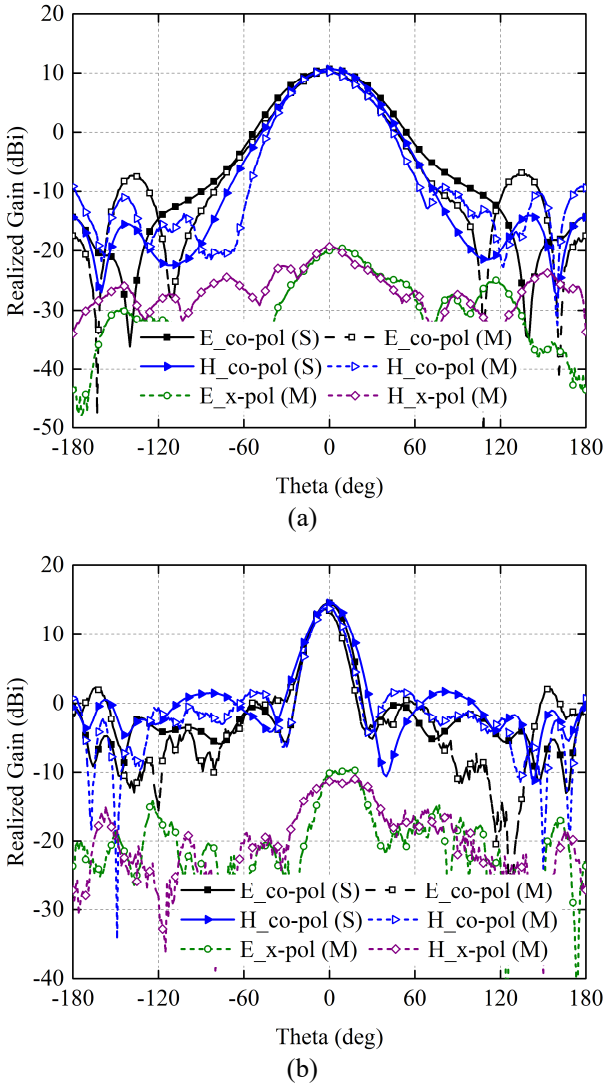

Figure 14: Simulated (S) and measured (M) radiation pattern cuts of proposed antenna in (a) LB and (b) HB.

antennas. Moreover, the proposed antenna can achieve better overlapping bandwidth in both bands than other single-layer designs. When compared with the dual-band shared aperture antennas with multiple PRS layers that give flexible frequency ratio, the proposed antenna with single-layer PRS facilitates a simpler structure. The advantages of flexible frequency ratio, simple structure, relatively low antenna profile and high space utilization efficiency make the antenna a good candidate for dual-band applications.

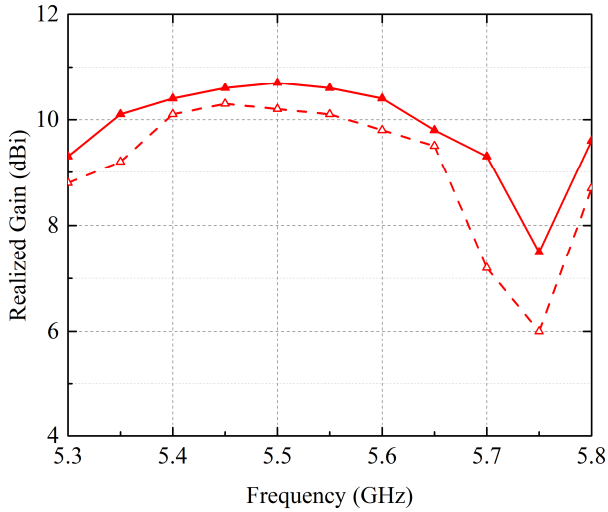

(a)

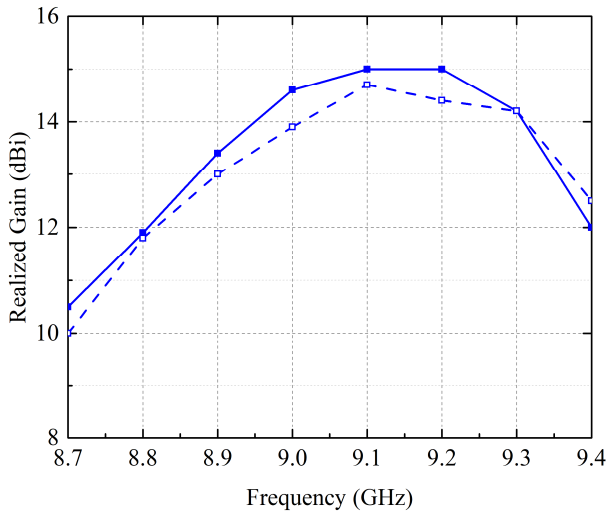

(b)

Figure 15: Simulated (solid line) and measured (dashed line) realized gains of proposed antenna in (a) LB and (b) HB.

5 Conclusion

In this paper, the frequency ratio range of the traditional DS-FPC antennas with single-layer PRS is analyzed and a frequency ratio gap is derived. A dual-band shared-aperture antenna integrating a LB SBA and a HB FPC antenna with a shared

Table 2: Comparison between the proposed and previous dual-band shared-aperture antenna using PRS

Reference	f_H/f_L	Number of PRS layers	Overlapping Bandwidth		Peak gain (dBi)		Antenna volume (λ^3)	
			LB	HB	LB	HB	LB	HB
[10]	1.87	1	1.4% (6.95GHz)	3.4% (13GHz)	16.5	20.9	2.55×2.55×0.49	4.7×4.7×0.9
[12]	1.79	1	4.1% (5.6GHz)	2.7% (10GHz)	10.3	15.8	1.49×1.49×0.28	2.67×2.67×0.49
[13]	1.10	1	1.1% (7.28GHz)	2.5% (8GHz)	13.0	13.3	2.04×2.04×0.52	2.24×2.24×0.57
[15]	1.27	1	4.5% (11GHz)	2.6% (14GHz)	15	17.5	NA×NA×0.47	NA×NA×0.58
[16]	2.24	2	1% (2.45GHz)	12.7% (5.5GHz)	13.4	15.0	1.67×1.67×0.22	3.74×3.74×0.49
[20]	1.81	2	3.4% (5.3GHz)	4.7% (9.6GHz)	16.4	20.0	2.47×2.47×0.55	4.48×4.48×0.99
[22]	1.45	2	1.4% (3.45GHz)	2.2% (5GHz)	14.0	17.5	1.56×1.56×0.56	2.27×2.27×0.81
[23]	2.80	4	4% (10GHz)	8.9% (28GHz)	13.8	23.6	2.83×2.83×0.57	7.48×7.48×1.59
Proposed	1.64	1	7.3% (5.5GHz)	6.7% (9GHz)	10.7	15	1.47×1.47×0.36	2.4×2.4×0.59

single-layer PRS is proposed to fill the gap. The PRS exhibits different reflection coefficient distributions in LB and HB. With a parasitic element which is transparent in HB and a nonuniform PRS with relatively small reflection magnitude in the outer unit cells, the LB SBA can be take advantage of the PRS to yield a reduced profile, without affecting the HB FPC antenna. In HB, the FPC antenna works with the first-order FPC mode. Without relying on a traditional dual-band resonance cavity, the proposed antenna facilitates more flexible frequency ratio. A prototype working at 5.5GHz and 9GHz was designed and fabricated. The overall profile of the antenna is 0.36 and 0.59 wavelengths in LB and HB, respectively. The antenna achieves 7.3% and 6.7% overlapping bandwidths between the 10dB impedance bandwidths and 3dB realized gain bandwidths in LB and HB. It offers the simulated peak realized gains of 10.7dBi and 15dBi, respectively.

References

[1] J. Navarro Ortiz, P. Romero Diaz, S. Sendra, P. Ameigeiras, J. J. Ramos-Munoz, and J. M. Lopez-Soler, "A survey on 5G usage scenarios and traffic models," *IEEE Commun. Surveys & Tutorials*, vol. 22, no. 2, pp. 905-929, Feb. 2020.

[2] M. Z. Chowdhury, M. Shahjalal, S. Ahmed, and Y. M. Jang, "6G wireless communication systems: applications, requirements, technologies, challenges, and research directions," *IEEE Open J. Commun. Society*, vol. 1, pp. 957-975, July 2020.

[3] A. Dogra, R. K. Jha, and S. Jain, "A survey on beyond 5G network with the advent of 6G: architecture and emerging technologies," *IEEE Access*, vol. 9, pp. 67512-67547, Oct. 2021.

[4] T. Li and Z. N. Chen, "Metasurface-based shared-aperture 5G S-/K-band antenna using characteristic mode analysis," *IEEE Trans. Antennas Propag.*, vol. 66, no. 12, pp. 6742-6750, Dec. 2018.

[5] G. Zhou, B. Sun, Q. Liang, S. Wu, Y. Yang, and Y. Cai, "Triband dual-polarized shared-aperture antenna for 2G/3G/4G/5G base station applications," *IEEE Trans. Antennas Propag.*, vol. 69, no. 1, pp. 97-108, Jan. 2021.

[6] F. Qin, and *et al*., "A triband low-profile high-gain planar antenna using Fabry-Perot cavity," *IEEE Trans. Antennas Propag.*, vol. 65, no. 5, pp. 2683-2688, May 2017.

[7] P. Mei, X. Q. Lin, G. F. Pedersen, and S. Zhang, "Design of a triple-band shared-aperture antenna with high figures of merit," *IEEE Trans. Antennas Propag.*, vol. 69, no. 12, pp. 8884-8889, Dec. 2021.

[8] G. V. Trentini, "Partially reflecting sheet arrays," *IEEE Trans. Antennas Propag*., vol. 4, no. 4, pp. 666-671, Oct. 1956.

[9] A. Goudarzi, M. M. Honari, and R. Mirzavand, "Resonant cavity antennas for 5G communication systems: a review," *Electronics*, vol. 9, no. 7, pp. 1080, July 2020.

[10] F. Meng and S. K. Sharma, "A dual-band high-gain resonant cavity antenna with a single layer superstrate," *IEEE Trans. Antennas Propag*., vol. 63, no. 5, pp. 2320-2325, May 2015.

[11] Y. Lv, X. Ding, and B. Wang, "Dual-wideband high-gain Fabry-Perot cavity antenna," *IEEE Access*, vol. 8, pp. 4754-4760, Dec. 2020.

[12] J. Chen, Y. Zhao, Y. Ge, and L. Xing, "Dual-band high-gain Fabry-Perot cavity antenna with a shared-aperture FSS layer," *IET Microwaves, Antennas Propag*., vol. 12, no. 13, pp. 2007-2011, Feb. 2018.

[13] C. Chen, Z. G. Liu, H. Wang, and Y. Guo, "Metamaterial-inspired self-polarizing dual-band dual-orthogonal circularly polarized Fabry-Pérot resonator antennas," *IEEE Trans. Antennas Propag*., vol. 67, no. 2, pp. 1329-1334, Feb. 2019.

[14] E. B. Lima, J. R. Costa, and C. A. Fernandes, "Multiple-beam focal-plane dual-band Fabry-Pérot cavity antenna with reduced beam degradation," *IEEE Trans. Antennas Propag*., vol. 67, no. 7, pp. 4348-4356, Jul. 2019.

[15] A. Pirhadi, M. Hakkak, F. Keshmiri, and R. Karimzadeh Baee, "Design of compact dual band high directive electromagnetic bandgap (EBG) resonator antenna using atificial magnetic conductor," *IEEE Trans. Antennas Propag*., vol. 55, no. 6, pp. 1682-1690, Jun. 2007.

[16] J. Qi, Q. Wang, F. Deng, Z. Zeng, and J. Qiu, "Low-profile uni-cavity high-gain FPC antenna covering entire global 2.4 GHz and 5 GHz WIFI-bands using uncorrelated dual-band PRS and phase compensation AMC," *IEEE Trans. Antennas Propag*., early access. July 2022.

[17] H. Moghadas, M. Daneshmand, and P. Mousavi, "A dual-band high-gain resonant cavity antenna with orthogonal polarizations," *IEEE Antennas Wireless Propag. Lett*., vol. 10, pp. 1220-1223, 2011.

[18] B. A. Zeb, Y. Ge, K. P. Esselle, Z. Sun, and M. E. Tobar, "A simple dual-band electromagnetic band gap resonator antenna based on inverted reflection phase gradient," *IEEE Trans. Antennas Propag*., vol. 60, no. 10, pp. 4522-4529, Oct. 2012.

[19] B. A. Zeb, N. Nikolic, and K. P. Esselle, "A high-gain dual-band EBG resonator antenna with circular polarization," *IEEE Antennas Wireless Propag*. Lett., vol. 14, pp. 108-111, Sep. 2015.

[20] F. Qin, and *et. al*., "A simple low-cost shared-aperture dual-band dual-polarized high-gain antenna for synthetic aperture radars," *IEEE Trans. Antennas Propag*., vol. 64, no. 7, pp. 2914-2922, Jul. 2016.

[21] M. L. Abdelghani, H. Attia, and T. A. Denidni, "Dual- and wideband Fabry-Pérot resonator antenna for WLAN applications," *IEEE Antennas Wireless Propag. Lett*., vol. 16, pp. 473-476, Jan. 2017.

[22] Z. Liu, R. Yin, Z. Ying, W. Lu, and K. Tseng, "Dual-band and shared-aperture Fabry-Perot cavity antenna," *IEEE Antennas Wireless Propag. Lett*., vol. 20, no. 9, pp. 1686–1690, Sep. 2021.

[23] P. Mei, S. Zhang, and G. F. Pedersen, "A dual-polarized and high-gain X-/Ka-band shared-aperture antenna with high aperture reuse efficiency," *IEEE Trans. Antennas Propag*, vol. 69, no. 3, pp. 1334-1344, Mar. 2021.

[24] A. H. Abdelrahman, F. Yang, A. Z. Elsherbeni, and P. Nayeri, *Analysis and Design of Transmitarray Antennas*, Morgan & Claypool, 2017.

[25] Ben A. Munk, *Frequency Selective Surfaces: Theory and Design*, John Wiley & Sons, 2000.

[26] D. M. Pozar, *Microwave engineering*, 3rd ed., John Wiley & Sons, 2005.

[27] L. Zhou, X. Chen, Y. Cui, and X. Duan, "Comparative effects of capacitive and inductive superstrates on the RCA's gain," *IET Microw. Antennas Propag*., vol. 12, pp. 1834-1838, May 2018.

[28] R. Li, D. Thompson, M. M. Tentzeris, J. Laskar, and J. Papapolymerou, "Development of a wide-band short backfire antenna excited by an unbalance-fed H-shaped slot," *IEEE Trans. Antennas Propag*., vol. 53, no. 2, pp. 662-671, Feb. 2005.

[29] G. Zhou, B. Sun, Q. Liang, Y. Yang, and J. Lan, "Beam-deflection short backfire antenna using phase-modulated metasurface," *IEEE Trans. Antennas Propag*., vol. 68, no. 1, pp. 546-551, Jan. 2020.

[30] V. K. Kanth, and S. Raghavan, "Complementary frequency selective surface array optimization using equivalent circuit model," in *Proc. IEEE MTT-S Int. Microw. RF Conf. (IMaRC)*, Ahmedabad, India, Dec. 2017, pp. 1-4.

Paper IV

Co-Designed Millimeter-Wave and Sub-6GHz Antenna for 5G Smartphones

This letter proposes a co-designed millimeter-wave (mm-wave) and sub-6GHz antenna system. The antenna system consists of four 28GHz mm-wave arrays with reconfigurable radiation patterns and two sub-6GHz antennas fed with two corner capacitive coupling elements (CCEs). Each corner CCE is formed by the connected ground planes of two mm-wave arrays in the shared-aperture configuration. The two CCEs are separately matched to cover two sub-6GHz bands. Each mm-wave array consists of an active patch element and two parasitic patch elements loaded with PIN diodes, realizing 90-degree beam scanning range with two states of the PIN diodes. The measured results of the fabricated prototype show good agreement with the simulated ones. The prototyped mm-wave arrays cover the band 27.5-28.35GHz, and each achieves 90º beam scanning at 28GHz, with measured peak realized gain of 7.9 dBi. The CCE ports cover the two sub-6GHz bands of 0.79-0.96GHz and 1.7-5GHz, with measured isolation of above 17dB and 20dB, respectively. The mm-wave band isolation is above 26dB.

Qiuyan Liang, Hanieh Aliakbari and Buon Kiong Lau,
"Co-Designed Millimeter-Wave and Sub-6GHz Antenna for 5G Smartphones,"
IEEE Antennas Wireless Propag. Lett., vol. 21, no. 10, pp. 1995-1999, Oct. 2022.

1 Introduction

With the widespread adoption of smartphones and the increasing use of bandwidth-hungry apps, there is demand for ever higher data rates in wireless communications. Millimeter wave (mm-wave) technology can facilitate higher data rates, due to more bandwidth being available at higher frequencies [1], [2]. But to compensate for high path loss in mm-wave bands to ensure sufficient coverage area, mm-wave antennas need to form steerable beams with high gains.

One popular approach for mm-wave beam-steering is to use conventional phased array antennas [3]-[7]. However, phase shifters can incur considerable insertion loss and phased array elements can occupy a relatively large volume in a smartphone [8]. To facilitate a compact radiator and avoid the use of phase shifters, a 28GHz array with parasitic elements is proposed [8]. The beam-steering is realized by shorting the parasitic elements via four transmission lines of different lengths. However, no real switch is used in the measurement and the transmission lines occupy considerable printed circuit board (PCB) space.

To fit multiple antennas working in widely separated bands into the limited space of a smartphone, co-design of the mm-wave antenna and sub-6GHz antenna has been studied [9]-[17]. In [9] and [10], the mm-wave arrays with feeding networks and the sub-6GHz antennas (chip antennas/monopoles) are designed in separate spaces. In [11] and [12], the slot structure acting as a mm-wave connected array is cleverly reused as a defected ground structure to improves the isolation between the sub-6GHz antennas. However, the array and sub-6GHz antennas still occupy separate spaces.

To improve aperture utilization, a frequency-reconfigurable slot antenna with a varactor diode working in a 4G band is reused as a mm-wave antenna based on the connected slot array concept [13]. However, its 4G band is limited to 2.05-2.7GHz. As another share-aperture approach, the mm-wave array module is embedded into the metal bezel present in some smartphones, with the bezel serving as the sub-6GHz antenna [14]-[16]. This method helps to reduce the blockage of the mm-wave antenna radiation due to the metallic frame. Similarly, the addition of grating strips facilitates the reuse of the PCB space occupied by a low-band planar inverted-F antenna (PIFA) for implementing a mm-wave antenna array [17]. However, the mm-wave antennas in [14]-[17] are still phased arrays with lossy feeding networks, and some sub-6GHz antennas (e.g., PIFA) occupy relatively large spaces.

In this work, a co-designed smartphone antenna system is proposed to accommodate four mm-wave arrays and two sub-6GHz antennas in a compact space. The mm-wave array employs parasitic elements loaded with PIN diodes to achieve beam-steering, in the same manner as Yagi-Uda antenna [18]. Instead of using self-resonant elements, the sub-6GHz antennas are excited by non-resonant capacitive coupling elements (CCEs) [19], which are becoming popular to realize low cellular

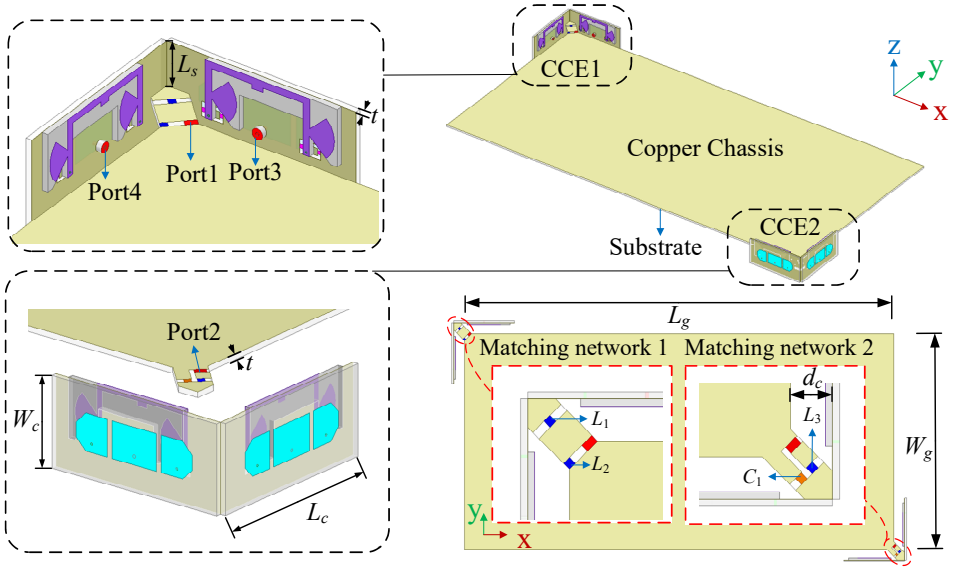

Figure 1: Overall structure of proposed co-designed antenna (L_s = 4mm, L_c = 17mm, W_c = 8mm, t = 0.508mm, L_g = 120mm, W_g = 60mm, d_c = 3mm).

band antennas due to their compactness and simple structure (see [20] and references therein). The metal ground planes of the mm-wave arrays are shared by the corner CCEs that excite the sub-6GHz bands. This shared-aperture configuration with compact mm-wave arrays on the corner CCEs facilitates sleek integration into 5G smartphones. The fabricated prototype confirms that each mm-wave array can realize 90° scanning range with good impedance matching in the desired frequency band of 27.5-28.35GHz. Therefore, the four mm-wave arrays on the two CCEs enable full 360° coverage. The two sub-6GHz antennas are well matched in the operating bands of 0.79-0.96GHz and 1.7-5GHz, respectively.

2 Co-Designed Antenna System

Figure 1 provides the three-dimensional (3D) view and top view of the proposed co-designed antenna system. It consists of four mm-wave arrays mounted on two corner CCEs and a 120mm × 60mm chassis excited by the two CCEs to cover two sub-6GHz bands. The proposed antenna system is further described below.

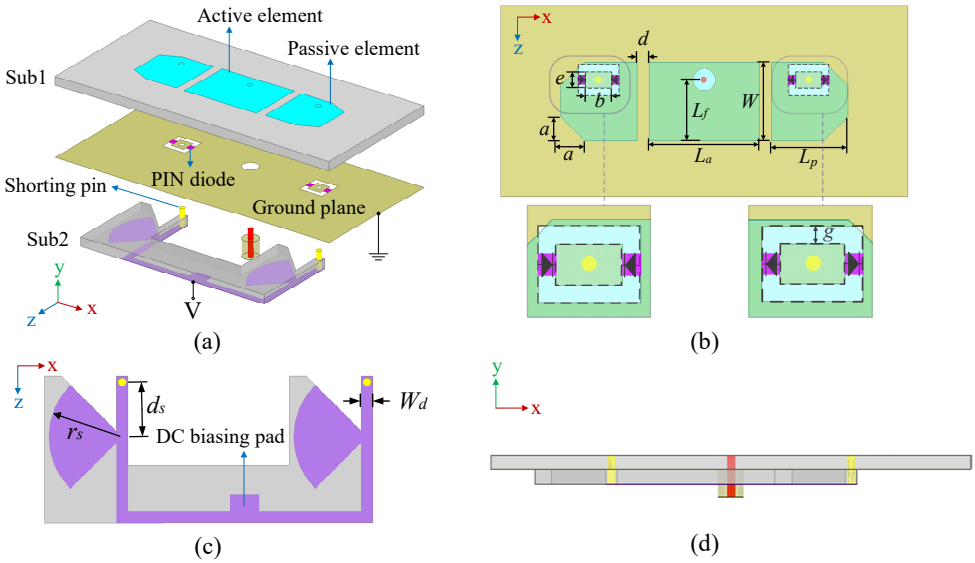

Figure 2: Geometry of mm-wave array fed by Port3. (a) Three-dimensional exploded view. (b) Top view (a = 1mm, b = 1.1mm, d = 0.5mm, e = 0.7mm, L_a = 4.6mm, L_f = 2.6mm, L_p = 3.2mm, W = 3.3mm, g = 0.3mm). (c) DC biasing lines (r_s = 1.8mm, d_s = 2.2mm, W_d = 0.6mm). (d) Side view.

2.1 Mm-Wave Antenna Array

As shown in Fig. 2, the antenna array uses two layers of substrate (Rogers 5880, with thickness of 0.508mm, relative permittivity of 2.2 and loss tangent of 0.0009) for the radiating layer (Sub1) and the direct current (DC) control layer (Sub2). The array is composed of an active element fed with a 50Ω coaxial cable and two passive elements symmetrically located on two sides of the active element. Each passive element is loaded with two PIN diodes bonded over a square slot etched on the ground. The DC biasing lines are printed on the bottom layer of Sub2. Two shorting pins connect the DC biasing lines, the passive elements and the metal sheets within the etched slots. The two sets of PIN diodes for the two passive elements are installed with opposite bias directions and their DC biasing lines with isolation fan stubs are connected in parallel to share a DC feeding pad. The opposite bias ensures that, when a DC voltage is applied, the PIN diodes of one passive element will always be in the opposite state to those of the other passive element (i.e., ON and OFF states for passive elements 1 and 2, respectively, or vice-versa). The PIN diodes, produced by MACOM (Model no. MA4GP907), allow for operation up to millimeter frequencies [21]. Its equivalent circuits for the ON and OFF states in mm-wave bands, as shown in Fig. 3, were used in the simulation model, where the insertion loss of the PIN diode in the ON and OFF state is modelled with a 5.2Ω and a 10kΩ resistor, respectively.

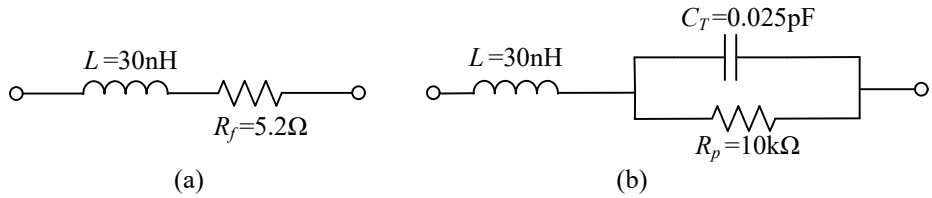

Figure 3: Equivalent circuits of PIN diode in (a) ON state and (b) OFF state.

The parasitic element is connected to/disconnected from the ground plane when the beneath PIN diodes are turned ON/OFF, which decreases/increases its effective electrical size, such that it acts as a director/reflector [22]. The beam of this array is steered to the director and away from the reflector based on the principle of Yagi-Uda antenna. By applying positive or negative DC voltage between the DC biasing pad and the ground, two symmetrical beams can be achieved.

The effects of the structural parameters were investigated using ANSYS HFSS 2021. The simulation results show that the beam deflection angle and sidelobe level (SLL) are mainly dependent on the size of the parasitic elements (controlled by *a*) and the distance between the parasitic elements and the active one (*d*) (see Fig. 2(b)). For example, decreasing *a* or increasing *d* will lead to increased beam deflection angle and SLL, as well as narrower main beam. The appropriate *a* and *d* values were then optimized to obtain ±45° beam deflection (i.e., mirror symmetric beams for the two possible states of the diodes) and low SLL. The impedance bandwidth of the antenna becomes wider when *d* decreases, which is because of that a second (higher) resonance is introduced by the parasitic element in the ON state. Considering the radiation pattern performance and the fabrication tolerance requirements, the distance d = 0.5mm was finally chosen.

2.2 Sub-6GHz Antennas

Since the CCE should be placed in the region of maximum electric field maximum strength of the mode to be excited (i.e., the fundamental dipole mode) [23], two CCEs are placed at two diagonally opposite corners of the chassis. In addition, these corner locations enable the four mm-wave antennas on the two CCEs to cover the entire field of view and mitigate blockage from the user's hand(s). CCE1 and CCE2 excite the chassis through matching networks (see Figs. 1 and 4) designed in Betamatch [24] to realize two sub-6GHz antennas, i.e., Port1 and Port2 cover the low band (LB) of 0.79-0.96GHz and the high band (HB) of 1.71-5GHz, respectively. A larger CCE size facilitates broader bandwidth of Port1, thus the CCE parameters are chosen considering the trade-off between the bandwidth and size [25]. The

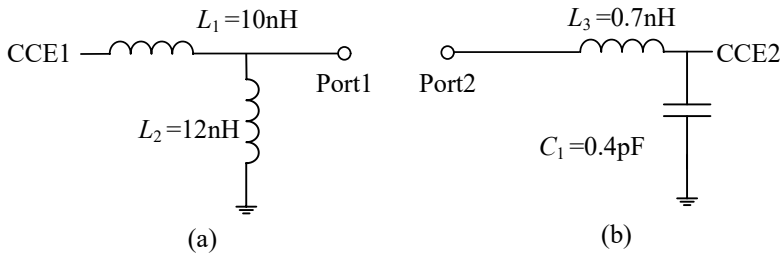

Figure 4: Schematics of matching networks for (a) CCE1 and (b) CCE2.

Figure 5: Proposed antenna system with metal frame.

bandwidth of Port1 and the isolation between Port1 and Port2 in the LB mainly depend on the inductance L_1. With decreasing L_1, the LB bandwidth increases whereas the Port1-Port2 isolation decreases. To achieve a good trade-off between bandwidth and isolation, the matching elements in matching network 1 were chosen to be L_1 = 10nH and L_2 = 12nH. The bandwidth of Port2 in the HB mainly depends on the capacitance value C_1. The Port1-Port2 isolation in HB is not significantly affected by the matching elements. The optimized matching elements in matching network 2 are C_1 = 0.4pF and L_3 = 0.7nH. It is noted that the loading effect of the mm-wave connectors has been included in the design of matching networks, to facilitate experimental validation. In practice, these connectors are not needed and the matching network can be updated by changing the matching circuit parameter values (e.g., L_1 = 18nH and L_2 = 10nH for Port1). Moreover, more matching elements can give a larger Port2 bandwidth (e.g., 1.37-6.71GHz using five elements) [24].

In practical applications, smartphones are equipped with a touch screen and some come with metal bezels (side frames). It is found that adding a metal plate (of the same size as the chassis) 4mm above the chassis (and grounded through a shorting pin at the chassis center) to model the screen does not affect the fundamental mode of the chassis [26], and the impedance matching in the sub-6GHz bands can be restored by updating the matching networks. To study the effect of metal bezels, four separate vertical metal strips of 8mm width were located along (but not

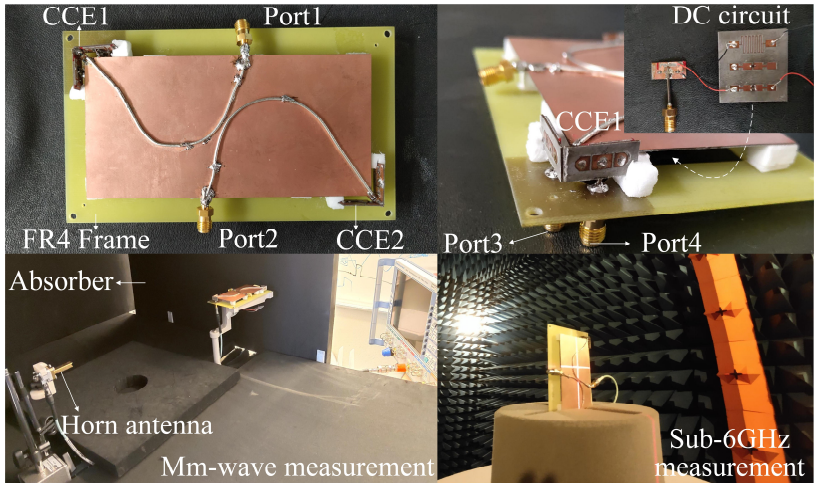

Figure 6: Prototype of proposed antenna system and measurement setups.

connected to) the four sides of the chassis, as depicted in Fig. 5. When the distance d_1 between the strips and the CCE1 is larger than 5mm (0.015 wavelength in free space at 0.875GHz), Port1 retains over 90% of the original bandwidth (i.e., the case with no strip). The distance d_2 for the CCE2 to retain at least 90% of the original bandwidth is 2mm (0.023 wavelength in free space at 3.5GHz).

3 Simulated and Measured Results

A prototype of the smartphone antenna system was fabricated (see Fig. 6). The mm-wave CAB.058 coaxial cables are used to feed the mm-wave arrays on CCE1 in the measurement, which are intended to verify the beam scanning range of the mm-wave arrays on each CCE. In real implementation, the feeding of the mm-wave antenna should be realized with more advanced integrated technology to minimize any possible interference. The DC voltage is applied through a substrate with the DC circuits, which is attached on the back side of the chassis. An FR4 frame is designed to support the antennas in the measurement.

3.1 S-Parameters

Fig. 7 shows the S-parameter results of the two sub-6GHz antennas. The measured 6dB impedance bandwidth (VSWR of 3:1) of Port1 is 0.38GHz (0.75-1.13GHz),

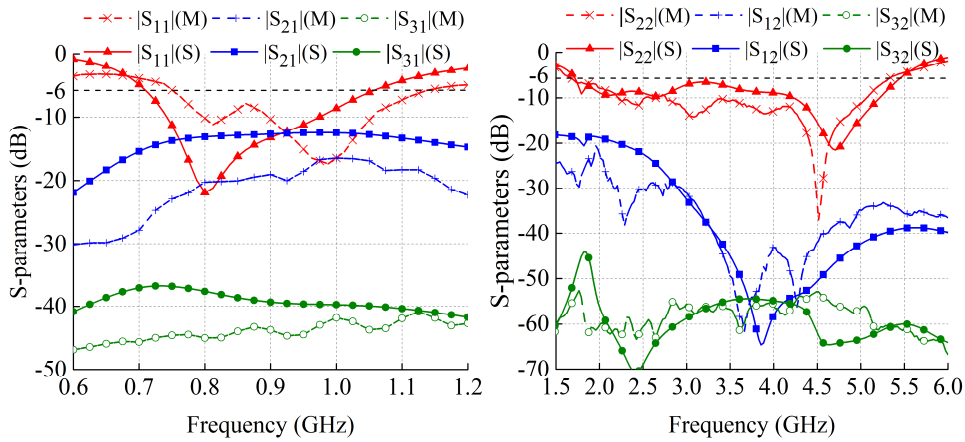

Figure 7: Simulated (S) and measured (M) S-parameters of sub-6GHz antennas.

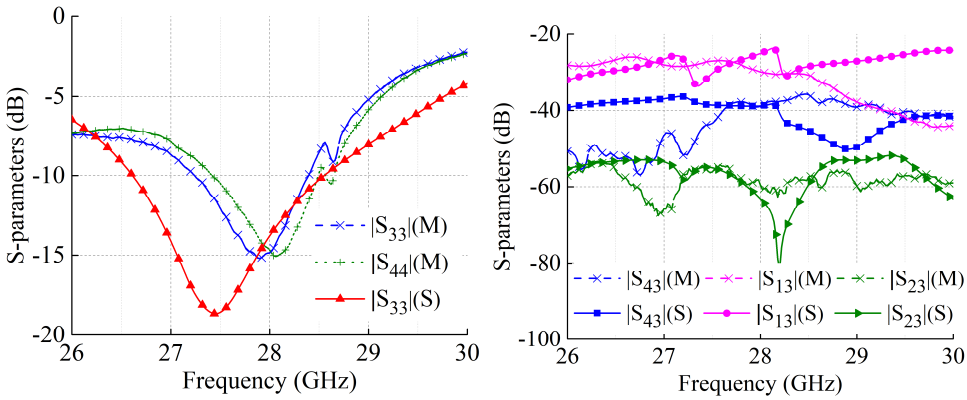

Figure 8: Simulated (S) and measured (M) S-parameters of mm-wave array.

covering the LTE800/850/900 bands. In the operating band (i.e., LB), the measured isolation of the sub-6GHz ports $|S_{21}|$ is larger than 17dB and that between Port1 and mm-wave port Port3 $|S_{31}|$ is larger than 43dB. The measured 6dB impedance bandwidth of Port2 is 3.6GHz (1.70-5.30GHz), covering the LTE1700-2600 and 5G NR n77-79 bands. In this upper band (i.e., HB), the measured isolations with other ports are over 20dB.

The S-parameter results of the mm-wave array are shown in Fig. 8. Port3 and Port4 have the same simulation results for reflection coefficient due to symmetry. The simulated 10dB bandwidth of the mm-wave antenna is around 2GHz (26.56-28.54GHz). It is noted that, if needed, the mm-wave antenna bandwidth can be significantly enhanced (e.g., to 3GHz) by using a stacked patch as the active element.

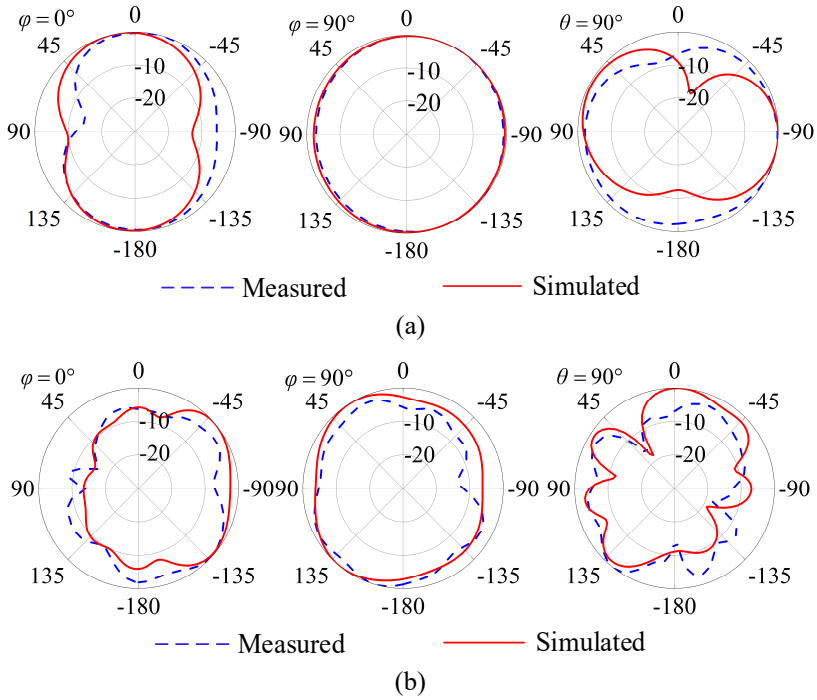

Figure 9: Simulated and measured normalized radiation patterns at sub-6GHz band in (a) LB (0.875 GHz) and (b) HB (3.5GHz).

The measured resonances are slightly higher than those in simulation and the measured bandwidths are narrower than the simulated ones, due to the tolerance in the soldering of the mm-wave cables. Such discrepancy is common in mm-wave bands due to the relatively small wavelengths [13]-[17]. The measured 10dB bandwidths of Port3 and Port4 are 1.15GHz (27.25-28.4GHz) a 1.1GHz (27.4-28.5GHz), respectively, covering the 5G NR n261 band. In the operating mm-wave band, the measured isolations with other ports are over 26dB.

3.2 Radiation Patterns

The radiation pattern results of the fabricated prototype in the sub-6GHz bands were obtained from a SATIMO multi-probe spherical near-field system [27]. Figure 9 shows the normalized simulated and measured 2-D pattern cuts at $\theta = 90°$ (azimuth cut), $\varphi = 0°$ (elevation cut), and $\varphi = 90°$ (elevation cut) for Port1 and Port2 at 0.875 GHz in LB and 3.5 GHz in HB, respectively. The fundamental mode of the chassis is excited by the CCEs in the two sub-6GHz antennas.

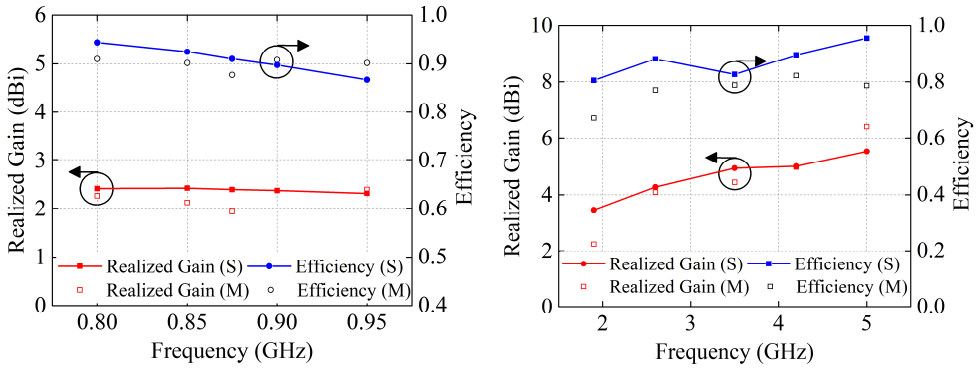

Figure 10: Simulated (S) and measured (M) realized gain and efficiency in sub-6GHz in (a) LB and (b) HB.

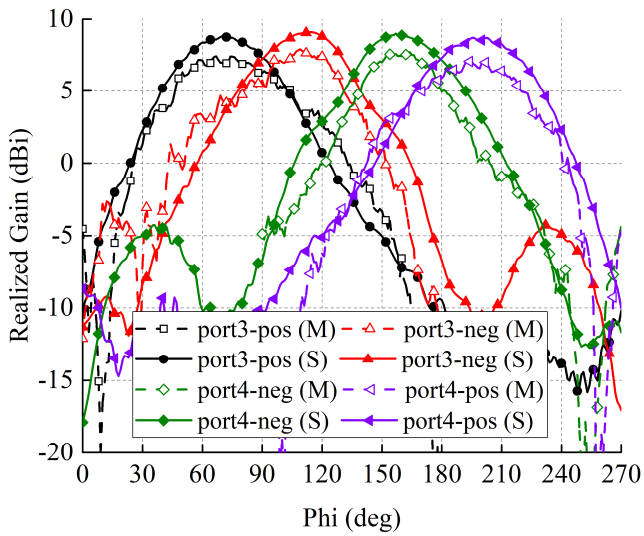

Figure 11: Simulated (S) and measured (M) radiation patterns of mm-wave arrays with positive (pos) and negative (neg) voltage at 28 GHz.

The discrepancies between the simulated and measured patterns are primarily due to the presence of a feed cable in the near field of the structure. The simulated and measured realized gain and efficiency in the sub-6GHz bands are shown in Fig. 10. The measured efficiencies are higher than the simulated ones at some frequency points due to the discrepancies between the measured and simulated S-parameters.

Table 1: Comparison between the proposed and previous 4G/5G designs.

	Frequency range (GHz)	Total antenna volume (mm^3)	Phased array (mm-wave)	Diodes
[13]	2.05-2.7 and 23-29	35×12.28×0.381	yes	yes
[14]	0.7-0.96, 1.71-2.69 and 25-30	75×10×7	yes	no
[16]	0.76-0.98, 1.24-2.87, and 22-28.4	21.7×7.75×0.64	Active and dummy elements	no
[17]	0.74-0.96, 1.7-2.2, and 22-31	70×9×0.764	yes	no
This work	0.75-1.13, 1.7-5.3 and 27.5-28.35	34×8×1.016×2	no	yes

Figure 11 shows the radiation patterns of two mm-wave arrays on CCE1 at 28GHz, which were measured with an in-house pattern measurement system utilizing the Rohde and Schwarz vector network analyzer ZVA67. Applying the positive/negative voltages on the DC biasing pads of the two mm-wave arrays, four deflected beams were realized. The two mm-wave arrays on CCE1 can achieve 180° coverage range with half power beamwidth. The peak measured realized gains are 7.4dBi or 7.9dBi (Port3 with positive or negative voltage) and 7.1dBi or 7.7dBi (Port4 positive or negative voltage). The peak measured realized gains are less than the simulated ones by 1.4dBi (Port3 positive), 1.2dBi (Port3 negative), 1.6dBi (Port4 positive) and 1.3dBi (Port4 negative), respectively. The realized gain difference is primarily due to the loss in the mm-wave cables and slight pattern shape discrepancy, the latter of which was caused by inaccuracies in the PIN diode's equivalent circuits and the tolerance of the measurement system.

3.3 Comparison with Other Sub-6GHz/Mm-Wave Antennas

A comparison of recent co-designed antennas for sub-6GHz and mm-wave bands is presented in Table 1. The sub-6GHz antennas in [14] and [17] employ self-resonance structures, which occupy larger volumes. Phased arrays, which require feeding networks, are used for the mm-wave antennas in [13], [14] and [17]. The proposed antenna system can cover wider sub-6GHz bands despite the use of two compact CCEs. With the parasitic elements, the proposed mm-wave array achieves beam scanning without the need for complex feeding networks. Moreover, the shared-aperture configuration of the corner CCEs and mm-wave arrays enables a compact antenna volume.

4 Conclusion

A co-designed mm-wave and sub-6GHz antenna system for 5G smartphone application is proposed in this letter. Each mm-wave array antenna uses two parasitic elements loaded with PIN diodes to realize beam scanning. The four mm-wave arrays share the aperture of the CCEs, with the latter providing coverage of two sub-6GHz bands, which facilitates a compact antenna structure. The measured results show that the sub-6GHz antennas cover the bands of 0.79-0.96GHz and 1.71-5GHz. The mm-wave array provides 90° scanning range with measured realized gain of up to 7.9dBi at 28GHz. Possible future work includes adding ports in the sub-6GHz bands for MIMO operation by means of creating and exciting more resonant modes [20] as well as using more parasitic elements and reconfigurable states for higher gain in mm-wave bands.

5 Acknowledgement

The authors would like to thank A. Johansson of Lund University and D. Pugachev of Sigma Connectivity for their help in prototype fabrication and pattern measurement.

References

[1] T. S. Rappaport, *et al*., "Millimeter wave mobile communications for 5G cellular: It will work!" *IEEE Access*, vol. 1, pp. 335-349, 2013.

[2] W. Hong, K. H. Baek, and S. Ko, "Millimeter-wave 5G antennas for smartphones: Overview and experimental demonstration," *IEEE Trans. Antennas Propag*., vol. 65, no. 12, pp. 6250-6261, Dec. 2017.

[3] N. Ojaroudiparchin, M. Shen, S. Zhang, and G. F. Pedersen, "A switchable 3-D-coverage-phased array antenna package for 5G mobile terminals," *IEEE Antennas Wireless Propag. Lett.*, vol. 15, pp. 1747-1750, Feb. 2016.

[4] S. Zhang, X. Chen, I. Syrytsin, and G. F. Pedersen, "A planar switchable 3-D-coverage phased array antenna and its user effects for 28-GHz mobile terminal applications," *IEEE Trans. Antennas Propag*., vol. 65, no. 12, pp. 6413-6421, Dec. 2017.

[5] I. Syrytsin, S. Zhang, G. F. Pedersen, and A. S. Morris, "Compact quad-mode planar phased array with wideband for 5G mobile terminals," *IEEE Trans. Antennas Propag*., vol. 66, no. 9, pp. 4648-4657, Sep. 2018.

[6] W. Hong, K. Baek, Youngju Lee, and Yoon Geon Kim, "Design and analysis of a low-profile 28 GHz beam steering antenna solution for future 5G cellular applications," in *Proc. IEEE MTT-S Int. Microw. Symp. (IMS)*, Tampa, USA, Jun. 1-6, 2014, pp. 1-4.

[7] N. Ojaroudiparchin, M. Shen, and G. F. Pedersen, "A 28 GHz FR-4 compatible phased array antenna for 5G mobile phone applications," in *Proc. Int. Symp. Antennas Propag. (ISAP)*, Hobart, Australia, Nov. 9-12, 2015, pp. 1-4.

[8] S. Zhang, I. Syrytsin, and G. F. Pedersen, "Compact beam-steerable antenna array with two passive parasitic elements for 5G mobile terminals at 28 GHz," *IEEE Trans. Antennas Propag.*, vol. 66, no. 10, pp. 5193-5203, Oct. 2018.

[9] C. Lee, M. K. Khattak, and S. Kahng, "Wideband 5G beamforming printed array clutched by LTE-A 4 × 4-multiple-input-multiple-output antennas with high isolation," *IET Microw. Antennas Propag.*, vol. 12, no. 8, pp. 1407-1413, Mar. 2018.

[10] R. Hussain, A. T. Alreshaid, S. K. Podilchak, and M. S. Sharawi, "Compact 4G MIMO antenna integrated with a 5G array for current and future mobile handsets," *IET Microw. Antennas Propag.*, vol. 11, no. 2, pp. 271-279, Jan. 2017.

[11] M. Ikram, R. Hussain, and M. S. Sharawi, "4G/5G antenna system with dual function planar connected array," *IET Microw. Antennas Propag.*, vol. 11, no. 12, pp. 1760-1764, Sep. 2017.

[12] M. S. Sharawi, M. Ikram, and A. Shamim, "A two concentric slot loop based connected array MIMO antenna system for 4G/5G terminals," *IEEE Trans. Antennas Propag.*, vol. 65, no. 12, pp. 6679-6686, Dec. 2017.

[13] M. Ikram, E. A. Abbas, N. Nguyen-Trong, K. H. Sayidmarie, and A. Abbosh, "Integrated frequency-reconfigurable slot antenna and connected slot antenna array for 4G and 5G mobile handsets," *IEEE Trans. Antennas Propag.*, vol. 67, no. 12, pp. 7225-7233, Dec. 2019.

[14] J. Kurvinen, H. Kähkönen, A. Lehtovuori, J. Ala-Laurinaho, and V. Viikari, "Co-designed mm-Wave and LTE handset antennas," *IEEE Trans. Antennas Propag.*, vol. 67, no. 3, pp. 1545-1553, Mar. 2019.

[15] R. M. Moreno, J. A. Laurinaho, A. Khripkov, J. Ilvonen, and V. Viikari, "Dual-polarized mm-wave endfire antenna for mobile devices," *IEEE Trans. Antennas Propag.*, vol. 68, no. 8, pp. 5924-5934, Aug. 2020.

[16] R. C. Rocio, S. Zhang, K. Zhao, and G. F. Pedersen, "Mm-wave beam-steerable endfire array embedded in a slotted metal-frame LTE antenna," *IEEE Trans. Antennas Propag.*, vol. 68, no. 5, pp. 3685-3694, May 2020.

[17] M. M. Samadi Taheri, A. Abdipour, S. Zhang, and G. F. Pedersen, "Integrated millimeter-wave wideband end-fire 5G beam steerable array and low-frequency 4G LTE antenna in mobile terminals," *IEEE Trans. Veh. Technol.*, vol. 68, no. 4, pp. 4042-4046, Apr. 2019.

[18] J. Huang and A. C. Densmore, "Microstrip Yagi array antenna for mobile satellite vehicle application," *IEEE Trans. Antennas Propag*., vol. 39, no. 7, pp. 1024-1030, July 1991.

[19] J. Villanen, J. Ollikainen, O. Kivekas, and P. Vainikainen, "Coupling element based mobile terminal antenna structures," *IEEE Trans. Antennas Propag*., vol. 54, no. 7, pp. 2142-2153, July 2006.

[20] H. Aliakbari and B. K. Lau, "Low-profile two-port MIMO terminal antenna for low LTE bands with wideband multimodal excitation," *IEEE Open J. Antennas Propag*., vol. 1, pp. 368-378, 2020.

[21] MACOM. (2016). *Products: MA4GP907*. [Online]. Available: http://cdn.macom.com/datasheets/MA4GP907.pdf

[22] W. Deng, X. Yang, C. Shen, J. Zhao, and B. Wang, "A dual-polarized pattern reconfigurable Yagi patch antenna for microbase stations," *IEEE Trans. Antennas Propag*., vol. 65, no. 10, pp. 5095-5102, Oct. 2017.

[23] R. Valkonen, M. Kaltiokallio, and C. Icheln, "Capacitive coupling element antennas for multi-standard mobile handsets," *IEEE Trans. on Antennas Propag*., vol. 61, no. 5, pp. 2783-2791, May 2013.

[24] Betamatch. (2019). *MNW Scan Pte Ltd, Version 3.7.6*. Accessed: Nov. 11, 2021. [Online]. Available: http://www.mnw-scan.com

[25] H. Aliakbari and B. K. Lau, "Impact of capacitive coupling element design on antenna bandwidth," in *Proc. 12th Europ. Conf. Antennas Propag. (EuCAP)*, London, UK, Apr. 9-13, 2018, pp. 1-4.

[26] H. Aliakbari, L. Y. Nie, and B. K. Lau, "Large screen enabled tri-port MIMO handset antenna for low LTE bands," *IEEE Open Journal of Antennas and Propag.*, vol. 2, pp. 911-920, Aug. 2021.

[27] Satimo Stargate. (2019). *Measurement System*. Accessed: Aug. 26, 2021. [Online]. Available: http://www.satimo.com